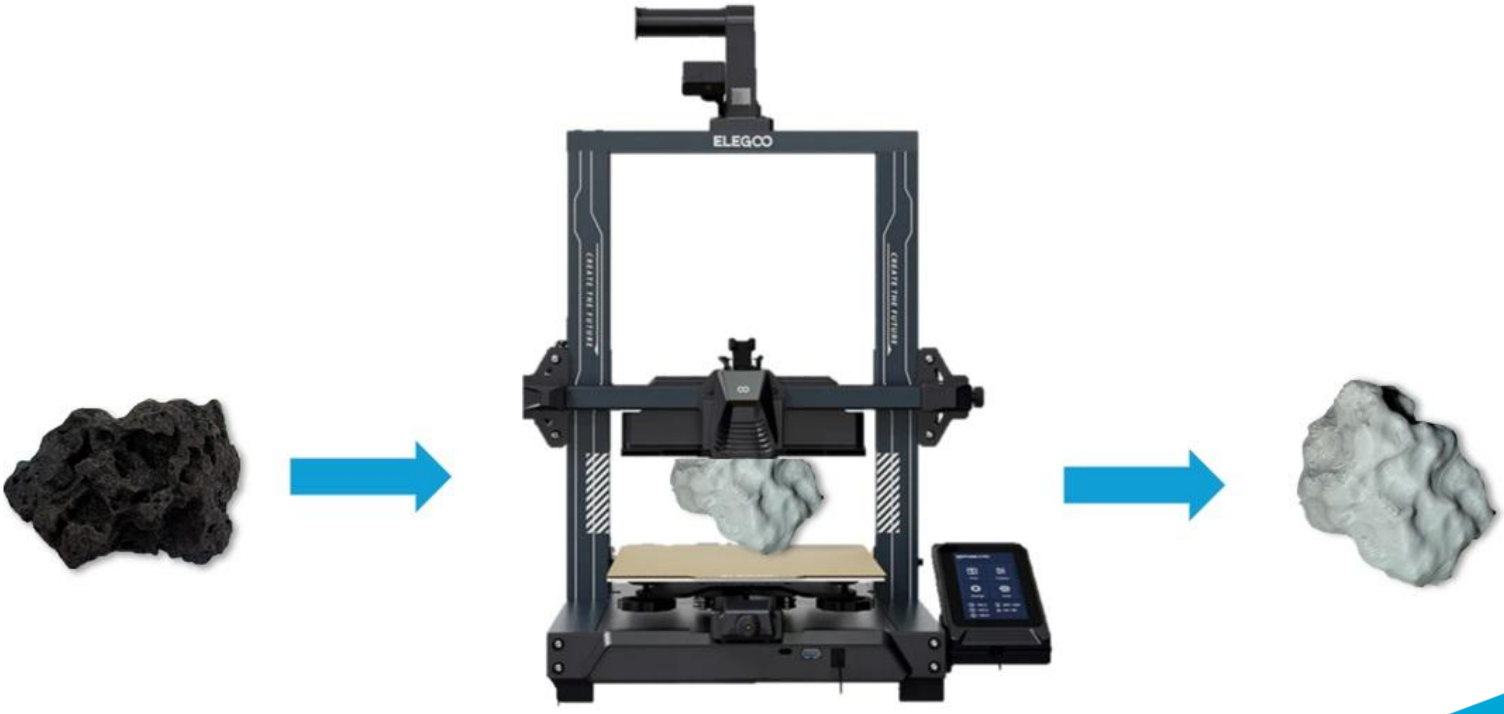

From Sinter to Print

Linking Particle Shape and Flowability

Author: E. Asad Pour
Date: 26 January 2026

From Sinter to Print

Linking Particle Shape and Flowability

By

E. Asad Pour

In partial fulfilment of the requirements for the degree of:

Master of Science
in Mechanical Engineering

at the Department Maritime and Transport Technology of Faculty Mechanical Engineering of
Delft University of Technology
to be defended publicly on Monday January 26, 2026 at 13:00

Student number: 5040418
MSc track: Multi-Machine Engineering
Report number: 2025.MME.9150
Project duration: January 27, 2025 – January 26, 2026
Supervised by: Prof.dr.ir. D. Schott
Dr. A. Hadi,
Dr. H. Shi,
Date: January 26, 2026

Preface

This thesis was written as part of the master's program in Mechanical Engineering at TU Delft from January 2025 to January 2026. Its main focus is on how particle shape simplification affects the flowability of 3D-printed sinter particles.

The motivation for this research arises from the increasing need to improve the accuracy and efficiency of Discrete Element Method (DEM) simulations used to analyze granular materials. Although sinter is crucial in steel production, its highly irregular particle shape presents ongoing challenges for both computational and experimental modeling. By exploring the use of physical replicas with controlled geometric simplifications, this study aims to bridge the gap between computational limits and real-world material behaviour.

I would like to thank Prof. dr. ir. D. Schott, Ahmed-Hadi, and Hao-Shi for their advice and feedback. Their inputs helped me develop a more critical and structured approach to experimental work and analysis. Additionally, I am grateful to Ton Veer and the IWS Faculty Workshop team for their technical support in 3D printing the particle replicas, and to Raïsa Roeplal and Wouter Schuitemaker for providing the MATLAB codes for quantitative analysis (Appendix B and Appendix H).

Finally, I want to thank my family and friends for their support throughout this thesis.

Erol Asad Pour
Rotterdam, January 2026

Contents

Abstract

Granular materials, including iron ore sinter, play a crucial role in steelmaking, where bulk behaviour affects process efficiency. The highly irregular and angular morphology of sinter particles governs their bulk behaviour. In order to understand the bulk behaviour of granular materials, like sinter, simulations are performed. Discrete Element Method is a widely used technique for simulating bulk behaviour. However, in this method the particle shapes are often simplified as spheres to minimize computational cost. This raises the question of the extent to which particle shape detail is needed to maintain realistic bulk behaviour. In this study, the scope of bulk behaviour is limited to flowability. To overcome the computational load of DEM simulations, geometric complexity was transferred from the virtual to the physical domain by fabricating 3D-printed sinter particle replicas at various levels of simplification.

For shape simplification, three common DEM shape modelling approaches, multi-sphere, polyhedral, and super-ellipsoid, were first evaluated, after which polyhedral models were chosen due to their superior ability to capture angular features. Then, the shape fidelity across various simplification levels (400,000-40 faces) was quantified using shape descriptors (sphericity, convexity, and roundness). Based on these quantifications in shape deviations, four shape models were selected: the original shape (400,000 faces, previously 3D-printed by Wouter Schuitemaker), the threshold resolution (400 faces), an intermediate model between the threshold and most simplified resolution (100 faces), and the most simplified model (40 faces). The latter three models were 3D-printed in bulk (1000 particles per model). Then these models were used in flowability experiments, where angle of repose (AoR), coefficient of static friction (μ_s), and Hausner ratio (HR) were measured.
From the results, it follows that geometric simplification increases the sphericity, convexity, and roundness, with a critical threshold near 400 faces, below which these shape descriptor values increase nonlinearly. The AoR, μ_s, and HR exhibit only modest variations across simplification levels, and confidence intervals overlap substantially, showing that stepwise differences are generally not statistically significant. Statistically detectable cumulative reductions occur only at very low face counts (~100 faces or fewer) and are primarily associated with increases in sphericity and convexity; roundness has a weaker influence.

Importantly, the AoR remains within the ‘cohesive’ flowability classification up to 100 faces, indicating negligible practical change in bulk flow behaviour. Only for the most simplified 40-face particles does AoR approach the upper bound of the ‘fair-flowing’ classification. The HR follows a similar trend, remaining within ‘poor flowability’ before reaching the upper bound of the ‘passable’ category for the 40-face particles, implying a marginal increase in flowability.

Overall, flowability appears relatively insensitive to particle shape simplification within the tested range. Statistically detectable changes might occur only at very low resolutions (~100 or fewer faces), with the 40-face particles showing a slight shift in flowability classification. Whether other aspects of bulk behaviour beyond flowability are sensitive to shape simplification remains to be determined.

Samenvatting

Granulaire materialen, zoals ijzerertssinter, zijn essentieel in de staalproductie. Hun bulkgedrag heeft directe invloed op de efficiëntie van het proces. Dat gedrag wordt sterk bepaald door de onregelmatige en hoekige vorm van de sinterdeeltjes. Om dit beter te begrijpen, worden simulaties gebruikt. Een veelgebruikte methode is DEM, waarbij deeltjes vaak tot bolvormen worden vereenvoudigd om de rekenkosten en rekentijd te beperken, wat de vraag oproept hoeveel vormdetail nodig is om het bulkgedrag realistisch te simuleren. In deze onderzoek ligt de focus op de stromingseigenschap (flowability) van het materiaal. Om de hoge rekentijd van DEM-simulaties te vermijden, is de geometrische complexiteit verplaatst van het virtuele naar het fysieke domein door 3D-geprinte replica's van sinterdeeltjes te maken met verschillende vereenvoudigingsniveaus.

Voor de vereenvoudiging van de deeltjesvorm zijn eerst drie veelgebruikte DEM-benaderingen onderzocht: multi-sphere-, polyhedrale- en superellipsoïde modellen. Omdat polyhedrale modellen hoekige kenmerken het beste weergeven, is voor deze methode gekozen. Vervolgens, is de vormnauwkeurigheid bij resoluties van 400.000 tot 40 vlakken is gekwantificeerd met behulp van vormparameters(sfericiteit, convexiteit en rondheid). Op basis hiervan zijn vier representatieve resoluties gekozen: de oorspronkelijke (400.000 vlakken, eerder 3D-geprint door Wouter Schuitemaker), de grensresolutie (400), een tussenmodel (100) en het sterkst vereenvoudigde model (40 vlakken). De laatste drie modellen zijn in bulk geprint (1000 deeltjes per model). Deze deeltjes zijn vervolgens gebruikt in experimenten, waarbij de angle of repose (AoR), de statische wrijvingscoëfficiënt (μ_s) en de Hausner-ratio (HR) zijn bepaald.
Uit de resultaten blijkt dat geometrische vereenvoudiging leidt tot een toename van sfericiteit, convexiteit en rondheid. Daarbij is een duidelijke grens zichtbaar rond 400 vlakken; onder deze waarde nemen de vormkenmerken niet-lineair toe. De gemeten waarden voor AoR, μ_s en HR variëren slechts beperkt tussen de vereenvoudigingsniveaus. Pas bij zeer sterke vereenvoudiging (ongeveer 100 vlakken of minder) treden cumulatieve, statistisch aantoonbare afnames op. Deze zijn vooral gerelateerd aan toenemende sfericiteit en convexiteit, terwijl rondheid een minder grote invloed heeft. Belangrijk is dat de AoR tot en met 100 vlakken binnen de classificatie *cohesive* blijft, wat erop wijst dat het praktische bulkstromingsgedrag nauwelijks verandert. Pas bij de sterkst vereenvoudigde deeltjes met 40 vlakken nadert de AoR de bovengrens van de classificatie *fair-flowing*. De Hausner-ratio (HR) vertoont een vergelijkbaar patroon: deze blijft binnen de categorie *poor flowability* en bereikt pas bij de 40-vlakkige deeltjes de bovengrens van *passable*. Dit wijst op slechts een geringe verbetering van de stromingseigenschappen.

Samenvattend blijkt de stromingseigenschap (flowability) binnen het onderzochte bereik relatief ongevoelig voor vereenvoudiging van de deeltjesvorm. Statistisch merkbare veranderingen doen zich waarschijnlijk alleen voor bij zeer lage resoluties (ongeveer 100 vlakken of minder), waarbij de 40-vlakkige deeltjes een lichte verschuiving in de flowability-classificatie laten zien. Of andere aspecten van bulkgedrag, buiten flowability, gevoelig zijn voor vormvereenvoudiging, moet nog worden onderzocht.

AI statement

For this MSc. graduation thesis work for the course [ME-MME MSc Thesis + ME54035], I have used Generative AI to:

- Create (part of) the code in [MATLAB] for solving the problem
- Obtain inspiration for the overall structure of the report
- Improve the grammar, style, layout, and/or spelling of the text

In all cases I have reviewed and corrected the work and remain fully responsible for the content of the report.

1 Introduction

1.1 Background

Granular material consists of a collection of particles, usually varying in size from 1 µm to 10 m, that demonstrate behaviour affected by forces or displacements, causing interactions that lead to a loss of energy. These materials are generally found in nature and extensively manipulated in different industrial uses [1,2], and can transition from a solid-like state to a fluid-like state depending on the applied force or displacement.
When these particles are subjected to external forces (e.g., compression from weight or shear stress of a flowing motion), they must rearrange their position. These rearrangements are inherently inelastic. Because particle interactions dissipate energy through frictional contacts and inelastic collisions, granular flow cannot sustain itself without continuous energy input. Contrary to an ideal fluid, which can flow indefinitely in the absence of losses, a granular material loses momentum once the external driving force is removed. The particles then settle into a mechanically stable configuration, making the system revert to a solid-like state (e.g., a sand pile coming to rest) [3,4].

As for the steel industry, sinter (granular material composed of fused iron ore) is a key element of the blast furnace burden (a layered mix of raw materials) [5]. Sinter particles are irregular in shape, with a heterogeneous structure that entails both smooth, dense areas and fractured, porous regions. Their irregular surface textures, varying from dull to shiny, exhibit the partial melting and solidification that takes place during the sintering process, as shown in Figure 1.

Figure 1 Macro-type features A-E on sinter particles [6]

This blast furnace burden is charged from the top of the blast furnace (Figure 2). As the burden descends, it interacts with the hot gases rising from the furnace's bottom. These gases mainly drive endothermic reactions, where the iron ore gradually melts into liquid iron.

This resulting liquid iron then flows out of the blast furnace and gets used for further processing in steel production. The efficiency of these reactions in the blast furnace depends on how well the solid-gas interactions occur. Since these interactions depend on the internal structure of the burden, the geometry of the particles, and the shaping of how they interact during charging and descent, they directly determine the bulk behaviour of the bed [7].

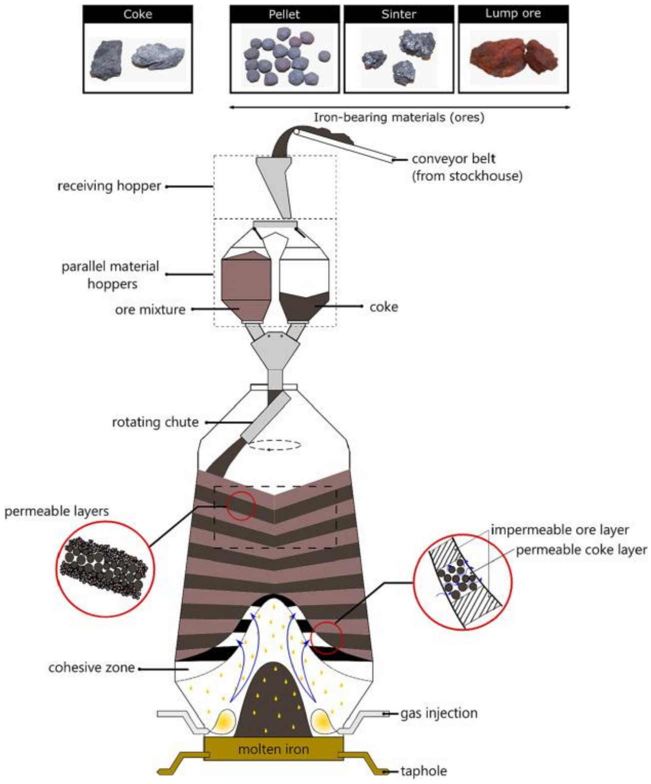

Figure 2: Schematic view of the blast furnace [7]

Accordingly, this study focuses only on sinter particles, as their irregular shapes significantly influence bed structure and permeability. Therefore, it is important to understand the shape effects of sinter particles on bulk behaviour in order to improve the blast furnace efficiency and ultimately the overall performance and energy efficiency of steelmaking [8,9].

To understand the bulk behaviour, numerical simulations can be applied to examine particle-scale interactions. The Discrete Element Method (DEM), introduced by Cundall and Strack in 1979, is a generally used numerical simulation method to simulate granular materials. DEM provides information about the location, velocity, stress, and energy of each particle in a granular system. [10–12]. The particles are often modelled as spheres due to their low computational load [13].

However, particle shape significantly affects the bulk behaviour of granular materials [14]. Therefore, it is one of the most demanding aspects of DEM simulations [15–18].
Accurately capturing the effect of particle shape is essential for reliable DEM simulations.

1.2 Problem Definition

In spite of the recognized important role of particle shape on bulk behaviour, DEM simulations usually depend on spherical approximations. Simulating particle shapes with accurate shapes comes with a great computational load. In calibration studies, simulations using spherical particles finished in only 40-70 minutes, while it took 7-8 hours using polyhedral particles. Extending this across 81 simulations, a full set required 2-4 days with spheres but 23-32 days when polyhedra were involved, thus showcasing the steep computational cost [19]. Thus, it is more efficient to use alternative methods that cover particle shape effects without the impractical computational cost.
The method in this study uses 3D printing to replicate sinter particles at varying levels of geometric simplification for application in experiments. By transferring particle shape complexity into the physical domain, this approach takes away the computational burden of software-based simulations while still ensuring the acquisition of critical insights into bulk behaviour [20]. Here, a representative (non-simplified) sinter particle shape (Figure 3), 3D printed by [21], is used as a reference for comparison with the simplified particles, and the scope of the bulk-behaviour analysis is restricted to flowability.

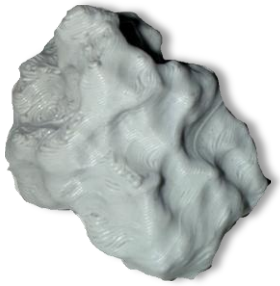

Figure 3: 3D-printed sinter particle (original shape)

By systematically comparing 3D-printed particles with varying levels of geometric simplification, this study investigates the effect of shape simplification on flowability and reproduces experimental reference data to support the development of more accurate but simultaneously computationally efficient DEM simulations.

1.3 Research Questions

“How does the shape simplification of 3D-printed sinter particle affect their flowability?’’

In order to answer this research question , the following sub-questions have to be answered first:

1. Which shape modelling method and shape descriptors most accurately capture and quantify the geometry of irregularly shaped particles?
2. How does the level of geometric simplification impact the shape descriptors and volume relative to the original particle?
3. How to 3D print simplified shaped particles in bulk with matched volume and weight to the original particle?
4. How does the level of simplification influence measurable bulk properties such as angle of repose, coefficient of static friction, and Hausner ratio?

2 Modelling and Quantifying Irregularly Shaped Particles

This chapter provides an answer to the following sub-research question: *Which shape modelling method and shape descriptors most accurately capture and quantify the geometry of irregularly shaped particles?* Here, three shape modelling approaches multi-sphere, polyhedral, and super-ellipsoid are critically compared alongside a literature-based review of shape descriptors. These models are chosen due to their prominent application in DEM for representing irregular particle shapes [22–24].

The discussion is carried out in three stages. First, the theoretical foundations, strengths, and limitations of each modelling approach are studied, focusing on their capability to represent irregularly shaped particles: the multi-sphere model via overlapping spheres, the polyhedral model across vertices and planes, and the super-ellipsoid model through parametric equations. Furthermore, particle shape descriptors are evaluated, including 3D measures like sphericity and convexity and 2D measures such as roundness, to review their effectiveness in quantifying morphological differences between original and simplified geometries. Finally, given these analyses, the chapter recognizes the most suitable shape modelling approach and critical set of descriptors for systematic application further on.

By establishing a clear framework for choosing shape models and descriptors, this chapter guarantees that subsequent comparisons of geometric fidelity through different simplification levels are both rigorous and reproducible, ultimately enabling accurate quantification of shape deviations in 3D-printed particles.

2.1 Particle Shape Models

Three established particle shape models are applied to capture the complex morphology of irregularly shaped particles: the multi-sphere model, polyhedral models, and the super-ellipsoid model.

2.1.1 Multi-Sphere Model

The multi-sphere model is one of the most effective and generally adopted techniques in Discrete Element Method (DEM) modelling for exhibiting irregular particle shapes. Here, one should assemble a set number of smaller spheres, or “sub-spheres,” whose size, number, and position can be varied to approach the desired geometry [16,25]. This flexibility enables it to represent particles with highly irregular geometries. By augmenting the number of sub-spheres, the approximation gets more refined, and the particle shape more closely resembles real particles [22,26,27].

Two modes are applied to arrange the sub-spheres upon approximating a multi-sphere particle:

1) **Control Geometry (CG) Principle:**
   Here, sub-spheres are organized to match the outer form of the particle as closely as they can. For example, CG-3 refers to a control geometry consisting of three sub-spheres, with accuracy rising as more and smaller sub-spheres are applied (Figure 4).

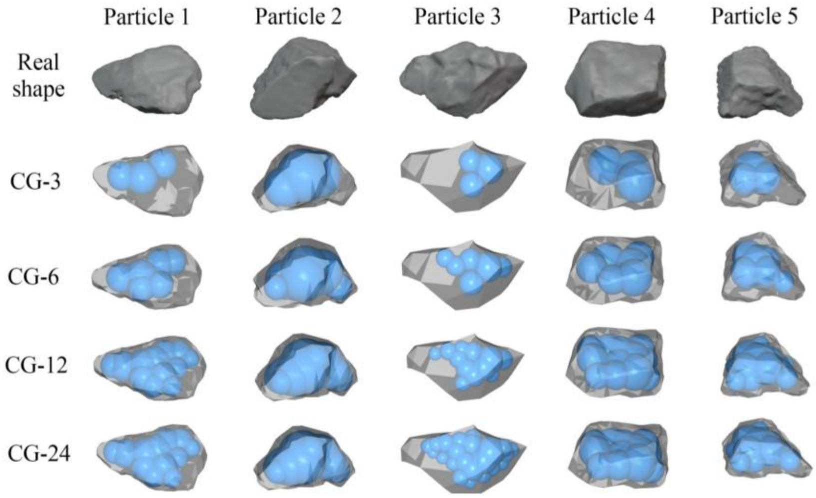

Figure 4: Particles represented by the multi-sphere model (control geometry) *[22]*

2) **Control Volume (CV) Principle:**
   Here, the multi-sphere particle and the corresponding real particle share the same volume. In Figure 5, CV depicts the ‘control volume’. The number following the variable name CV represents the number of particles. Here, the same principle applies, as the larger the number of particles, the smaller they are, and therefore the more accurate the particle geometry representation becomes.

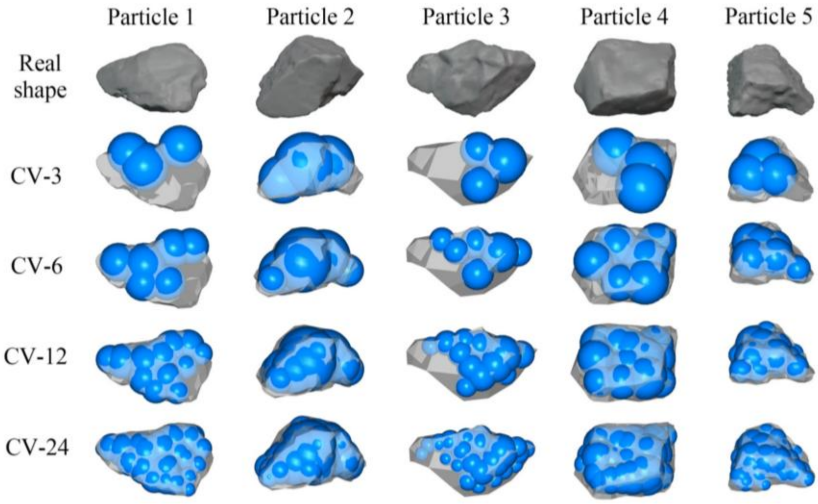

Figure 5: Particles represented by the multi-sphere model (control volume) [22]

The Control Geometry Principle (CG) concentrates on matching the shape of the real particle by organizing sub-spheres to tightly follow its outer form. The Control Volume Principle (CV) guarantees that the total volume of the sub-spheres equals the volume of the real particle, even if the shape isn't perfectly matched. CG is better for shape accuracy, while CV rather suits volume and mass accuracy.

The multi-sphere method in Discrete Element Method (DEM) modelling is especially useful for exhibiting non-spherical particle shapes. Its main strength is that contact detection and force calculation can depend on simple algorithms primarily developed for spheres or discs. By taking the validated sphere–sphere contact detection algorithm, the method guarantees accuracy and computational efficiency without the necessity for developing new algorithms for complex particle geometries. This makes the method both efficient and robust [25,28–30].

Nevertheless, when looking at physical experiments entailing 3D-printed particles, with the particle shapes being realized physically rather than approximated numerically, the advantages connected to simplified contact detection and force computation become irrelevant, because these interactions are governed by the real physical geometry rather than a computational model. Therefore, the benefits of efficient computation can only be seen in simulation environments, not in physical experimental contexts.

In spite of its wide application, the multi-sphere method has restrictions when approximating particle surfaces. Given that it depends on overlapping spheres, the outer surface of the particle is inherently “bumpy” rather than smooth. This limits its ability to capture sharp edges or flat faces, even in case many sub-spheres are used. Consequently, while it can approximate spherical or slightly irregular shapes reasonably well, the model becomes less accurate for highly angular particles [25,31].

Overall, the multi-sphere model is efficient and adaptable for DEM simulations but stays restricted by its bumpy surface representation and decreased accuracy for angular particles. These shortcomings reduce its suitability for physical studies with 3D-printed particles, where geometric fidelity is more critical than computational simplicity.

2.1.2 Polyhedral Model

Polyhedral particles consist of a number of vertices, edges, and planes. Hence, it is rather appropriate to apply the polyhedral model to show the discontinuity of the particle surface. In general, the geometric primitive utilized to build the polyhedral particles is the triangular plane, as illustrated in Figure 6. As with the multi-sphere model, the shape approximation precision of the polyhedral model can be augmented by applying more triangular planes at the expense of extending computational load [22,32].

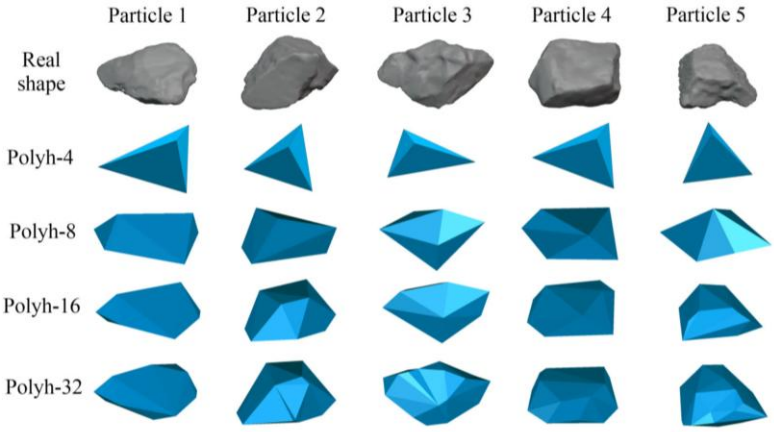

Figure 6: Particles represented by the polyhedral model [22]

A main advantage of the polyhedral model entails its superior ability to represent angular and faceted particle shapes in comparison to sphere-based models. Unlike the multi-sphere model, which naturally produces rounded and bumpy surfaces, the polyhedral model is able to closely approximate sharp edges, flat faces, and complex geometries. This polyhedron modelling method is applied in many fields (like geotechnical and geotechnical engineering) to reasonably simplify complex shapes (e.g., ores and rocks) [22,23].

One restriction of the polyhedral model entails the requirement of greater computational effort compared to multi-sphere and super-ellipsoid models during Discrete Element Method (DEM) simulations given the complexity of calculating contacts between multiple planes and edges. This augmented computational cost may become significant upon simulating systems with many particles or highly detailed geometries [33–35].

Nonetheless, physical experiments here will be conducted by using 3D-printed particles rather than computational DEM simulations. As such, the increased computational burden related to the polyhedral model is eliminated. This makes sure the advantages of the polyhedral approach are fully used without concern for simulation time.

2.1.3 Super-Ellipsoid Model

The super-ellipsoid method refers to the application of super-ellipsoids, a mathematical shape that generalizes the ellipsoid by applying various exponents in its equation to acquire a range of shapes from spherical to rectangular (Figure 7).

The super-ellipsoid shape formulation can be seen as an extension of spherical or ellipsoidal shapes and can be applied to represent spherical, ellipsoidal, cylindrical, diamond-like, and cubic particles by varying solely five shape parameters (a, b, c, s_1, s_2) [36] .

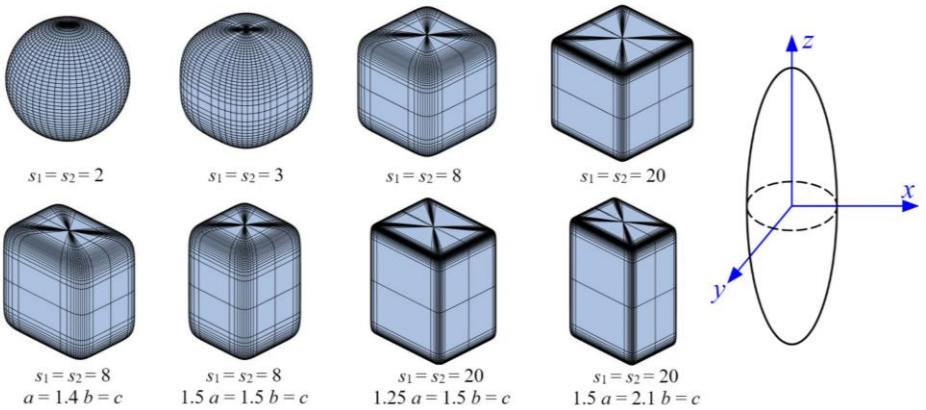

Figure 7: Particles represented by the super-ellipsoid model [22]

Equation 1 describes the shape of a super-ellipsoid:

$$f(x, y, z) = \left(\left|\frac{x}{a}\right|^{s_2} + \left|\frac{y}{b}\right|^{s_2}\right)^{\frac{s_1}{s_2}} + \left|\frac{z}{c}\right|^{s_1} - 1 = 0 \qquad (1)$$

, where:

- a, b and c: constitute the semi-major axis lengths, defining the particle's size along the x, y, and z axes, respectively.
- s_1, s_2: represent shape indices that control the particle's edges' curvature. Low values (≈ 1) produce rounded shaped (sphere-like), whereas larger values (>10) produce sharp-edged, box-like shapes.

The key strength of super ellipsoidal models is their flexibility and mathematical efficiency. With simple parameter adjustments, they can exhibit a wide range of non-spherical particle shapes such as ellipsoids, cylinders, and cubes with sharp edges [37]. The super ellipsoid function can accurately describe these particle shapes (e.g. ellipsoids) instead of relying on an approximation made of multiple spheres or polyhedra. This ensures low computational load in DEM simulations upon analysing particle interactions[38]. This particle shape model fits best for smooth particles from a sphere to an elongated [22,39,40].

Given that there are particles with an ellipsoidal shape, [24], showed that the super ellipsoid model regenerates packing and flow behaviour both more accurately and more efficiently than the multi-sphere model. The latter asks for a large number of spheres to approximate the geometry, which greatly enhances computational time while still introducing approximation errors.

The restriction of the super-ellipsoid method is that it cannot exhibit very irregular, faceted, sharply angular particles, as it generates shapes that are always smooth, symmetric and strictly convex [24,41].

2.1.4 Selection of Particle Shape Model

In this study, the polyhedral model is selected as the most fitting representation for particle shape as it is able to precisely approximate irregularly shaped particle geometries with angular features, flat surfaces, and sharp edges. Table 1 also demonstrates that the multi-sphere model gives rounded, bumpy surfaces given overlapping spheres, deeming it less accurate for faceted or angular particles. The super-ellipsoid model, while efficient for smooth, symmetric, convex shapes, cannot capture the geometric complexity necessary to represent irregular, sharply faceted particles.

Although polyhedral models typically need higher computational effort in DEM simulations given complex contact detection, this limitation is out of place for the present study, since the focus lies on physical experiments using 3D-printed particles, where geometric fidelity is the primary concern (see Table 1 for strengths and limitations of all three models).

Table 1: strengths and limitations of the tree particle shape models (multi-sphere, polyhedral, super-ellipsoid)

Model	Strengths	Limitations
Multi-sphere	Flexible in approximation of irregular shaped particles; widely used in DEM simulations due to its computational efficiency (irrelevant for physical experiments)	Surface is bumpy, poor accuracy for modelling (compared to polyhedral method) faceted, angular shaped particles.
Polyhedral	Accurately represents angular and faceted particle shapes .	Highest computational load in DEM simulations compared to multi-sphere model and super-ellipsoid model, but this is irrelevant for physical simulations
Super-ellipsoid	Accurately represents spheres, ellipsoids, cylinders, diamond-like, and cubes using only 5 parameters; more precise than polyhedron or multi-sphere approximations for these shapes.	Cannot represent very irregular, faceted, sharply angular particles, unlike multi-sphere and polyhedral method.

2.2 Particle Shape Descriptors

A particle’s shape is usually characterized by three hierarchical components (Figure 8). These are the form, which shows the overall geometry of the particle; roundness, which represents the degree of large-scale smoothness or angularity of its edges and corners; and surface texture, which is connected to the fine-scale irregularities present on the particle's surface [42,43].

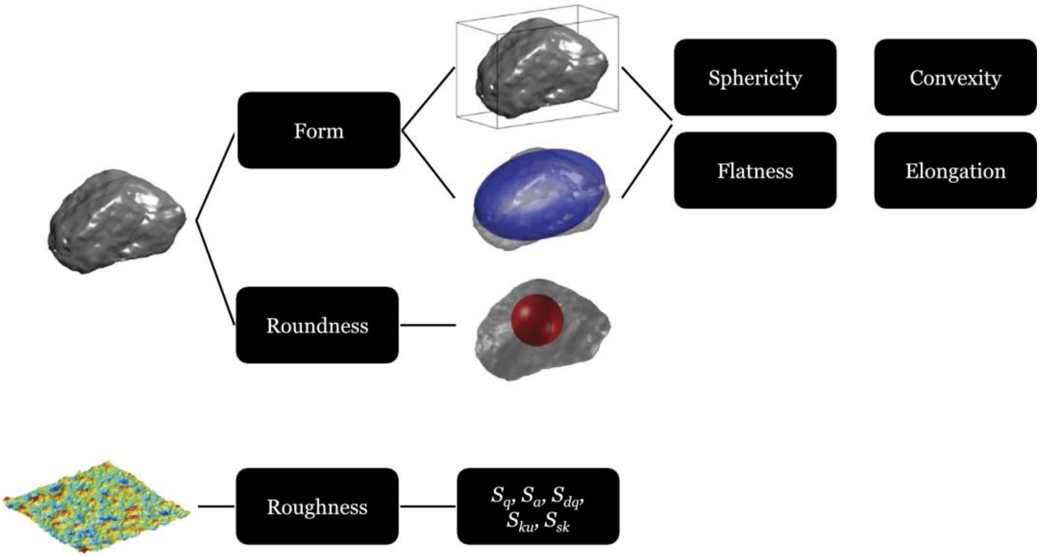

Figure 8: Shape aspects and descriptors [43]

Form is a first-order morphological property, representing the relative proportions of a particle. Roundness is a secondary aspect of particle morphology, connected to the sharpness of corners and edges, and is thus appended on top of the form features. Surface roughness is a third-order aspect of shape, associated with asperities which are appended on top of roundness features. It ought to be remarked that roughness is dependent on scale, so the extent to which this aspect of shape is measured and examined depends on the problem of interest [43,44].

Originally, particle shape characterization was applied in two dimensions, where the shape is determined from the projection of a particle onto a plane [45]. Nevertheless, 2D descriptions are highly dependent on the chosen orientation and projection, which restricts their reliability [46,47]. More recently, 3D approaches have been introduced, depending on techniques such as 3D scanning or the use of two orthogonal images to give a fuller and more accurate representation of particle morphology. Even though 3D imaging involves higher cost and complexity, it gives an orientation-independent representation of particle morphology, making it more suitable for accurate analysis [48].

Here, 3D shape descriptors are applied to quantify morphological variations between original and simplified particles, concentrating on form and roundness. Surface roughness is not taken into account, as the use of identical PLA material and consistent 3D printing parameters guarantees that the texture produced by the FDM process remains qualitatively uniform across all particles.

2.2.1 Form

The first step in quantifying form is to identify the dimensions applied to describe the particle, as these offer the foundation for measuring its form. Wentworth in 1922 [49] was probably one of the pioneering authors to systematically measure particle dimensions. This included determining the lengths of the three principal axes of the particle. The axes are named *a*, *b*, and *c*, with *a* being the longest, *b* being the one of intermediate length, and *c* being the shortest (Figure 9) [48,50].

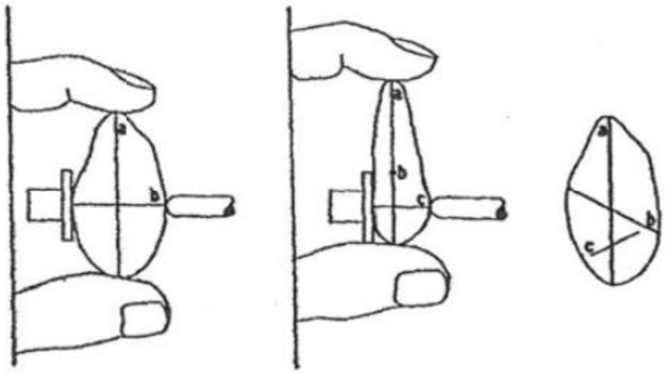

Figure 9: manual measurement of a, b and c [50]

It is commonly agreed that these three axes must be orthogonal to each other, but their point of intersection may differ [51].

Utilizing a, b, and c to identify particle dimensions enables it to represent more complex shapes. However, this method (Figure 9) is generally used for coarse particles because measuring a, b, and c by hand is practical at larger sizes. As particle size decreases, the process becomes more time-consuming. For very fine particles like clay, this method is no longer valid, as the individual particles are too small to observe and measure directly, so a different approach becomes necessary [52]. Therefore, in this study the 3D STL files of each particle are scrutinized by a MATLAB script (Appendix B) to receive geometric shape descriptor values. The code loops through each 3D shape file in shapeFiles. For each shape, it reads the STL file to get vertices (points) and faces (triangles forming the surface). It then centers the shape by subtracting the mean of the vertices. With Principal Component Analysis, PCA ([coeff, ~, latent] = pca(centeredVertices)), it identifies the principal axes of the particle by discovering the directions in which the points vary the most: first longest, then next-longest perpendicular to it, and finally the shortest perpendicular to both. The values in latent represent how much the shape extends along each of these directions (how “long” the shape is in each main direction). From this, the shortest direction is smallest_value (minIndex), the longest is largest_value (maxIndex), and the middle one is intermediate_value (midIndex). This effectively measures the shape’s “natural” length, width, and height. (Figure 10).

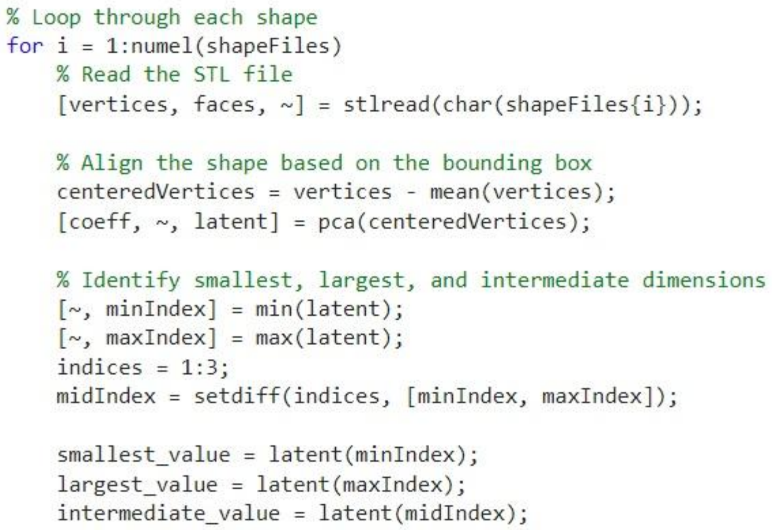

```
% Loop through each shape
for i = 1:numel(shapeFiles)
    % Read the STL file
    [vertices, faces, ~] = stlread(char(shapeFiles{i}));

    % Align the shape based on the bounding box
    centeredVertices = vertices - mean(vertices);
    [coeff, ~, latent] = pca(centeredVertices);

    % Identify smallest, largest, and intermediate dimensions
    [~, minIndex] = min(latent);
    [~, maxIndex] = max(latent);
    indices = 1:3;
    midIndex = setdiff(indices, [minIndex, maxIndex]);

    smallest_value = latent(minIndex);
    largest_value = latent(maxIndex);
    intermediate_value = latent(midIndex);
```

Figure 10: MATLAB code snippet from Appendix B that quantifies a (largest_value),b(intermediate_value) and c (smallest_value)

These axes are then used to determine elongation and flatness, which quantify the particle's aspect ratios. The code further calculates sphericity and convexity, essential descriptors that quantitatively cover the particle's form.

a. Flatness

Flatness is a geometric descriptor that represents the degree to which a particle deviates from a flat, plate-like shape. Throughout literature, flatness has been defined through different formulas. One of those was proposed by Cailleux in 1945, who defined the flatness index based on the relationship between the particle dimensions along the three principal axes (Equation 2), which is mathematically identical to the earlier formulation by Wenthworth [53].

$$flatness = \frac{a+b}{2c} \tag{2}$$

The index varies from the minimum value of 1 for an equant particle and augments progressively the flatter the particle. This index does not have an upper limit, which can complicate comparisons between samples [54].

A more widely adopted formulation of flatness was put forward by Zingg [55], as defined in Equation 3.

$$flatness = \frac{c}{b} \tag{3}$$

This ratio gives values between 0 and 1, where values approaching 0 show highly flat, plate-like particles, and values approaching 1 imply more equant, or equally proportioned, particles. The bounded 0–1 scale of the c/b ratio offers a standardized and straightforward metric for comparing flatness across samples, making it more practical for analytical and computational applications. Consequently, the MATLAB code shown in Appendix B employs the Zingg c/b.

b. Elongation

Elongation measures the ‘stretchiness’ of a particle. Authors have put forward different formulations for elongation [55–58]. The commonly used definition by Zingg (1935) [55] defines elongation as the ratio of the intermediate axis (b) to the shortest axis (a) (Equation 4):

$$elongation = \frac{b}{a} \tag{4}$$

This ratio yields values between 0 and 1, where values approaching 0 show highly elongated, needle-like particles, and values approaching 1 imply more equant, or equally proportioned, particles [49]. Its simplicity and effectiveness make it the best metric for characterizing particle elongation, and it is the formulation used in the MATLAB code in Appendix B.

The combination of flatness and elongation is used in Zingg’s plot for classification of shape. Given the combination of the values of both, the particles can be divided into four categories: oblate, compact, blade-like or prolate (Figure 11).

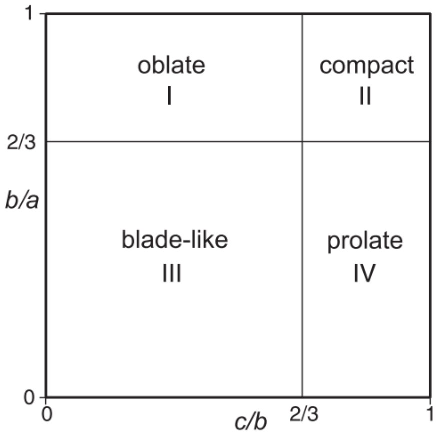

Figure 11: Shape classification system Zingg [59]

c. Convexity

Convexity ratio is a measure of convexity [50]. It simply measures the closeness by which the outline of a particle approaches a convex shape [60]. The value of convexity ranges from 0 to 1. Here, 1 exhibits a perfectly convex shape with no indentations. When the value of convexity approaches 0, it shows a shape that has increasingly concave irregular outlines [61]. In the 2D case it can be computed as the ratio of the particle’s actual area to the area of its convex hull [62]. The application of 2D convexity is generally applied due to the relative ease of acquiring 2D images. However, 2D convexity measurements can be affected by the projection of the particle depending on the orientation choice. 2D projections may not capture all surface concavities, especially those that are not visible in the projection plane, causing an overestimation of convexity [63].

In the 3D convexity analysis the entire shape is examined, leading to a more accurate value of convexity. Therefore, this 3D method will be applied here. The convexity can be described in 3D similarly as the ratio of the particles' volume (V) to the convex hull volume (V_{CH}) (Equation 5) [43,63].

$$Convexity = \frac{V}{V_{CH}} \tag{5}$$

The convex hull is the smallest polyhedron covering the shape, see Figure 12. This convex hull is based on the 3D coordinates of all the surface points of the input shape. Then the convex hull of these points is calculated by a MATLAB function "convhull".

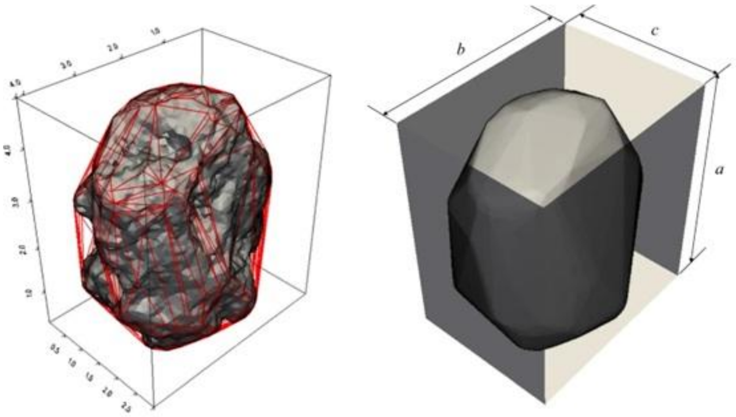

Figure 12: Left: particle shape; Right: convex hull [64]

d. Sphericity

Sphericity quantifies the closeness by which a particle's shape approaches a perfect sphere, with values ranging from 0 to 1, with 1 implying a perfect sphere [65–67].

Several quantitative methods for expressing sphericity are described in literature. One of the methods is brought forward by [50], where a practical approach uses three mutually perpendicular axes (a ≥ b ≥ c) of a particle. By computing the ratios b/a and c/b, sphericity may be determined graphically via a specialized chart, termed the "intercept sphericity" (Figure 13). Though easy, this method neglects complex three-dimensional shape variations, restricting its accuracy in displaying true particle sphericity.

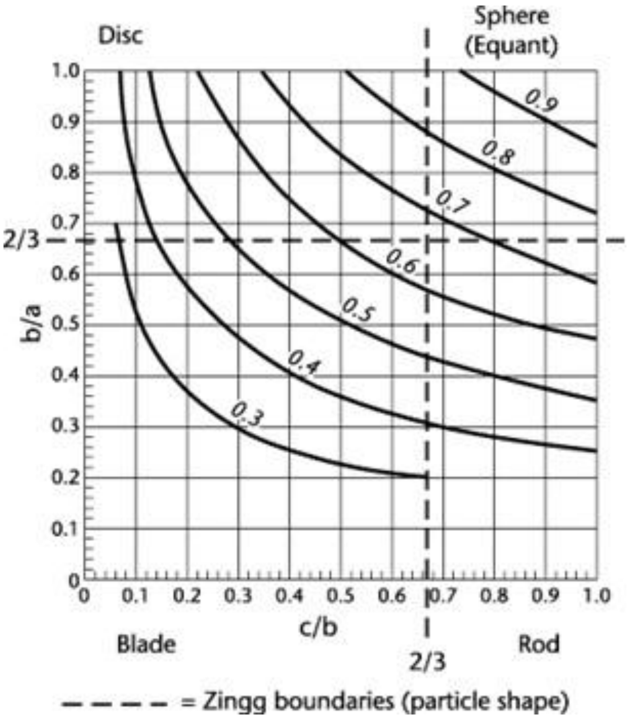

Figure 13: Chart to determine Krumbein intercept sphericity [50,68]

Nevertheless, of the various descriptions of sphericity, none seems to have found such wide recognition and acceptance [69] as Wadell's [70] concept, which can be represented by Equation 6. Therefore, in this study the sphericity as defined by Wadell will be used.

$$\varphi = \frac{\pi^{\frac{1}{3}}\left(6V_p\right)^{\frac{2}{3}}}{S_p} \tag{6}$$

Here, φ stands for sphericity, V_p and S_p describe the particle's volume and surface area respectively.

2.2.2 Roundness

Roundness stands for the natural sharpness or roundness of the particle corners, being the inverse of angularity [49,71,72]. The roundness was first seen by Wadell as the ratio between the average radius of curvature of the corner portion and the maximum inscribed circle radius (Equation 7) [70].

$$R = \frac{\frac{1}{n}\sum_{i=1}^{n} r_i}{r_{ins}} \tag{7}$$

R stands here for roundness, r_i stands for the radius of the corner circle, and r_{ins} is the radius of the maximum inscribed circle. The maximum inscribed circle and the corner circles of a specific particle are shown in Figure 14.

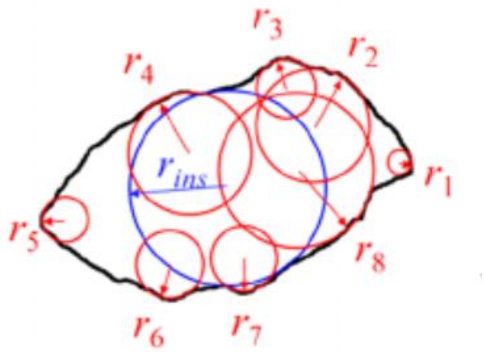

Figure 14: 2D Roundness: r_i (i from 1 to 8) is the radius of the corner circle and r_{ins} is the radius of the maximum inscribed circle [73]

This definition of roundness is restricted to two dimensions [74–76]. The main restriction of this 2D approach entails the fact that a single projection cannot fully capture the complete three-dimensional shape of a particle. Furthermore, the choice of projection angle is subjective, often causing inconsistent roundness assessments [77]. Another limitation is that the original method for determining Wadell's roundness manually entails effort and is subjective. To deal with this issue, the MATLAB (see appendix C) code from the paper [78] is applied.

The MATLAB code determines the maximum inscribed circle as shown in Figure 15. In Figure 15b , for the particle, the nearest boundary pixel is computed for each pixel inside the, which gives a Euclidean distance map. Here, the maximum inscribed radius R_i is identified as the largest distance value in this map, occurring at location C_i.

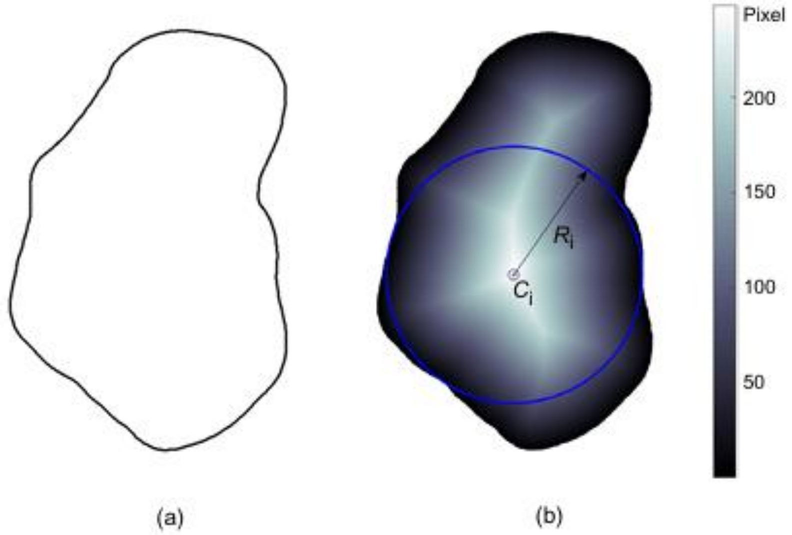

Figure 15: a) particle outline, b) Euclidean distance map [78]

Figure 16 shows the procedure for determining the corner circles. During this procedure all the corner points 1 to 36 are used to compute a best-fit circle (Figure

16(a)). R represents here the radius, C denotes the centre of the circle, and T is the minimum distance from C to the particle boundary. If T is smaller than R, it means the circle is not tangent to the boundary, indicating that it is not a valid corner circle. Here, endpoint 36 is liquidated, and point 35 becomes the new last point. The points from 1 to 35 are now applied to fit a new circle. The recalculated T and R values are compared. If T is still smaller than R, point 35 is deleted and 34 becomes the new last point. The process carries on until a circle is found satisfying T=R or if point 3 becomes the last point.
Figure 16(b) and (c) display how the last point in the fitting process turns when trying to fit a circle to a particle’s edge. The process commences by trying to fit a circle from point 20 back to point 3. If no good circle is found, the loop ends. Then, the process restarts from point 2 and tries again. This continues until a suitable circle is found. For example, in Figure 16(f), a good fit (circle C1) was found using points 2 to 5.

Next, the process moves on: point 6 becomes the new start, and point 36 the new end, as demonstrated in Figure 16(g). Another fitting, C2, is found using points 8 to 10 (Figure 16 (h)). The algorithm continues at this pace until all corners are uncovered.

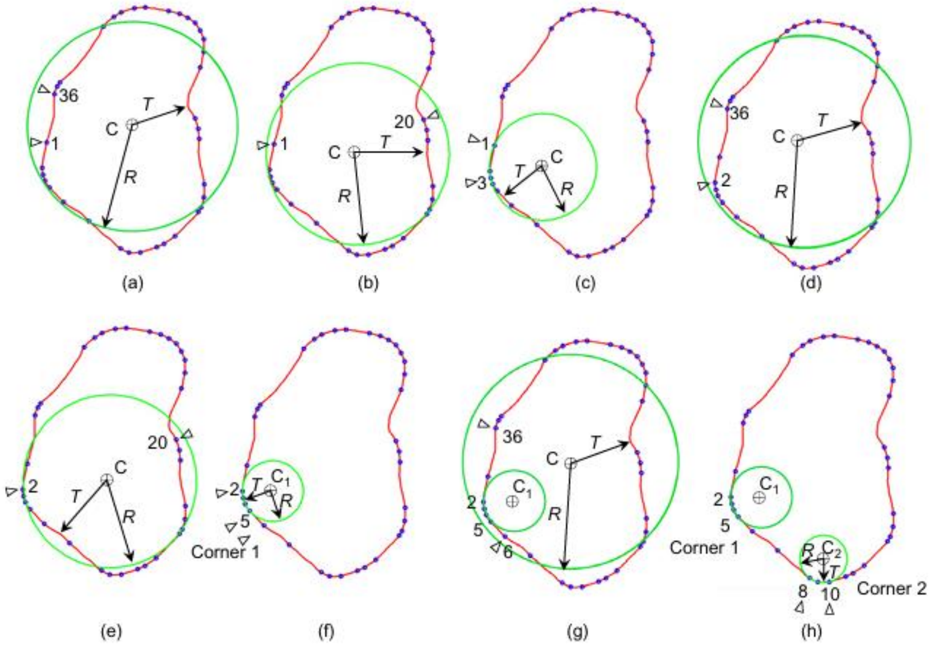

Figure 16: circle-to-corner fitting process [78]

After completing the process, seven corners were discovered on the particle (Figure 17), each with a fitted circle (displayed in green). The maximum inscribed circle of the particle is displayed in red.

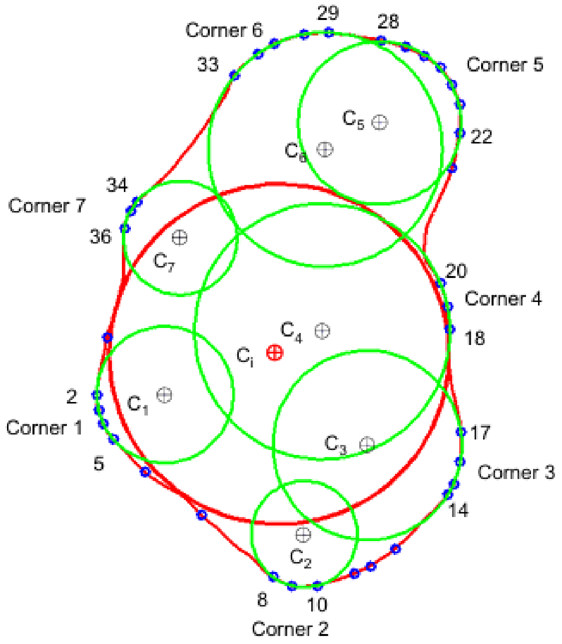

Figure 17: Result of circle-to-corner fitting [78]

Figure 18 shows the result of a circle-to-corner fitting of a particle analysed in this study, with radii expressed in pixels.

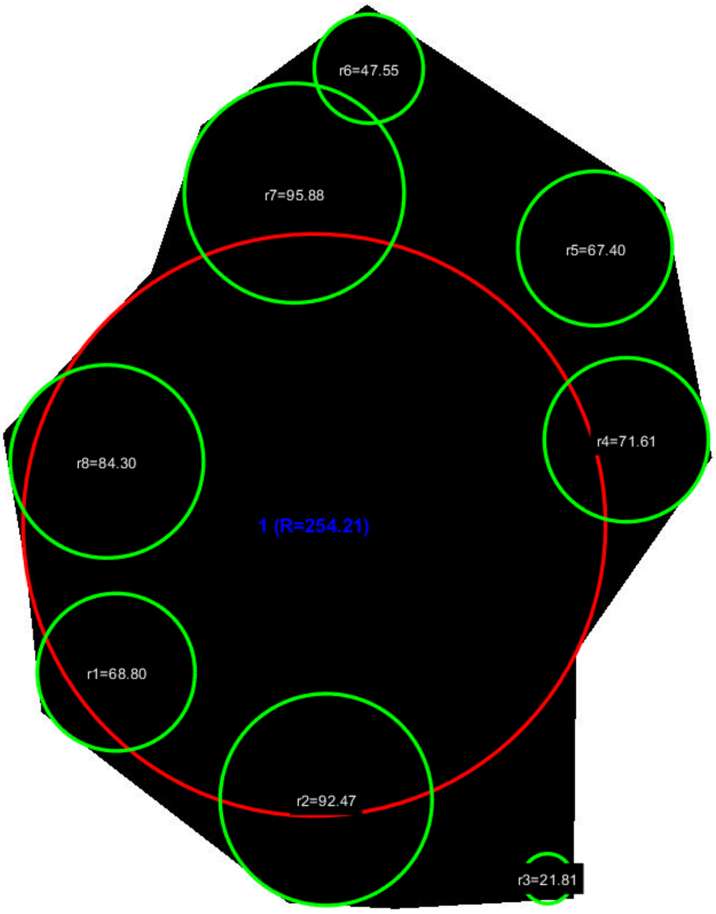

Figure 18: Result of circle-to-corner fitting (60 faces, top view)

This algorithm is restricted to a single 2D plane. Literature experiments prove that early approaches to image-based 3D shape analysis, which are meant to reconstruct particle geometry by combining multiple 2D images from different viewpoints, usually apply three orthogonal projection images (front, side, and top) [79–81].These studies showed that a limited number of 2D views can still give meaningful insights into a particle's three-dimensional shape features.

Following this established approach, the present study estimates the 3D roundness of particles by calculating roundness values from each of the three orthogonal projections, interpreted as the particle's silhouettes viewed along its principal axes: front (YZ plane), side (XZ plane), and top (XY plane). These views can be obtained through Solidworks. The average of these three values is then applied to approximate the overall 3D roundness of the particles at each simplification level.

2.2.3 Selection of Shape Descriptors

Sphericity and convexity were selected as the primary three-dimensional metrics because they provide orientation-invariant characterization of particle shape and surface compactness. Sphericity, defined by Wadell, reflects how closely a particle's shape approaches a perfect sphere by comparing its surface area to that of a sphere with the same volume. Convexity quantifies the ratio of particle volume to the volume of its convex hull, showing the degree of surface concavities or indentations. Sphericity inherently integrates the geometric effects of the three orthogonal axial ratios (b/a and c/b), as described by Krumbein's method (Figure 13), offering a comprehensive measure of particle form. While a single sphericity value can match multiple combinations of b/a and c/b, this additional detail is not needed for quantifying the effect of irregular particle shape on bulk behaviour. This approach offers a reference for DEM simulations, where ideal spheres are commonly applied, and helps improve the accuracy of such simulations. Consequently, separate metrics for elongation and flatness are redundant and are not used to characterize overall particle form.

3D roundness is applied here as a proxy for particle angularity given their inverse relationship. It is derived by averaging 2D roundness values measured from three orthogonal projections: front, side, and top, providing a robust approximation of the particle's overall 3D roundness. While 2D roundness alone is sensitive to particle orientation and does not fully capture 3D geometry, this averaging approach mitigates orientation effects and enables consistent and comparable evaluation of shape changes between original and simplified particle models without requiring full volumetric reconstruction. Table 2 summarizes the employed shape descriptors.

Table 2: Selected shape descriptors and definitions

Descriptor	Equation	Dimension	Range	Reference
Sphericity	$\varphi = \frac{\pi^{\frac{1}{3}}(6V_p)^{\frac{2}{3}}}{S_p}$, where V_p and S_p describe the particle's volume and surface area.	3D	[0,1]	[70]
Convexity	$Convexity = \frac{V}{V_{CH}}$, where V_{CH} is the volume of the convex hull	3D	[0,1]	[43]
Roundness	$R = \frac{1}{n} * \frac{\sum_{i=1}^{n} r_i}{r_{ins}}$, where r_i is the corner radius, r_{ins} is the radius of the maximum inscribed circle	2D	[0,1]	[70]

2.3 Conclusion

This chapter reviews three prominent particle shape modelling methods, multi-sphere, polyhedral, and super-ellipsoid, alongside essential shape descriptors, with the goal of identifying the most suitable modelling approach and critical shape descriptors for showing simplified particle geometries and precisely quantifying their deviation from original particle shapes.

Shape Modelling Methods
The multi-sphere model, while computationally efficient for DEM simulations given simplified contact detection, inherently generates surfaces that are featured by rounded protrusions, giving poor approximations of sharp edges and flat faces. Its dependence on overlapping spheres restricts geometric fidelity, especially for angular particles. On the other hand, the super-ellipsoid model provides mathematical flexibility for smooth, parameterized shapes but has difficulty in accurately capturing discrete planar facets and concavities typical of natural irregular particles. In contrast, the polyhedral model stands out at representing angularity, flat surfaces, and sharp edges through its application of triangular planes, vertices, and edges. While computationally intensive for DEM simulations, this drawback is less important in physical 3D printing contexts, where geometric precision takes precedence over algorithmic efficiency. Thus, the polyhedral model is chosen as the most suitable method here, as it protects essential morphological features and supports accurate quantification of deviations in simplified particle geometries.

Shape Descriptors
To quantify deviations in particle morphology between original and simplified shapes, most attention was allocated to 3D shape descriptors given their invariance to particle orientation, guaranteeing continuous measurements regardless of spatial positioning. Sphericity (using Wadell’s formulation) and convexity (expressed as the volume-to-convex-hull ratio) offer comprehensive metrics evaluating overall form and surface compactness, practically encompassing deviations from idealized geometries. Roundness, which inversely correlates with angularity, was approached in 3D by averaging 2D roundness values measured from three orthogonal projections (front, side, and top), giving a consistent estimate of particle roundness to stimulate comparison between original and simplified models. Flatness and elongation were ignored, as their geometric effects are inherently captured by sphericity through the axial ratios (b/a and c/b). While these ratios can contain additional detail beyond a single sphericity value, this information is not necessary for quantifying the effect of irregular particle shape on bulk behaviour, providing a reference for DEM simulations where ideal spheres are commonly employed, and helping to improve their accuracy.

Together, these findings directly relate to the sub-question, “Which shape modelling method and shape descriptors most accurately capture and quantify the geometry of irregularly shaped particles?” This study shows that the polyhedral modelling approach, in combination with the following shape descriptors: sphericity, convexity, and roundness, offers the most effective and comprehensive framework for representing simplified particle geometries and quantifying their deviations from original shapes.

3 Impact of Simplification on Particle Shape and Volume

As discussed in Chapter 2, this thesis adopts the polyhedral method for shape modelling due to its superior ability to capture flat surfaces and sharp edges of irregular particles. To quantify particle morphology, the chosen shape descriptors are sphericity, convexity, and roundness. Besides, the study examines the way simplification affects particle volume to review the effect of shape simplification on physical properties as well. Volumes of the original and simplified models are obtained by adding their STL files into SolidWorks and pulling out the computed volume from the CAD environment.
This chapter concentrates on sinter particles as the representative irregular particle type and deals with the sub-research question, "*How does the level of geometric simplification impact the shape descriptors and volume relative to the original particle?''*

From the overall population, a single representative shape and size is chosen for detailed examination. Although size distribution has an impact on bulk flow behaviour, this falls out of the scope of this study. This work concentrates rather on the geometric simplification of one representative particle to examine how shape approximations impact bulk flow behaviour. The original sinter particle is simplified as a polyhedral model using MeshLab. The shape descriptors sphericity and convexity are calculated with the MATLAB code offered in Appendix B, while roundness is computed as the average of the 2D roundness at three orthogonal projections using a separate MATLAB script shown in Appendix C.

In order to quantify the effect of geometric simplification on particle shape and volume, a series of models with progressively decreased mesh resolutions is investigated. These simplification levels entail the original particle model (~400,000 faces) and simplified versions with 40,000; 10,000; 4,000; 1,000; 400; 300; 200; 150; 100; 80; 60; and 40 faces. For each model, the values of the selected shape descriptors, sphericity, convexity, and roundness, including particle volume, are calculated to review the extent to which simplification alters geometric fidelity. Appendix D offers visualizations of the models for each simplification level.

3.1 Shape Descriptors and Volume by Simplification Level

3.1.1 Sphericity

The sphericity plot (Figure 19) shows that for mesh resolutions exceeding 400 faces the changes in sphericity are relatively small, while simplifications below this level correspond to a more noticeable increase in sphericity.

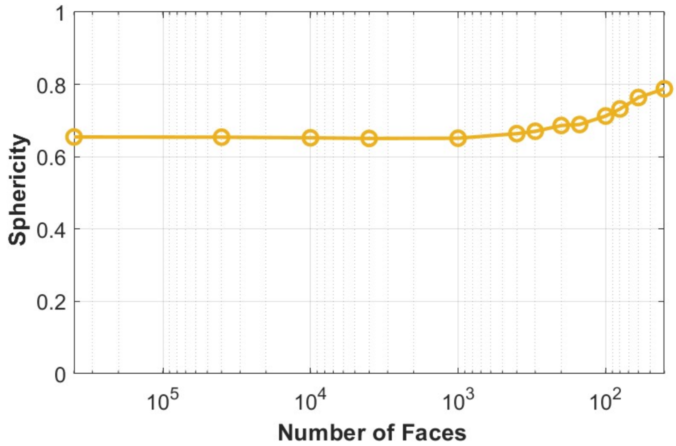

Figure 19: Sphericity vs. Number of Faces

In order to comprehend the impact of simplification on the sphericity of the particle at various levels, initially there has to be a quantitative-qualitative classification of the meaning of certain sphericity values (Table 3).

Table 3: Sphericity categorization [44]

Category	Range
Low Sphericity	0.35–0.45
Medium Sphericity	0.45–0.60
Spherical (Equant)	0.60–0.80
High Sphericity	0.80–1.0

These ranges provide a numerical scale to examine how spherical a particle is, which is crucial for comparing changes under simplification processes.

In addition, Figure 20 gives a visual interpretation of sphericity by plotting particle shapes through both sphericity (vertical axis) and roundness (horizontal axis). The sphericity scale is demonstrated at values of 0.3 (low), 0.5 (medium), 0.7 (high), and 0.9 (ultra sphericity).

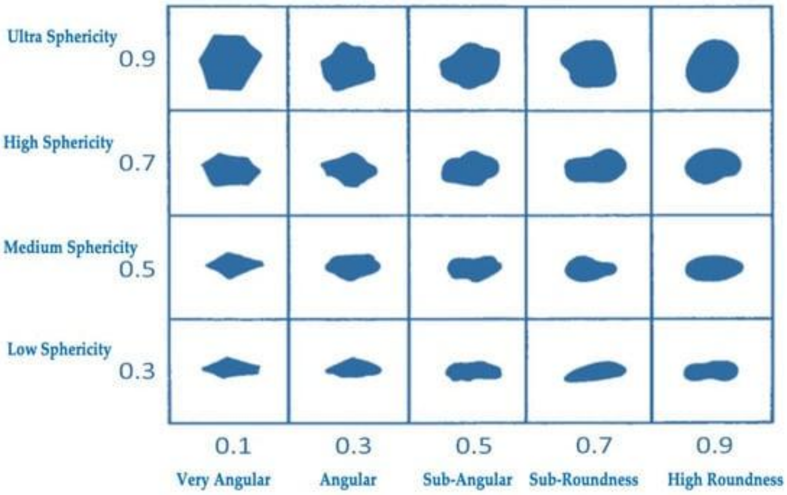

Figure 20: Classification chart based on roundness and sphericity of particles [82]

The original shape (~400,000 faces) has a sphericity of ~0.66, which rises to 0.79 at 40 faces and converges to ~0.65 at higher resolutions (Appendix D). The particle remains within the Spherical/Equant class (0.60–0.80) across all resolutions. Sphericity is most sensitive to face count between 40 and 400 faces, while above 400 faces the values converge, indicating that the main morphological features are already captured.

3.1.2 Convexity

Figure 21 shows that the convexity increases from 0.66 to 0.80 (for 400,000 to 40 faces, Figure 22). As the resolution increases from 400 to 400000 faces, corresponds to an slight decrease of convexity from 0.68 to 0.66 (~1.63% decrease). This suggests that as the mesh resolution increases, changes in convexity become smaller, converging toward a value of 0.664.

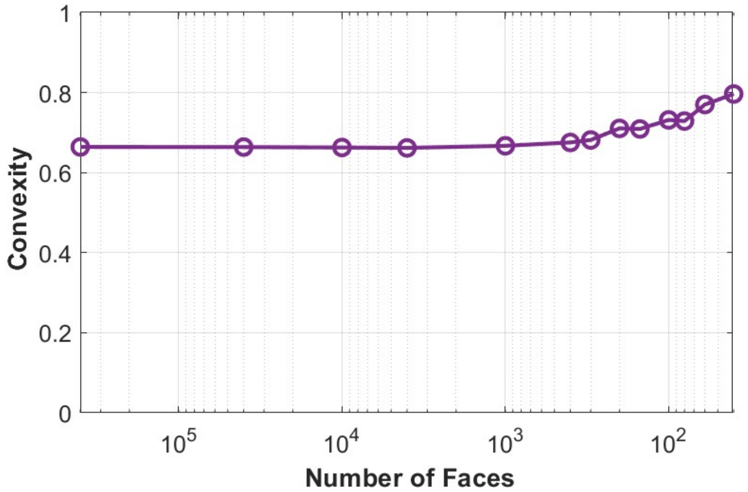

Figure 21: Convexity vs Number of Faces

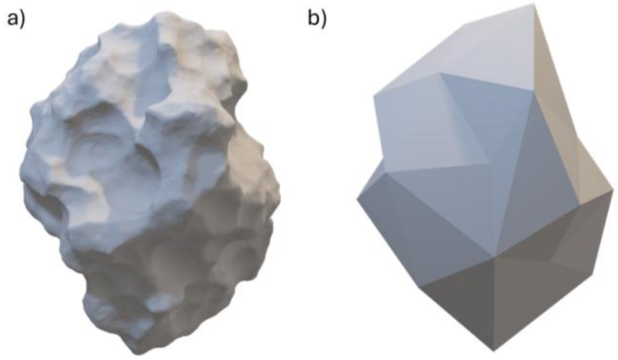

Figure 22: a) Original sinter particle shape (~ 400000 faces); b) Simplified sinter particle shape (40 faces)

In the range (400-40) faces, this shape descriptor has a ~16.2% increase from 0.68 to 0.80. This happens as coarser meshes usually "fill in" concave features, effectively making the particle more convex (Figure 23). Therefore, simplification causes the particle's shape to more closely look like its convex hull.

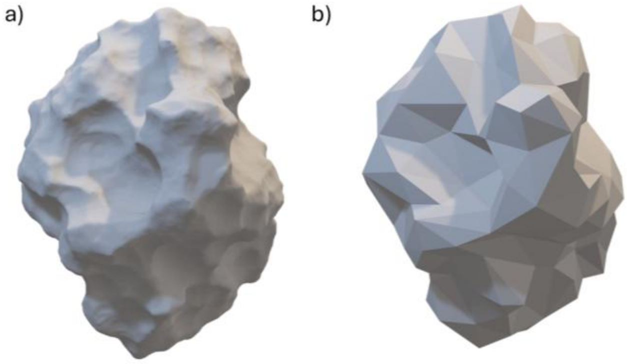

Figure 23: a) Original sinter particle shape (~ 400000 faces); b) Simplified sinter particle shape (400 faces)

In short, convexity is relatively stable at higher resolutions, with only minor deviations above 400 faces, while coarser meshes below this range progressively increase convexity by smoothing concavities and edges, causing the particle's shape to resemble its convex hull more closely.

3.1.3 Roundness

In general, roundness values are implemented to quantify the smoothness or angularity of a particle's edges and corners. The following standard descriptive categories exist is shown in Table 4.

Table 4: Roundness categorization [44]

Category	Range
Very angular	0.12-0.17
Angular	0.17-0.25
Subangular	0.25-0.35
Subrounded	0.35-0.49
Rounded	0.49-0.7
Well rounded	0.7-1

The roundness plot (Figure 24) demonstrates the convergence of the particle's roundness after the resolution of 400 faces is surpassed. Beyond this resolution, the roundness value converges around 0.14, which falls under the category 'very angular'. This shows that further rises in the number of faces have little effect on roundness.

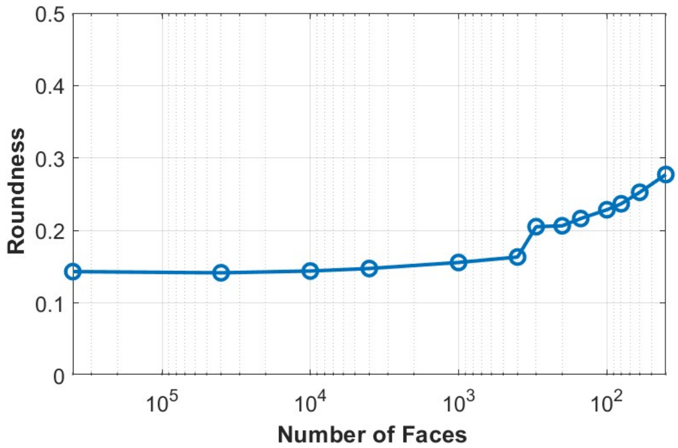

Figure 24: Roundness vs. Number of Faces

However, when the mesh simplification is below the resolution of 400 faces, the roundness increases. The particle is classified as 'very angular' at 400,000–400 faces (roundness 0.14–0.16). Reducing the mesh to 40 faces increases roundness to 0.28, changing its classification from angular to subangular. This reflects the smoothing of corners and edges, with qualitative effects on roundness occurring mainly below 400 faces.Once the mesh resolution is more than 400 faces, the particle roundness classification remains the same as that of the original particle.

3.1.4 Volume

Figure 25 showcases the correlation between particle volume and mesh resolution under simplification levels from 400000 to 40 faces.

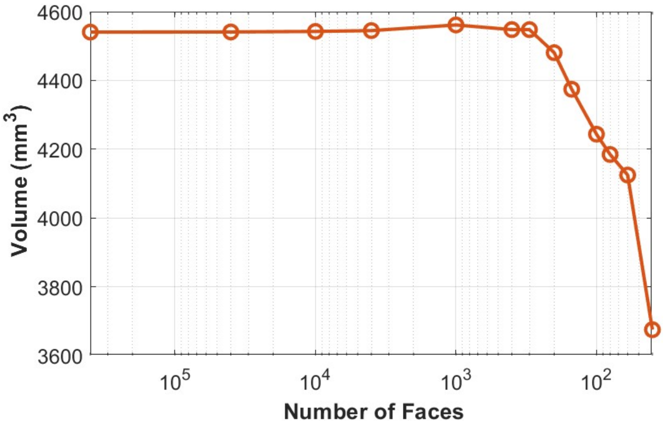

Figure 25: Volume vs. Number of Faces

At the original shape (400,000 faces), the particle has a volume of 4540.55 mm³. As the number of faces drops, volume initially remains roughly the same. From 400,000 down to 400 faces, volume changes only slightly between 4540 and 4547.72 mm³.

As simplification goes on below 400 faces, volume starts to decrease further. At 200 faces, volume decreases to 4480.61 mm³, showing a ~1.3% underestimation relative to the original model. This trend becomes more intense at lower resolutions: at 40 faces, volume drops sharply to 3675.01 mm³, corresponding to a 19.1% reduction. This loss is due to the removal of concavities and finer surface features, resulting in an oversimplified geometry which doesn't reflect the particle's true physical form.

Nevertheless, this study strives to understand the way in which shape simplification impacts bulk flow behaviour. For such an examination to be valid, it is essential that shape remains the only changing variable. This means that the particles across various simplification levels need to be scaled to the volume of the 400,000-face model.

3.1.5 Overall Shape Convergence and Threshold Resolution

Building on the individual analyses of sphericity, convexity, roundness, and volume, this section synthesizes their combined behaviour given progressive simplification. Table 5 exhibits the relative changes in the three key shape descriptors sphericity, convexity, and roundness together with the overall average of their absolute relative changes. In this case, the average of their absolute relative changes serves as a composite indicator for overall shape alteration.

The relative changes in sphericity, convexity, and roundness were calculated by subtracting the metric value at the highest resolution (400,000 faces) from its corresponding value at each level of simplification, and then dividing this difference by the original (400,000-face) value. The specific values of these metrics are given in Appendix E. The average absolute shape change was obtained as the mean of the absolute values of these three relative changes, thus working as an integrated composite indicator that quantitatively demonstrates the overall morphological deviation of the simplified particle models from the original reference geometry. Here, an unweighted mean of the absolute relative changes in sphericity, convexity, and roundness is assumed to provide a robust, fully reproducible, and standardized measure of overall morphological deviation.

Following the benchmark from a study [83] that used a 5 % relative error threshold as a practical criterion for identifying the level of geometric accuracy, further refinement results in negligible improvements. While their study concentrated on clump models of sand, ballast, and cobbles for DEM, and not 3D-printed sinter polyhedra, the underlying principle, that a small relative change indicates a morphological plateau, is equally relevant.

Accordingly, the same 5% criterion is assumed here as a practical threshold to identify the mesh resolution at which further geometric refinement yields negligible changes in particle shape.

As shown in Table 5, the average absolute shape deviation decreases from 44.6% at 40 faces to 5.7% at 400 faces, after which improvements become minimal (< 3% at 1000 faces and < 1% for higher resolutions). This convergence trend shows that the geometric fidelity of the model stabilizes at approximately 400 faces, defining it as the threshold resolution.

Table 5: Relative changes in shape descriptors across various levels of shape simplification

Number of faces	sphericity change(%)	convexity change(%)	roundness change (%)	average absolute shape change (%)
40	20.34	19.92	93.50	44.59
60	16.64	15.95	76.40	36.33
80	11.83	9.75	65.33	28.97
100	8.85	10.16	59.56	26.19
150	5.25	6.78	51.09	21.04
200	4.83	7.00	44.11	18.65
300	2.40	2.62	43.25	16.09
400	1.40	1.69	14.05	5.71
1000	-0.53	0.43	8.79	3.25
4000	-0.62	-0.35	3.00	1.32
10000	-0.36	-0.21	0.56	0.37
40000	-0.09	-0.05	-1.14	0.43
400000	0.00	0.00	0.00	0.00

3.2 Conclusion

This chapter examined the sub-research question:
“How does the level of geometric simplification impact the shape descriptors and volume relative to the original particle?”

The results make it clear that mesh simplification quite affects both morphological descriptors and physical properties when resolution decreases below a critical threshold:

- **Sphericity** increases from 0.65 (at 400,000 faces) to 0.79 (at 40 faces) as mesh resolution decreases. Despite this increase, the particle remains within the 'Spherical/Equant' classification across the tested range (400,000- 40 faces). This suggests that the overall particle sphericity is largely preserved.
- **Convexity** increases from 0.66 to 0.80 (400,000 to 40 faces). This indicates that the shape becomes more convex at lower face count. At higher face counts (>400 faces), it converges around 0.66.
- **Roundness** increases as mesh resolution decreases, with the particle classified as ‘very angular’ (for 400,00 – 400 faces), ‘angular’ (for 300-60 faces), and ‘sub-angular’ (at 40 faces). This trend indicates that reducing the mesh resolution below 400 faces is associated with a qualitative increase in roundness.
- **Volume** remains largely consistent (within ±0.16% deviation) for meshes with 400 faces or more but starts to decrease more strongly at lower resolutions (below 400 faces), reaching a 19.1% underestimation at 40 faces.

The threshold resolution is quantified via analysis of the combined shape metrics (sphericity, convexity, and roundness), where it is shown that this average absolute shape change increase for mesh resolutions below the 400 face model. When increasing the number of faces beyond 400 faces, the combined shape metric remains below the 5% threshold, indicating that the geometric fidelity compared to the original model stabilizes.

In summary, shape simplification primarily affects the shape descriptors below an approximate threshold of 400 faces, while above this range (400–400,000 faces) the descriptors remain largely stable. In parallel, particle volume decreases with decreasing number of faces, reflecting the loss of fine surface features and concavities.

4 3D Printing of Simplified Particles

As concluded in the preceding chapter, geometric simplification changes particle morphology to a certain extent, which later may affect bulk flow behaviour. To experimentally isolate and review this effect, simplified particles must be physically regenerated while guaranteeing that factors such as particle volume and mass remain consistent with the original reference particle. If this physical fidelity is lacking, any observed differences in flow behaviour could not be connected merely to shape changes.

In this chapter, the focus is on the following sub-research question: "*How to 3D print simplified shaped particles in bulk with matched volume and weight to the original particle?*" By using and developing the morphological analysis, three representative simplification levels are chosen, 40, 100, and 400 faces, covering the range from highly simplified to morphologically accurate. These models offer a thorough basis for examining shape effects on bulk flow.

To 'convert' these digital models into physical test particles, Fused Deposition Modelling (FDM) is used as the printing method. FDM gives the necessary resolution and material consistency to regenerate small, irregular particles with controlled density. Nonetheless, the fabrication process comes with additional challenges: simplified models inherently stand out in volume from the original particle, and variations in print infill can change mass. To solve this issue, a systematic calibration approach is developed. Firstly, each simplified model is uniformly scaled to the original particle (400,000-face model) volume. Hereafter, infill ratios were empirically adjusted and calibrated to obtain mean particle masses close to the target value of 3.69 g, with all deviations staying within the 95% confidence intervals.

Finally, a bulk printing plan was carried out, producing 1000 particles per simplified model across multiple printers, applying standardized parameters (0.4 mm nozzle, 0.2 mm layer height) and colour-coded filaments for clear distinction between the different models. This approach guaranteed reproducible mass and dimensional accuracy while isolating particle shape as the sole variable for subsequent bulk flow experiments.

4.1 3D printing Approach

3D printing, or additive manufacturing, is a layer-by-layer fabrication technique under which a computer-controlled system builds three-dimensional objects on a flat build platform [84–86]. Here, Fused Deposition Modelling (FDM) was applied to fabricate simplified particles to keep full consistency with the original FDM-printed reference particles. In FDM, a thermoplastic filament, particularly polylactic acid (PLA), is heated to a semi-molten state and extruded through a precision nozzle, where successive layers fuse upon cooling to construct the desired particle geometry [84].

Printed objects are typically not made as fully solid volumes. Rather, they consist of a continuous outer wall that sets out the surface geometry and gives structural strength, even though the interior is either left hollow or filled with a honeycomb-like infill structure to stimulate the walls using minimal material. Since infill density directly controls mass, it was altered to match the original particle's weight while maintaining its geometric volume. Complex particle morphologies mostly have unsupported or overhanging regions that cannot be printed directly. To keep dimensional accuracy, temporary support structures are automatically produced during the FDM process to stabilize these areas. Although necessary, these supports increase both material consumption and printing time.

Two FDM printer models were used here, one Original Prusa XL and three Bambu Lab A1 units, with specifications summarized in Table 6. Both types of FDM printers must have the same layer height and nozzle diameter in order to guarantee that the 3D-printed particles have the same printing quality [87]. The available printers were used simultaneously to speed up the printing process.

Table 6: 3D printer models and parameters

	Original Prusa XL	**Bambu Lab A1**
Technology	FDM	FDM
Build area	360x360x360 mm	256x256x256 mm
Layer height	0.2 mm	0.2 mm
Nozzle diameter	0.4 mm	0.4 mm

4.2 Selection of Simplified Models

In Chapter 3, key shape descriptors and physical properties (particle volume and weight) were examined regarding the number of faces used in mesh simplification.

The analysis uncovered how geometric simplification affects both the morphological and physical fidelity of an irregular sinter particle. Simplification under 400 faces significantly changes the particle's roundness, sphericity, and convexity, smoothing features and thereby decreasing shape fidelity. Likewise, volume is underestimated at lower resolutions, with accuracy sharply augmenting and stabilizing at ≥400 faces. While a broad range of simplification levels was originally made (400,000; 40,000; 10,000; 4,000; 1,000; 400; 200; 150; 100; 80; 60; 40 faces), experimentally testing all of them through 3D printing and flow analysis would necessitate excessive material and time. Furthermore, the shape descriptors for models above 400 faces displayed minimal variation, meaning that their influence on bulk flow behaviour would likely be equivalent. Nevertheless, between 400 and 40 faces, changes in shape descriptor values are still pronounced, making this range critical for examination. As such, three representative simplified models were picked out for the study: the most simplified model (40 faces), an intermediate model (100 faces), and a threshold model (400 faces).

4.2.1 400 and 40 Face Model

The 400-face model (Figure 26) was chosen as the threshold model. At this level, the particle is categorized as ‘very angular’, which is the same category as that of the original particle. From this resolution the deviations in convexity compared to the original particle shape are less than 2%, showcasing that the model accurately retains structural concavities without overfilling them. The same is true for sphericity, where the value deviations are less than 2%, having the values stay well within the same morphological category (spherical/equant), and showing a balance between simplification and shape fidelity. These stable and realistic shape descriptor values indicate that the 400-face model may cover the essential geometrical features of the original irregular particle, turning it into the most convenient representation for examining shape effects on bulk flow behaviour without introducing distortions due to over-simplification.

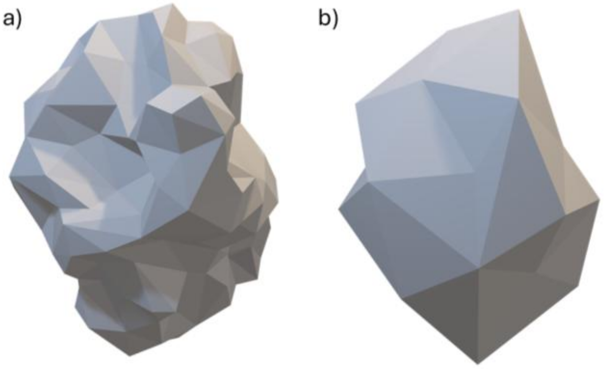

Figure 26: a) Threshold Model (400 faces); b) Most Simplified Model (40 faces)

The 40-face model (Figure 26) is the most simplified model used in this study. At this level of simplification, geometric accuracy is highly reduced. At this mesh resolution, the particle roundness can be classified as ‘subangular’. This is a significant change in roundness as the original particle is classified as ‘very angular’. The convexity at this level reaches the value of 0.80, which is higher compared to the value of 0.66 (at 400000 faces). Sphericity increases to 0.79, approaching the upper end of the spherical/equant category.

These changes show a considerable departure from the original geometry but have an important role in the study by exhibiting the morphological simplification. The 40-face model allows for the review of the extent to which heavily smoothed shapes affect bulk flow behaviour, giving a clear contrast to higher-fidelity representations.

4.2.2 100 Face Model

In order to choose the intermediate model within the range of (400 to 40) face models, the mean values of the key shape descriptors were first calculated (Equations 8-10). This approach ensures that the intermediate representation is chosen based on objective criteria.

$$\psi_{mean} = \frac{0.78777 + 0.66377}{2} = 0.72577 \tag{8}$$

$$C_{mean} = \frac{0.79635 + 0.67532}{2} = 0.73584 \tag{9}$$

$$R_{mean} = \frac{0.2772 + 0.1634}{2} = 0.22032 \tag{10}$$

These mean values exhibit the target geometric midpoint between the two extremes (400-40 face).

Hereafter, the Euclidean distance [88] was calculated between each candidate model (60-300 faces) and these target means (Equation 11):

$$distance = \sqrt{(\psi - \psi_{mean})^2 + (C - C_{mean})^2 + (R - R_{mean})^2} \tag{11}$$

, where

- ψ: sphericity
- C: convexity
- R: roundness

The Euclidean distance metric gives a multidimensional measure of the distance between the descriptors and their mean value. Candidate models in the 60–300 face range were reviewed; their descriptor values and computed distances are displayed in Table 7.

Table 7: Sphericity, Convexity, Roundness & Distance to the Mean for particle models with different Number of Faces

Number of Faces	Sphericity	Convexity	Roundness	Distance to mean
60	0.76357	0.77003	0.25273	0.0604
80	0.73208	0.72883	0.23687	0.0190
100	0.71255	0.73153	0.22860	0.0162
150	0.68901	0.7091	0.21647	0.0456
200	0.68626	0.71054	0.20647	0.0489
300	0.67033	0.68151	0.20523	0.0791

Here, the 100-face model (Figure 27) has the smallest distance to the mean. Therefore, this model is picked out as the intermediate model.

Figure 27: Intermediate Model (100 faces)

4.3 Volume and Mass adjustment

Particle size affects the bulk flow behaviour of granular materials by changing the force balance between adhesion and gravity. Adhesive interactions come forward primarily from Van der Waals forces in dry systems and liquid bridge forces in moist environments.
Fine particles (<100 µm) show a disproportionately strong cohesion owing to their high specific surface area and produce a greater number of contact points per unit mass. In contrast, bulk materials with larger particles are governed by gravitational forces, enhancing flowability [89,90].

To isolate the effect of particle shape on bulk flow in this study, the simplified particle replicas were designed to closely match the volume and mass of the original reference particles, thus ensuring that only shape, not size or weight, acts as a variable influencing flow behaviour.

4.3.1 Scaling for Volume Adjustment

To guarantee that shape is the only variable affecting bulk flow behaviour, simplified particle models must have the same volume as the original particle. This is obtained via a uniform homothetic scaling transformation, where all linear dimensions of the simplified model are multiplied by a scaling factor (Equation 12) [43]:

$$s = \left(\frac{V_{original}}{V_{model}}\right)^{\frac{1}{3}} \tag{12}$$

This operation keeps geometric similarity while altering the model's volume to match the reference particle. Scaling was done in SolidWorks, and Table 8 shows the original particle volume and the applied scaling factors for each simplified model.

Table 8: Volumes and corresponding scaling factors for simplified models

	Original model	400 face model	100 face model	40 face model
Volume (in mm^3)	4540.55	4547.72	4243.65	3675.01
Scaling factor		0.9995	1.0228	1.0730

4.3.2 Mass Correction via Infill Adjustment

To set apart particle shape as the sole factor influencing bulk flow behaviour, all particle models must have equal mass. The original-shaped particles work as the reference for the target mass that the simplified particles must replicate.
The target mass was identified by randomly picking out and weighing four particles from the original batch (400,000 faces) to get their mean weight. Photographs of these particles are demonstrated in Appendix F. Given the small sample size, the uncertainty was computed using the t-test. The corresponding t-value in this case is 3.182 (N= 4, 95% confidence level, Appendix I, [91]). The mean and standard deviation of the masses were computed in Excel, with the t-value as an input for calculating the uncertainty. The resulting target mass of the original particles is 3.69 g (Table 9).

To make sure that the simplified particles (400, 100, and 40 face models) got the same mass, their infill ratio was changed prior to 3D printing. Since the mass predicted by slicing software in most cases deviates from the actual printed mass, empirical calibration was carried out. This entailed printing sample particles at different infill ratios, measuring their mass, and choosing the ratio that produced an average weight closest to 3.69 g. Nonetheless, variations in 3D printing, especially when multiple printers are used simultaneously, bring with them small deviations from the target mass. The mean weights and uncertainties of the simplified particles are summarized in Table 9.

The deviations in printed mass were quantified by comparing each model's mean weight to the target mass relative to its uncertainty. As shown in Table 9, the 400 face model has an average weight of 3.60 g, 0.09 g below the target, within its uncertainty of ±0.14 g. The 100 face model fits the target exactly (3.69 g, ±0.04 g), and the 40 face model differs by 0.05 g (3.64 g, ±0.11 g). Since all deviations are within the 95% confidence intervals, the variations in mass are statistically insignificant. This proves that any observed variations in bulk flow behaviour can be linked solely to particle shape rather than mass.

Table 9: Mean Weight, Uncertainty and Infill Ratio of Simplified Models

	400000 model	400 face model	100 face model	40 face model
Average weight (g)	3.69	3.60	3.69	3.64
Uncertainty (95% CL) (g)	+/- 0.04	+/- 0.14	+/- 0.04	+/- 0.11
Infill ratio		45%	48%	49%

4.4 Design of the Bulk 3D printing

In order to carry out statistically meaningful bulk flow experiments, 1000 particles were fabricated for each of the three simplified particle geometry models. Producing such large quantities is important for capturing representative bulk behaviour, as shown in previous DEM simulations [92,93].

All particle models were fabricated by applying fused deposition modelling (FDM) with PLA filament to maintain consistent material properties. For consistent printing resolutions across all models, a 0.4 mm nozzle and 0.20 mm layer height was applied.

Different filament colours were used to distinguish the models (Figure 28).

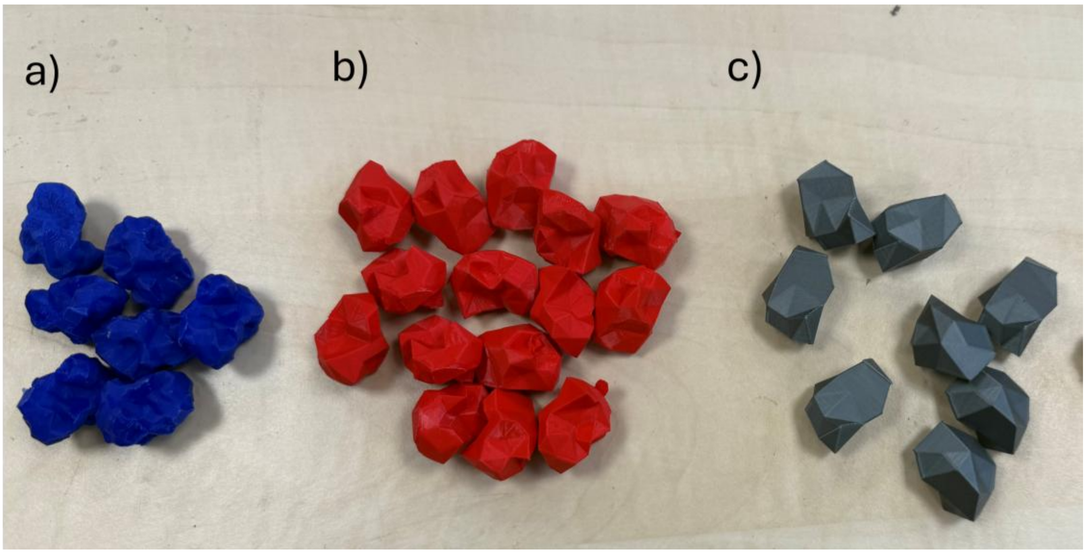

Figure 28: 3D-printed particles a) 400-face model; b) 100-face model; c) 40-face model

Material Budget and Printing Parameters

The required material per batch was estimated by multiplying the mean particle masses and confidence levels per model by the amount of printed particles per model (1000 particles).
To ensure that even in the worst-case scenario there is still enough material, the highest upper bound value of 3750 g (Table 10) and up to 20% support material, the total mass required per model was approximately 4500 g. This approves that one single 4.5 kg PLA spool per model is sufficient for each batch.

Table 10: Bulk mass per model

Model	Average scaled total Mass (g)	95% confidence level scaled (g)	Range (g)
400-face	3600	+/- 140	3460-3740
100-face	3690	+/- 40	3650-3730
40-face	3640	+/- 110	3530-3750

Limitations

The main restriction of the current bulk printing setup comes from the restricted build volumes of the available printers. The Original Prusa XL limited to the production of 100 particles per batch, whereas the Bambu Lab A1 is limited to the production of 50 particles per batch. Consequently, several printing cycles were needed to fabricate the 1,000 particles per model. Printing times also differed depending on particle complexity (Table 11, Appendix H). At a single particle this can vary from 30 to 37 minutes, where the printing time increases with particle complexity. Per batch of 100 particles, this results in durations varying from 1 day

7 hours 26 minutes to 2 days 2 hours 8 minutes. Scaling this up to 1000 particles for each model it takes between 13 and 20 days of continuous operation.

In order to minimize the printing time, three Bambu Lab A1 printers were operated at the same time for the 400- and 100-face models. However, using different printers introduce slight performance differences between individual printers. These inter-printer variations, in combination with repeated batch changes, led to minor discrepancies in particle geometry and weight within each model. For the 40-face model, although only a single Original Prusa XL printer was applied, the printing cycle had to be repeated every 100 particles due to build-area limitations. This repeated cycling likewise brought along small variations in particle weight within the same sample, associated with cumulative differences in filament feed rate, temperature drift, and layer adhesion between consecutive batches. Table 11 shows the parameters for 3D printing the simplified models in bulk.

Table 11: Printing parameters for bulk 3D printing of simplified models

	400 face model	**100 face model**	**40 face model**
Printing Method	FDM	FDM	FDM
3D Printer Model	Bambu Lab A1	Bambu Lab A1	Original Prusa XL
Nozzle Diameter	0.4 mm	0.4 mm	0.4 mm
Layer Height	0.2 mm	0.2 mm	0.2 mm
Infill Ratio	45%	48%	49%
Filament Type/Colour	PLA economy blue	PLA economy red	PLA economy silver
Filament Diameter	1.75 mm	1.75 mm	1.75 mm
Spool Weight	4500 g	4500 g	4500 g
Quantity Printed	1000	1000	1000
Printing time (single particle)	37 minutes	33 minutes	30 minutes
Printing time (100 particles)	2d 2h 8m	1d 14h 10m	1d 7h 26m

4.5 Conclusion

This chapter puts forward a methodology for 3D printing simplified particle replicas with matched volume and mass, making sure that particle shape remains the only variable affecting bulk flow behaviour. Three representative models 40, 100, and

400 faces were picked out based on quantitative analysis of shape descriptors. The 400-face model is the threshold resolution, the 100-face model showcases an intermediate geometric fidelity based on the Euclidean distance to the mean descriptor values between the threshold and simplest model, and the 40-face model exemplifies the lower bound of simplification, giving way to the study of extreme shape smoothing effects. In combination, these models cover a representative range of morphological variability.

To match the original particle's volume, all simplified models were objected to uniform homothetic scaling. Mass equivalence was obtained through empirical calibration of infill ratios during FDM printing, with all deviations staying within the 95% confidence interval of the target mass (3.69 g). Bulk production of 1000 particles per model was executed using standardized FDM parameters (0.4 mm nozzle, 0.2 mm layer height) throughout the printers, guaranteeing dimensional accuracy and reproducible mass. Different filament colours were applied to clearly distinguish the particle types during bulk flow testing: blue for the 400-face model, red for the 100-face model, and silver for the 40-face model.
Material budgeting proved that even under a conservative worst-case scenario, including support structures up to 20% of particle mass, the total filament necessity for 1000 particles remained below 4500 g, guaranteeing that a single PLA spool suffices. The main restriction of this bulk printing process was the limited build volumes of the available printers, which needed multiple cycles and introduced large printing times and variability in particle mass. Large-format industrial FDM systems could print all particles in a single batch, enhancing reproducibility and reducing production time.

In all, the sub-research question, "How to 3D print simplified-shaped particles in bulk with matched volume and weight to the original particle?", is addressed by implementing:

- Homothetic scaling to retain particle volume;
- Empirically calibrated infill ratios to match the target mass, with all deviations staying within the 95% confidence intervals.
- Standardized FDM fabrication parameters to keep dimensional and mass consistency across all simplification levels;
- Material-budget verification to ensure sufficient filament for bulk production, with support structures, among others.

This methodology isolates particle shape as the sole experimental variable, giving a robust foundation for subsequent analysis of bulk flow behaviour.

5 Flowability across varying levels of particle shape simplification

This chapter discusses the sub-research question: *How does the level of simplification influence measurable bulk flow properties such as angle of repose, coefficient of static friction, and Hausner ratio?* To address this sub-question, three complementary flowability indicators angle of repose (AoR), coefficient of static friction (μ_s), and Hausner ratio (HR) are systematically reviewed.

The chapter consists of three stages. First, the theoretical basis, significance, and limitations of each flowability related parameter are reviewed, among which are the mechanisms affecting AoR, the measurement of μ_s applying inclined surface tests, and the evaluation of HR through bulk and tapped densities. Second, the experimental procedures are discussed in detail, including the ledge test for AoR, bulk and single-particle inclined surface tests for μ_s, and HR measurements, all performed under controlled conditions with repeated trials to guarantee statistical robustness.

At the end, the results are presented and interpreted, highlighting how particle simplification influences flowability.

5.1 Flowability Assessment Methods

Flowability is defined as the ability of bulk solid materials to flow. This flowability depends on many physical characteristics. In fact, it is a result of the combination of the materials' physical properties that influence flowability, environmental conditions, and handling, storage, and processing equipment used for these materials. Because of these factors, flowability cannot be fully quantified by a single test, and therefore multiple tests are needed [94,95].

In general, shear testers (such as the Jenike Shear Cell and Ring Shear Tester) can give precise quantitative measurements of flowability. One limitation of these methods is that they are often time-consuming, equipment-intensive, and require large amounts of sample [96–98].

Otherwise, flowability can be quantified indirectly via several parameters that correlate with flowability [95,99]. Here, the flow behaviour of the 3D-printed particles was reviewed through three common parameters: the angle of repose (AoR), coefficient of static friction (μ_{st}), and Hausner ratio (HR).

5.1.1 Angle of Repose

The angle of repose is the maximum angle between the sloping side of a heap of granular material and the horizontal plane at which the material stays stable without sliding or collapsing (Figure 29). It is a key parameter applied to characterize the flowability and packing behaviour of granular materials, including sand, powders, and grain [100,101].

Figure 29: Angle of Repose Representation [101]

The usefulness of the AoR is because of the fact that it is an easily measurable property that is related to harder to get properties, like the interparticle friction, and can thus be used to roughly characterise the flow behaviour of powder and granular materials (Table 12).

Table 12: Flowability description based on the angle of repose [2,101]

Description	**Angle of repose (°)**
Very free flowing	25-30
Free flowing	30-38
Fair flowing	38-45
Cohesive	45-55
Very cohesive	>55

A common problem when measuring the AoR is that not all materials can become neat, cone-shaped piles with clear side angles. This is exhibited in Figure 30, where the AoR is marked as α. This issue often occurs with sticky materials, materials made of very sharp-edged particles, or materials with a wide mix of particle sizes, which can lead the particles to separate into layers [2,89].

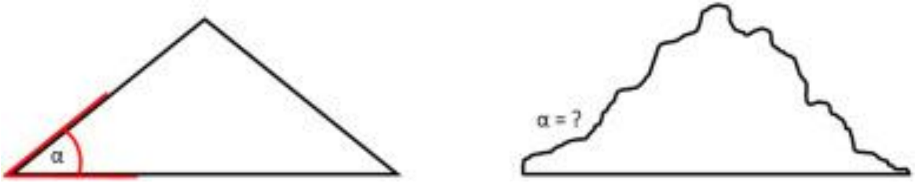

Figure 30: 'Ideal' vs. 'non-ideal' conical heaps of bulk material [101]

To deal with these complexities, the AoR is described as the steepest average slope of a distinct area of the unconfined material, measured from the horizontal plane on which the material can be heaped without collapsing [101]. This definition is implemented in the MATLAB (Appendix H), which ensures objective and reproducible measurements. These processing steps are illustrated in Figure 31 (a-e). First, the image is taken, and its background is edited to a green colour. This enables the code to distinguish between the particles and the background. Note: If the particles aren't white or grey, their colour must be edited to white before inputting this image into the MATLAB code. After editing the image, a cropped region of interest is selected that contains only the discharged portion of the material. This ensures that exclusively the slope relevant for the AoR will be analysed. The image is processed in MATLAB using color-based segmentation to create a binary image, from which heap edges are extracted and fitted with a linear regression line. The slope of the fitted line is converted into the AoR by applying the arctangent function.

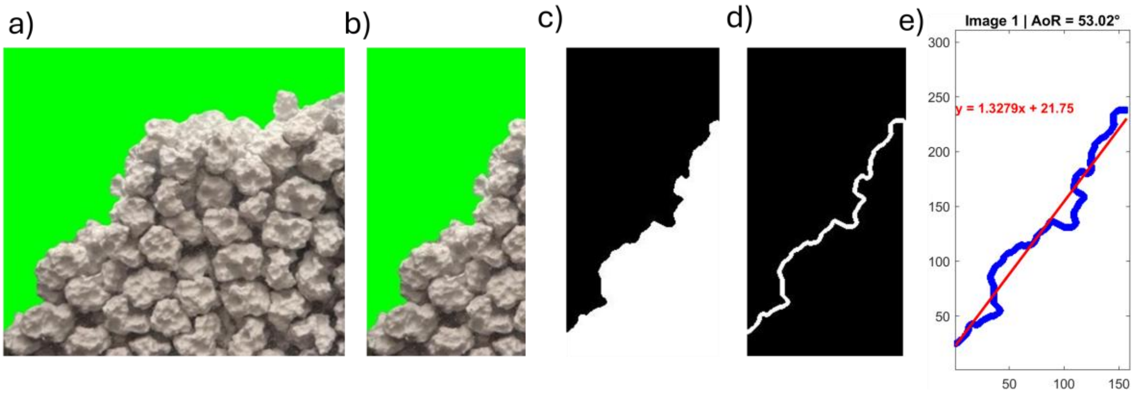

Figure 31: Image-processing steps: a) full image with edited green background; b) cropped region of interest; c) binary image after colour-based segmentation; d) extracted edge; e) extracted edge points (blue) and linear fitted line (red), to calculate AoR

Another limitation is that even though the AoR is used to characterize flowability, its value differs from the measurement method, as it is not an intrinsic material property [2,101]. According to [102], three mechanisms affect the measured AoR: (1) wall sliding of particles along the bottom surface, dominated by wall friction; (2) local avalanches caused by individual particles rolling down the heap; and (3) unstable shear surfaces within the heap, governed by the material's internal friction (Figure 32).

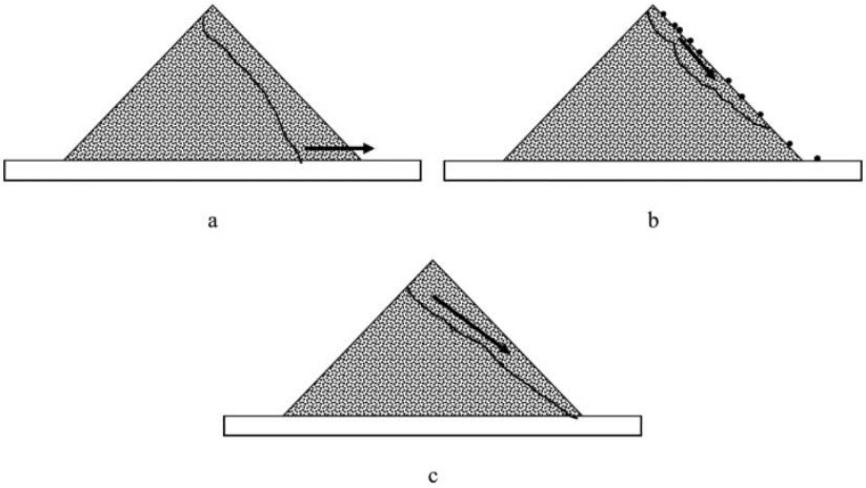

Figure 32: Mechanisms affecting AoR a) wall sliding; b) individual particle rolling; c) internal friction avalanches [102]

Among these, only the third mechanism exhibits the material's true flowability. Thus, experimental methods should reduce as much as possible the influence of wall sliding and local avalanches to isolate the internal friction effect. Here, the ledge test method is used for this purpose.

1. Ledge Test Method

The ledge test, also known as the ‘shear box’ [103] or the ‘rectangular container test’ [104], is used to determine the AoR.

The procedure follows these steps:

1) A rectangular container (200 × 140 × 200 mm) with the front gate. This container has a fixed width of 140 mm to keep an appropriate particle size-to-box width ratio and diminish wall effects (Figure 33). A tripod guarantees stable camera positioning across tests (Figure 34).

Figure 33: Filled ledge test box, with 40-face particles

2) The container is filled with particles while the front gate stays closed.
3) The front gate is quickly opened, allowing material to discharge freely from one side. Once the flow ceases, a stable slope forms inside the container.
4) A front-view image of the heap is obtained through the transparent wall. This image will go through the process as illustrated in Figure 31.

These steps are repeated 15 times per model under identical conditions. After each run, the container is emptied and refilled to ensure consistent packing. The final AoR is noted as the mean value with a 95% confidence interval, computed using the appropriate *t*-value.

Figure 34: Experimental setup of the ledge test

5.1.2 Coefficient of Static Friction

The coefficient of static friction (μ_s) is known as the ratio of the maximum static frictional force to the normal force between two contacting surfaces at rest. It demonstrates the resistance to the initiation of motion and correlates inversely with flowability. Higher μ_s values indicate poorer flowability [105,106].
Here, μ_s was measured using an inclined surface tester (Figure 35) at two scales: the bulk particle level and the single-particle level. The inclined surface tester determines the wall friction angle (θ_w), by steadily inclining the surface until sliding takes place. The coefficient of static friction is then computed using the relation (Equation 13):

$$\mu_s = \tan(\theta_w) \tag{13}$$

Where, μ_s is the static friction coefficient, and θ_w is the measured wall friction angle. This inclined surface tester has an accuracy of 0.3° [107] and displays the wall friction angle with one decimal. A more significant source of error is determining when the sliding starts.

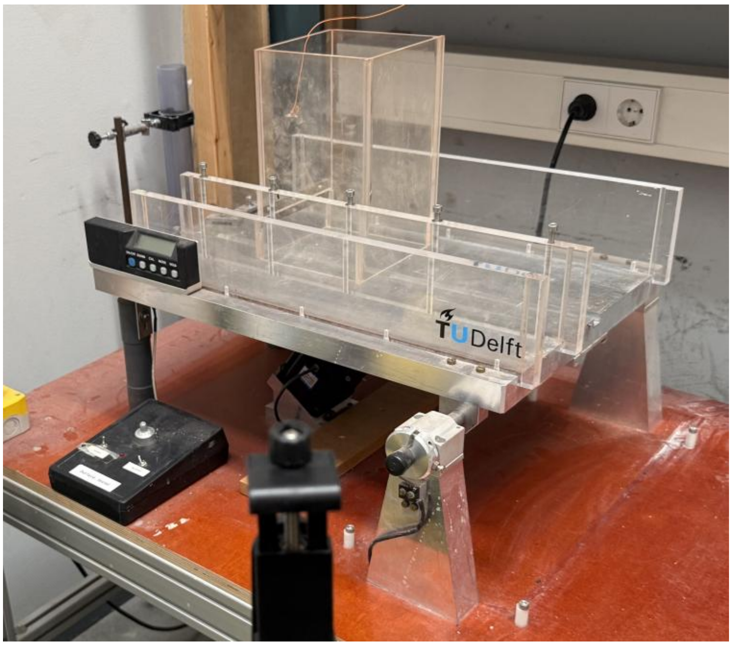

Figure 35: Side view of the inclined surface tester. The transparent box (test box) is used only for the bulk material tests.

Single-Particle Tests:

For single-particle measurements, the procedure was repeated 15 times per model by employing a single 3D-printed particle placed on the steel test surface. Two variants of the experiment were performed:

1. **Random placement test:** For each simplification level, a new particle was put on the table each time the previous one slid off. Both the particle's position and orientation were randomized.
2. **Controlled placement test:** An identical particle (per simplification level) was employed throughout, positioned and oriented identically for all repetitions. The location and orientation of the particle on the surface tester are shown in Figure 36.

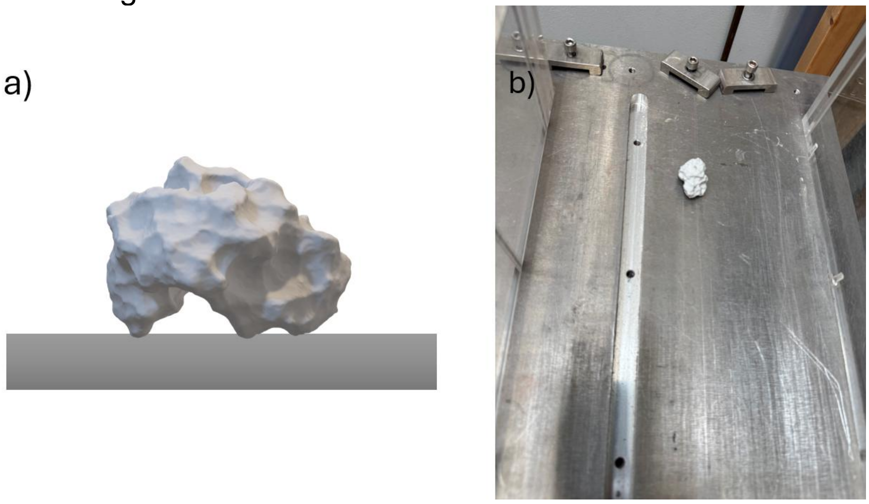

Figure 36: (a) Side view and (b) fixed position and orientation of the particle on the inclined surface used in the controlled placement test.

This comparison isolates the influence of particle positioning and orientation on the measured wall friction angle. All tests were video-recorded, and frame-by-frame analysis was carried out to accurately identify the onset of sliding and the corresponding inclination angle.

Bulk Material Tests:
In the bulk material tests, the test box was filled with 3D-printed particles to a height of 140 mm and leveled so the top surface was parallel to the base, yielding a material volume of (140 × 140 × 140 mm³), as shown in Figure 37. The inclination angle was augmented steadily until bulk sliding took place. The procedure was repeated 15 times for each particle simplification level and for the original particle shape. It should be noted that the test box was made of transparent plexiglass, which rests on a steel base. The static coefficient of friction of plexiglass on steel is reported as 0.3–0.4 [108]. It is assumed that this value is lower than the coefficient of friction of the bulk 3D-printed particles on steel. Thus, the plexiglass–steel interface might not significantly affect the measurements, and the measured coefficient of static friction primarily reflects the particle–steel interactions.

Figure 37: Transparent Box filled with 3D-printed 400,000-face model particles

The mean coefficient of static friction and its 95% confidence interval were computed from these repeated measurements using the appropriate t-value.

5.1.3 Hausner Ratio

The Hausner Ratio (HR) quantifies the degree of particle compaction and cohesiveness, offering an indirect measure of bulk material flowability. It is seen as the ratio between the tapped density (ρ_{t}), the density after compaction, and the bulk density (ρ_b), the density of the material in a loose, aerated state (Equation 14):

$$HR = \frac{\rho_T}{\rho_B} \tag{14}$$

A higher HR shows greater interparticle friction and poorer flow performance. According to [102] , HR values can be divided into categories (Table 13). Materials with HR < 1.11 show excellent flowability, while values above 1.59 correspond to extremely poor flow behaviour.

Table 13: Flowability classification based on HR [102]

HR	Flowability
<1.11	Excellent
1.11-1.18	Good
1.18-1.25	Fair
1.25-1.34	Passable
1.34-1.45	Poor
1.45-1.59	Very Poor
>1.59	Very Very Poor

Bulk Density Measurement:

Bulk density (ρ_b) is the density of a granular material in an uncompacted state. In this study, it is obtained by gently pouring a known mass of material into a 2000 mL measuring cylinder from a height of approximately 100 mm to minimize pre-compaction. The mass (m) and unsettled volume (V_0) are recorded, and the bulk density is computed as (Equation 15):

$$\rho_b = \frac{m}{V_0} \tag{15}$$

Tapped Density Measurement:

Tapped density relates to the bulk density of a powder after compaction by tapping. It is measured by putting a known mass of powder into a graduated cylinder and frequently tapping it until the volume stabilizes. Commercial tapped density testers are usually applied for automated and standardized tapping; on the contrary, a manual tapping method is employed in this paper because a tapped density tester is unavailable.

Following the procedure from [109], a known mass of material was put in the same 2000 mL cylinder and tapped vertically 180 times against a rigid surface until the volume stabilized. The final volume (V_t) was then measured, and the tapped density was computed as (Equation 16):

$$\rho_T = \frac{m}{V_T} \tag{16}$$

The experimental procedure is as follows:

1) Take a 2 Liter cylinder, with a resolution of 20 mL.
2) Weigh the empty cylinder 5 times with a one-decimal accuracy and record the mean mass.
3) Pour the particles into the measuring cup until an initial volume of 1L (V_O) is reached. Note: Pour these particles 100 mm above the brim of the cylinder to avoid excessive pre-compaction.
4) Perform manual tapping by vertically striking the cylinder against a rigid surface 180 times.
5) Measure the final tapped volume (V_T).
6) Weigh the filled cylinder to one decimal place.
7) Find the particle mass by subtracting filled cylinder mass by the mean empty cylinder mass.
8) Calculate the bulk density by dividing the particle mass by (V_O).
9) Calculate the tapped density by dividing the particle mass by (V_T).
10) Use the measured bulk and tapped densities to calculate the HR.
11) Repeat steps 1-10 five times for each simplification level and for the original shaped particles.

The mean HR and its 95% confidence interval (using the corresponding t-value from the t-table) are calculated based on these repeated measurements.

5.2 Experimental Design

To systematically review the extent to which particle simplification affects flowability behaviour, a structured experimental program was made (Table 14). The program includes four complementary tests the ledge test, bulk and single-particle inclined surface tests, and Hausner ratio measurement, which together cover the static, frictional, and compaction-based elements of granular flow.

Each experiment was done under controlled conditions, with multiple repetitions to maintain statistical robustness.

Table 14: Experiment Design

Experiment	Setup	Repetitions (per model)	Output parameters
Ledge Test	Rectangular container (200 × 140 × 200 mm); front wall functioning as door; transparent wall; MATLAB image processing toolbox; tripod with camera	15	Mean AoR +/- 95% CL
Inclined Surface Tester	Motor-driven steel surface tilting bed with steel surface; video recording for sliding detection; transparent test box for bulk sample	15	Mean μ_s+/- 95% CL
Hausner Ratio (HR)	2000 ml plastic measuring cylinder; 1L material; precision balance *(±0.1 g)*; manual tapping *(180 strikes)*	5	Mean HR +/- 95% CL

5.3 Test Results

This section shows the effects of particle geometry simplification on flowability, examined through angle of repose, coefficient of static friction, and Hausner ratio. All measurements were first validated by relative uncertainty and compared with literature to guarantee reliability. The following subsections detail the results (for more details see Appendix J).

5.3.1 Angle of Repose

The angle of repose was measured throughout four levels of particle simplification to examine the way in which a reduction of the number of faces would affect flow behaviour.

Measurement Accuracy and Validation:

Measurement precision was reviewed using relative uncertainty, computed as the ratio of measurement uncertainty to the mean AoR, expressed as a percentage. Throughout all simplification levels, relative uncertainties varied from 4.45% to 6.42% (Table 15) showing good precision. For validation, these uncertainties were compared with literature values: [21] reported for the 3D printed sinter particles at 100% scale an AoR of 46.58° +/- 3.19° (at 95% confidence level). This matches a relative uncertainty of (3.19/46.58*100 =) 6.8%, which is higher than those acquired in the present study. As such, the measurements are reliable and suitable for comparing different levels of particle simplification. Besides, the angle of repose is reported to one decimal place, following the measurement precision used in the literature sources considered in this study [110–112].

Table 15: Mean, uncertainty (95% confidence level) and relative uncertainty of AoR at different simplification levels

	400000 faces	400 faces	100 faces	40 faces
Mean AoR	48.9°	41.7°	46.0°	44.4°
Uncertainty (95% confidence level)	+/- 2.1°	+/- 2.9°	+/- 2.5°	+/- 1.4°
Relative Uncertainty	+/- 4.3 %	+/- 6.2 %	+/- 5.3 %	+/- 3.1%

Effect of Shape Simplification on Angle of Repose:

Figure 38 and Table 15 show that the mean AoR slightly decreases as number of faces decrease, suggesting a marginal increase in flowability.

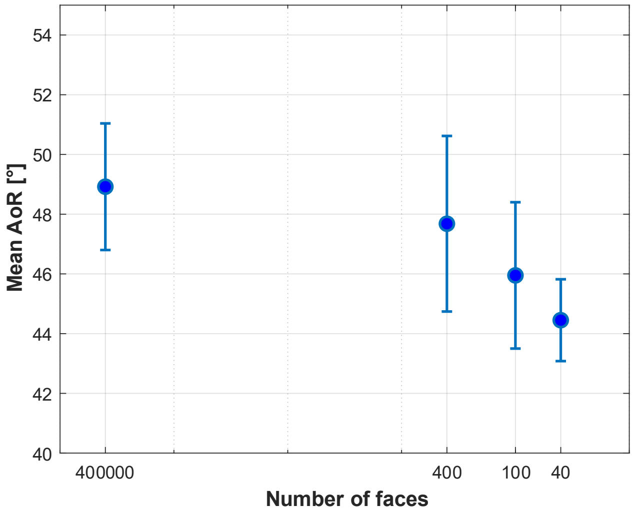

Figure 38: Mean and uncertainty (95% confidence level) of the AoR across the different levels of simplification

Even though the 95% confidence intervals for adjacent configurations overlap, this does not automatically mean the differences between them are not statistically insignificant. In fact, statistical theory shows that overlaps of up to about 29% can still correspond to a significant difference ($P < 0.05$) when comparing two independent averages [113]. Accordingly, overlaps are reviewed relative to the width of the reference configuration's 95% confidence interval, under the assumption that the confidence intervals are independent and symmetric.

As shown in Table J.2 the overlaps between adjacent simplification levels exceed the 29% threshold, ranging from 44.6% for 400 vs 400,000 faces to 67.5% for 100 vs 400 faces and 57.5% for 40 vs 100 faces. This indicates that the stepwise differences in angle of repose between adjacent face counts are unlikely to be statistically significant. Looking at the cumulative changes of the tested models, statistically significant changes in AoR w.r.t. the 400,000-face model is observed at the 40-face model, having an overlap of 0%. This indicates that the resolution where the AoR starts to change significantly, might be between 100 and 40-faces. However, the exact point of this transition cannot be precisely determined from the current data. The mean AoR decreased from 48.9° (400,000 faces) to 46.0° (100 faces), which falls within the 'Cohesive' category (Table 12). With the AoR further decreased to 44.4° (at 40 faces), reaching the upper limit of 'Fair Flowing'.

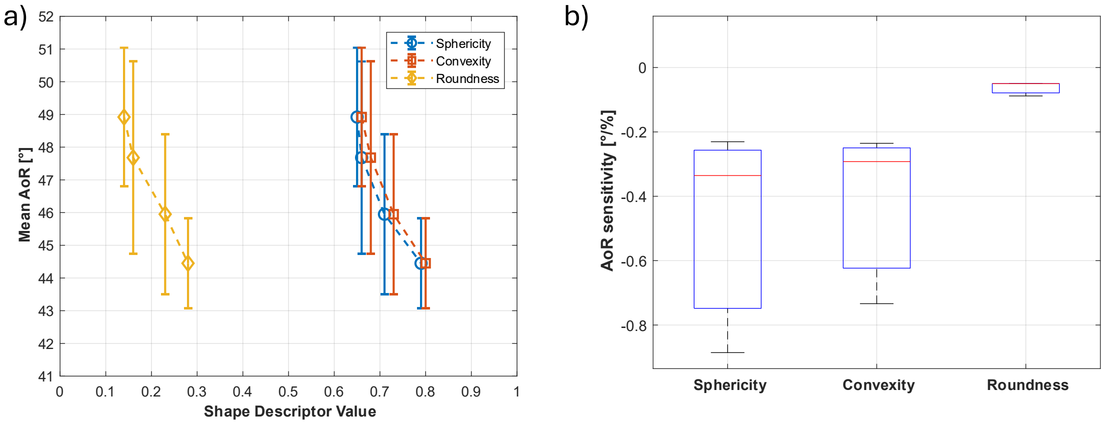

Figure 39: Relationship between AoR and Particle shape descriptors. a) mean AoR as a function of sphericity (blue), convexity (red), and roundness (yellow); the error bars here represent the uncertainties (95% confidence level). b) sensitivity of AoR to changes in each shape descriptor, the boxplots show the distribution across measurements with the median (red line), interquartile range (box) and whiskers indicating the max. and min. values

The observed reduction in angle of repose with decreasing face count can be directly connected to changes in particle geometry. Figure 39a shows that as sphericity, convexity, and roundness increase with decreasing face count, the mean AoR correspondingly decreases. This trend implies that particles with fewer faces, which are more spherical, convex, and rounded, exhibit lower resistance to flow initiation, consistent with classical granular mechanics where smoother, more regular shapes tend to pack more efficiently and reduce interparticle interlocking. Figure 39b illustrates boxplots that quantify the sensitivity of the angle of repose (AoR) to changes in particle shape descriptors: sphericity, convexity, and roundness. For each simplification, the difference from the reference AoR (400,000 faces) is divided by the percentage change in the shape descriptor (Equation 17):

$$\Delta AoR = \frac{AoR - AoR_{ref}}{d} \qquad (17)$$

where:

- AoR is the mean value at a given simplification level
- AoR_{ref} is the mean value for the reference configuration (400,000 face model)

- d is the percentage change of the corresponding shape descriptor (sphericity, convexity, or roundness) relative to its reference value (Table 5)

This defines a sensitivity metric that quantifies the change in AoR per unit relative change in shape, enabling a normalized comparison across descriptors with different numerical ranges. These resulting values are summarized using boxplots. The whiskers directly match the observed minimum and maximum sensitivities. The box height reflects the IQR (calculated as Equation J.3-J.5), forming a narrow box around the median, while the box width is purely graphical. For scientific comparison, this representation assumes that these interpolated sensitivity values give a meaningful summary of relative changes, even with a limited number of configurations. In larger datasets, median, quartiles, and whiskers would be computed directly from the data distribution, but here the approach is used to provide a consistent visualization of how AoR responds to variations in sphericity, convexity, and roundness.

Analysis of the sensitivity boxplots in Figure 39b shows that sphericity is the most sensitive shape descriptor, followed closely by convexity, with roundness being the least sensitive. The negative values of ΔAoR per percent change confirm an inverse relationship.

- Sphericity exhibits the largest magnitude of ΔAoR per percent change, with values ranging from approximately -0.88°/% (min) to -0.23°/% (max) and a median of −0.33°/%.
- Convexity shows slightly less sensitivity, with ΔAoR per percent change ranging from -0.73°/% to -0.23°/% and a median of −0.29°/%..
- Roundness has the smallest impact, with values between -0.08°/% and -0.04°/% and a median of −0.04°/%.

These results demonstrate that the cumulative decrease in AoR observed at very low face counts (below 100 faces) is primarily driven by increases in particle sphericity, closely followed by convexity, while roundness plays a secondary role. The quantified ranges and medians provide a clear, reproducible comparison of the relative influence of each shape descriptor on flow behaviour.

In short, the effect of particle shape simplification on AoR demonstrates that reducing face count leads to a slight but systematic decrease, indicating marginally improved flowability. While stepwise differences between adjacent face-count configurations are generally not statistically significant, cumulative reductions start to become more significant at very low face counts.

This decrease in AoR appears to be primarily driven by increases in particle sphericity and, to a slightly lesser extent, convexity, whereas roundness contributes minimally. Overall, these findings indicate that geometric simplification might have a minor effect on flowability, with the models mostly remaining within the same flowability category (‘cohesive’), and the simplest model reaching only the upper bound of the next lower category.

5.3.2 Coefficient of Static Friction (Single Particle)

The coefficient of static friction at the single-particle level was reviewed by applying two complementary experiments: a random placement test and a controlled placement test.

Measurement Accuracy and Validation

The reliability of the coefficient of static friction measurements is supported by the relative uncertainties observed in this study (Table 16-18), which vary from 3.83% to 11.81% across single-particle and bulk tests. For reference, [21] reported a wall friction angle of 27.6° ± 3.4° (95% confidence level) for 100% scale 3D-printed particles using the same inclined-plane method. Using Schuitemaker's values in the uncertainty formula provided in Appendix J yields a relative uncertainty of (0.07556/0.52* 100=) 14.53%, demonstrating that the measurement approach applied here is reliable and suitable for comparing different levels of particle simplification. Besides, the coefficient of static friction is reported to two decimal place, following the measurement precision used in the literature sources considered in this study [21,114].

Effect of shape simplficiation on coefficient of static friction (single particle level):

Random Placement Test

The mean coefficient of static friction decreases slightly as particle complexity is reduced from 0.48 (400,000 faces) to 0.46 (40 faces) (Table 16, Figure 40).

Table 16: Mean, uncertainty (95% confidence level) and relative uncertainty of the μ_s (single-particle level, random placement test) at different simplification levels

	400000 faces	400 faces	100 faces	40 faces
Mean μ_s	0.48	0.47	0.46	0.46
Uncertainty (95% confidence level)	+/- 0.06	+/- 0.04	+/- 0.03	+/- 0.03
Relative Uncertainty	12.50%	8.51%	6.52%	6.52%

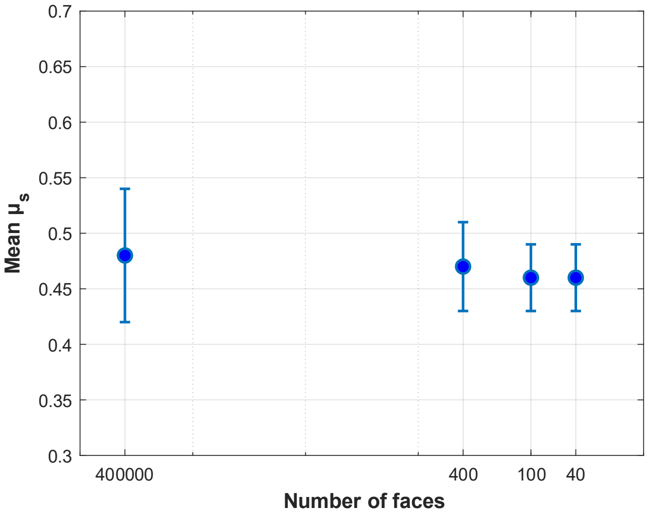

Figure 40: Mean and uncertainty (95% confidence level) of μ_s across levels of simplification (random placement test)

As shown in Table J.5, the confidence intervals for all adjacent simplification levels overlap by more than the 29% threshold. Furthermore, the cumulative change for the 100- face and 40-face models w.r.t. the 400,000-face model also exceeds this threshold. This indicates that the small decrease in the measured mean values is unlikely to be a statistically significant change.

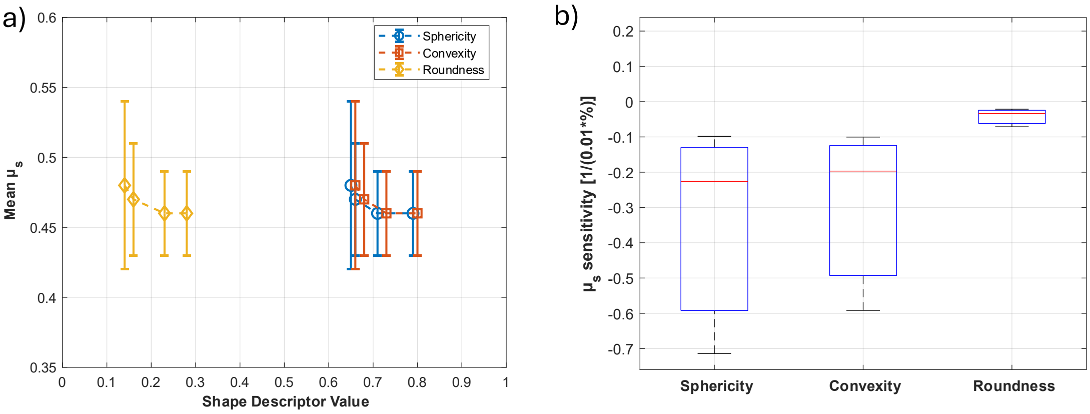

Figure 41: Relationship between μ_s (single particle, random) and Particle shape descriptors. a) mean μ_s as a function of sphericity (blue), convexity (red), and roundness (yellow); the error bars here represent the uncertainties (95% confidence level). b) sensitivity of μ_s to changes in each shape descriptor, the boxplots show the distribution across measurements with the median (red line), interquartile range (box) and whiskers indicating the max. and min. values

Figure 41a shows the measured mean coefficient of static friction plotted against sphericity, convexity, and roundness. Across all descriptors, a slight downward trend is observed as descriptor values increase, implying that geometric simplification (increasing sphericity, convexity, and roundness) is associated with a slight reduction in single-particle friction coefficient.

Nevertheless, this decrease is statistically insignificant, and no clear quantitative distinction between the effects of individual shape descriptors can be made. The trend suggests that smoother, more regular particle geometries may slightly reduce friction, though this effect remains weak relative to experimental uncertainty.

Figure 41b shows boxplots quantifying the sensitivity of the single-particle coefficient of static friction (random placement) to changes in particle shape descriptors. The changes in μ_s are is divided by the percentage change (0.01 increments) of each shape descriptor relative to the reference configuration (Equation 18):

$$\Delta\mu_s = \frac{\mu_s - \mu_{s_{ref}}}{0.01 * d} \tag{18}$$

, where:

- μ_s is the mean value at a given simplification level
- $\mu_{s_{ref}}$ is the mean value for the reference configuration (400,000 face model)
- d is the percentage change of the corresponding shape descriptor (sphericity, convexity, or roundness) relative to its reference value (Table 5)

Analysis of the sensitivity boxplots shows that μ_s exhibits a weak inverse sensitivity to shape descriptors: all sensitivities are negative, meaning that increases in sphericity, convexity, and roundness match reductions in μ_s:

- **Sphericity**: $\Delta\mu_s$ ranges from −0.71 to −0.10, with a median of −0.23
- **Convexity**: $\Delta\mu_s$ ranges from −0.59 to −0.10, with a median of −0.20
- **Roundness**: $\Delta\mu_s$ ranges from −0.07 to −0.02, with a median of −0.03

Overall, the slight reduction in μ_s with geometric simplification appears mainly linked to increases in sphericity, with smaller effects from convexity and minimal impact from roundness. Nevertheless, these effects remain statistically insignificant under random placement conditions.

Controlled Placement Test

In the results of the controlled placement test, the mean coefficients of static friction were slightly higher. Indicating that the chosen particle orientation and location on inclined surface tester may lead to a higher sliding resistance. Uncertainties decreased slightly, particularly for simpler particles, showing that controlling experimental variables enhances repeatability (Table 17, Figure 42).

Table 17: Mean, uncertainty (95% confidence level) and relative uncertainty of μ_s (single-particle level, controlled placement test) at different simplification levels

	400000 faces	400 faces	100 faces	40 faces
Mean coefficient of static friction	0.52	0.51	0.48	0.47
Uncertainty (95% confidence level)	+/- 0.04	+/- 0.04	+/- 0.02	+/- 0.02
Relative Uncertainty	+/- 7.69%	+/- 7.84%	+/- 4.17%	+/- 4.26%

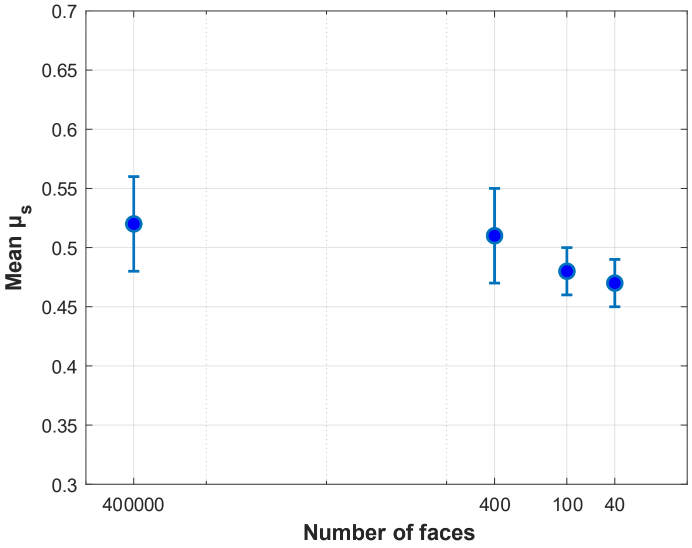

Figure 42: Mean and uncertainty (95% confidence level) of μ_s across various levels of simplification (controlled placement test)

For the single-particle controlled test, where experimental variability is minimized and shape is the only source of variation, overlaps between the confidence intervals of the adjacent face-count configurations are substantial Table J.8: 75.0% for 40 vs 100 faces, 37.5% for 100 vs 400 faces, and 87.5% for 400 vs 400,000 faces, all above the 29% threshold. Looking at the cumulative changes, the overlap values for the 100-face and 40-face model w.r.t. the 400,000-face model are below the threshold.

Considering cumulative changes across the full simplification range, overlaps decrease to 25.0% for 100 vs 400,000 faces and 12.5% for 40 vs 400,000 faces, both below the 29% significance threshold. These results indicate that while stepwise reductions in the measured mean single-particle friction coefficient are generally not statistically significant, the cumulative effect across simplifications below the 400 face resolution could potentially reach a statistically meaningful change in the coefficient of static friction relative to the original particle shape (400,000 faces).

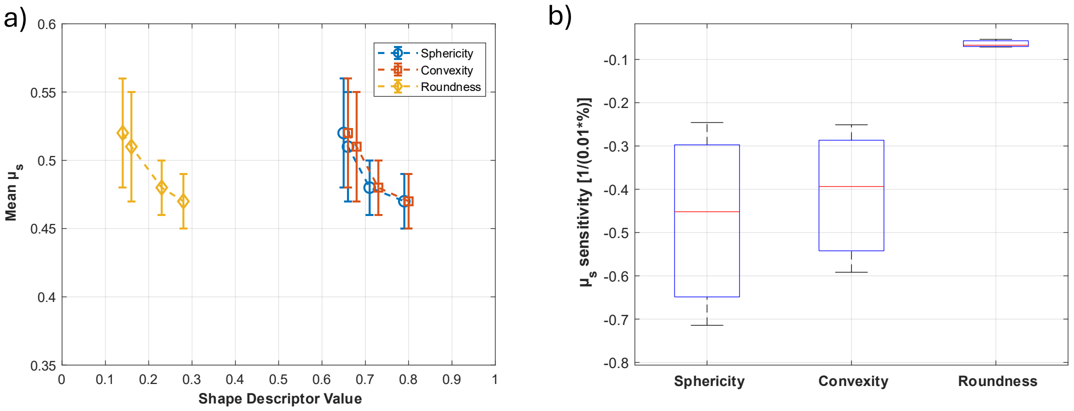

Figure 43: Relationship between μ_s (single particle level) and particle shape descriptors. a) mean μ_s of sphericity (blue), convexity (red), and roundness (yellow); the error bars here represent the uncertainties (95% confidence level). b) sensitivity of μ_s to changes in each shape descriptor, the boxplots show the distribution across measurements with the median (red line), interquartile range (box) and whiskers indicating the max. and min. values

Figure 43a illustrates the measured mean coefficient of static friction plotted against sphericity, convexity, and roundness. Across all descriptors, a slight downward trend is observed as descriptor values increase, implying that geometric simplification (increasing sphericity, convexity, and roundness) is associated with a modest reduction in single-particle friction. While changes between adjacent configurations are generally not statistically significant, the cumulative reduction relative to the original particle shape (400,000 faces) for resolutions below the 400-face model appears to be significant. This indicates that, under these controlled conditions, changes in particle shape descriptors might collectively have a measurable effect on the coefficient of static friction.

Figure 43b shows boxplots quantifying the sensitivity of the single-particle coefficient of static friction under controlled placement conditions, where shape was the only source of variability, to changes in particle shape descriptors. As in the random placement case, μ_s presents a negative sensitivity to all shape descriptors:

- Sphericity: $\Delta\mu_s$ ranges from −0.71 to −0.25, median −0.25
- Convexity: $\Delta\mu_s$ ranges from −0.59 to −0.25, median −0.39
- Roundness: $\Delta\mu_s$ ranges from −0.07 to −0.05, median −0.07

In the controlled test, where experimental variability is minimized and shape is the only source of variation, the slight reduction in μ_s with geometric simplification is mainly linked to increases in sphericity and convexity, with roundness playing a minor role. These cumulative effects could potentially become statistically meaningful below the 400-face resolution. In contrast, under random placement, where particle arrangement introduces additional variability, reductions in μ_s appear small and remain statistically insignificant.

5.3.3 Coefficient of static friction (Bulk-level)

Effect of shape simplification on coefficient of static friction (Bulk level):

Mean coefficients of static friction for bulk particle level also decrease slightly as particle mesh resolution is reduced, ranging from 0.55 (400,000 faces) to 0.49 (40 faces) (Table 18, Figure 44). Coefficient of static friction values are higher than at the single-particle level, which may be linked to the augmented normal forces generated by all the particles weights together, which increases resistance to sliding. The uncertainties are fewer than in single-particle tests, showing averaging effects over multiple particle contacts.

Table 18: Mean, uncertainty (95% confidence level) and relative uncertainty μ_s (bulk level) at different simplification levels

	400000 faces	400 faces	100 faces	40 faces
Mean μ_s	0.55	0.54	0.52	0.49
Uncertainty (95% confidence level)	+/- 0.03	+/- 0.03	+/- 0.03	+/- 0.03
Relative Uncertainty	+/- 5.45%	+/- 5.56%	+/- 5.77%	+/- 6.12%

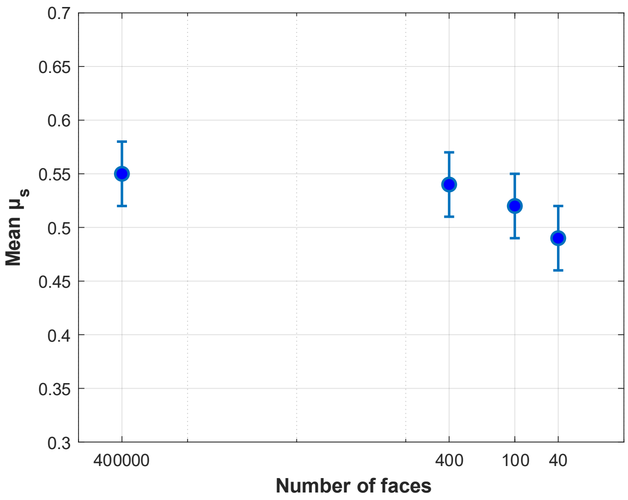

Figure 44: Mean and uncertainty (95% confidence level) of μ_s across levels of simplification (bulk level)

Here, the overlaps between confidence intervals of adjacent face counts all exceed the 29% threshold. The same is true for the cumulative changes, except for the overlap of the confidence interval of the 40-face model w.r.t. the interval of the 400,000- face model, having an overlap of 0% (Table J.11). The resolution where the threshold value starts to fall below is not precisely known, but likely between 100 and 40 face model.

These results indicate that while stepwise reductions in the measured coefficient of static friction (bulk level) are not statistically significant, the cumulative effect across simplifications below the 100-face resolution could potentially reach a statistically meaningful change in the coefficient of static friction relative to the original particle shape (400,000 faces).

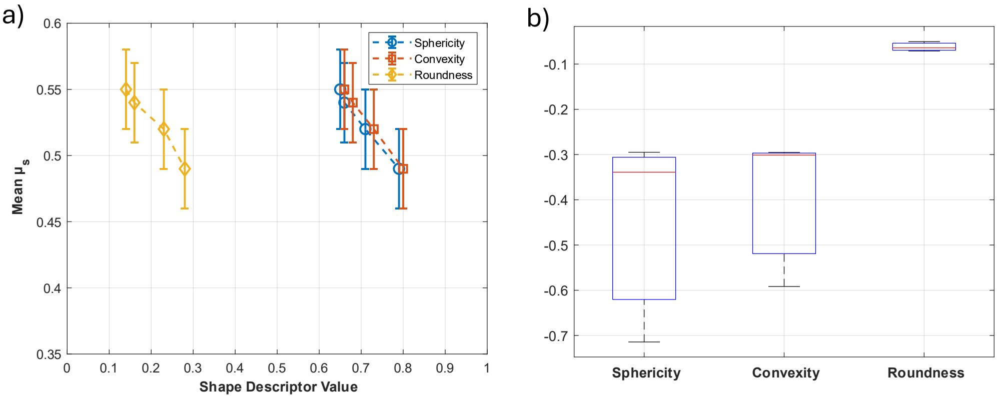

Figure 45: Relationship between μ_s (bulk level) and particle shape descriptors. a) mean μ_s as a function of sphericity (blue), convexity (red), and roundness (yellow); the error bars here represent the uncertainties (95% confidence level). b) sensitivity of μ_s to changes in each shape descriptor, the boxplots show the distribution across measurements with the median (red line), interquartile range (box) and whiskers indicating the max. and min. values

Figure 45a shows the measured mean coefficient of static friction plotted against sphericity, convexity, and roundness for bulk particle assemblies. Across all descriptors, a slight downward trend is observed as descriptor values increase, indicating that geometric simplification (increasing sphericity, convexity, and roundness) is associated with a modest reduction in bulk friction.

Figure 45b presents boxplots quantifying the sensitivity of the coefficient of static friction, under bulk conditions. As in the single particle case, μ_s exhibits negative sensitivity to all shape descriptors. The sensitivity is expressed in 0.01-unit increments per % change in the descriptor:

- **Sphericity:** $\Delta\mu_s$ ranges from −0.71 to −0.29, median −0.34
- **Convexity:** $\Delta\mu_s$ ranges from −0.59 to −0.30, median −0.30
- **Roundness:** $\Delta\mu_s$ ranges from −0.07 to −0.05, median −0.06

These results imply that, similar to the single-particle case, increase in the shape descriptors (mainly sphericity and convexity) are associated with modest decrease in μ_s. The resolution at which the decrease in μ_s may first become statistically significant is likely between the 100- and 40-face models.

5.3.4 Hausner Ratio

Measurement Accuray and Validation

As shown in Table 19, the relative uncertainties range from 2.07% to 2.27%. For comparison, a study by [107] reported a mean Hausner ratio of 1.25 with an absolute uncertainty of ±0.03. This corresponds to a relative uncertainty of 2.4%. As the relative uncertainties in this study are lower, the HR measurements are considered accurate. The Hausner Ratio is reported to two decimal places, following the measurement precision used in the literature sources considered in this study [107,115,116].

Table 19: Mean, uncertainty (95% confidence level) and relative uncertainty of HR at different simplification levels

	400000 faces	400 faces	100 faces	40 faces
Mean HR	1.45	1.42	1.36	1.32
Uncertainty (95%)	+/- 0.03	+/- 0.03	+/- 0.03	+/- 0.03
Relative Uncertainty	+/- 2.07%	+/- 2.11%	+/- 2.21%	+/- 2.27%

Results and Trends

Higher-face-count particles show larger HR values, indicating poorer flowability, while simpler shapes flow more easily. Based on standard HR classifications (Table 13), the 400,000-, 400-, and 100-face samples are categorized as poor, whereas the 40-face sample is at the upper limit of passable flowability.

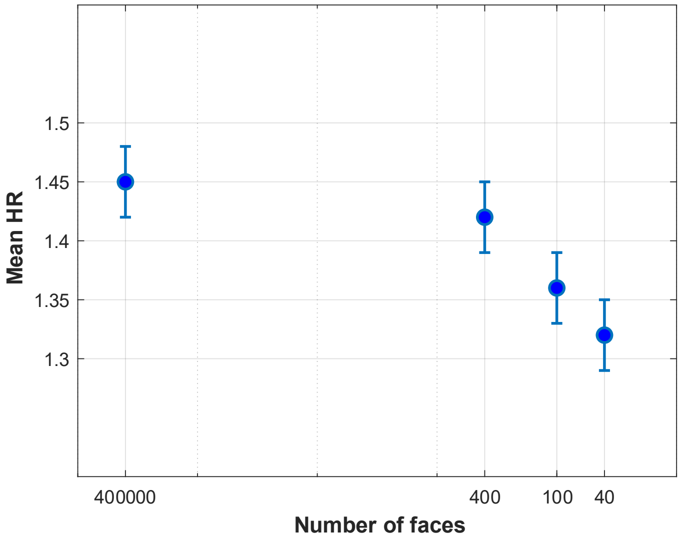

Figure 46: Mean and uncertainty (95% confidence level) of Hausner Ratio across various levels of simplification

Overlaps were assessed relative to the 95% confidence interval of the reference configuration, assuming independent and symmetric intervals.

The overlaps of the confidence intervals between adjacent resolutions generally exceed the threshold, except for the overlap between that of the 400- w.r.t. 100-

face model (Table J.18). Considering cumulative changes, overlaps decrease to 0.0% for both 100 vs 400,000 faces and 40 vs 400,000 faces, falling below the 29% threshold. The resolution at which the decrease may begin to approach statistical significance is likely to be between the 400-and 100-face models.

These results indicate that while stepwise reductions in mesh resolution generally may not yield statistically significant changes in the Hausner Ratio, cumulative simplifications below 400 faces can produce statistically significant reductions.

Nevertheless, the practical impact on flowability appears to be modest: most samples remain classified as having poor flow behaviour, while the 40-face sample falls at the upper end of the passable-flow range, near the boundary with poor flow (Table 13).

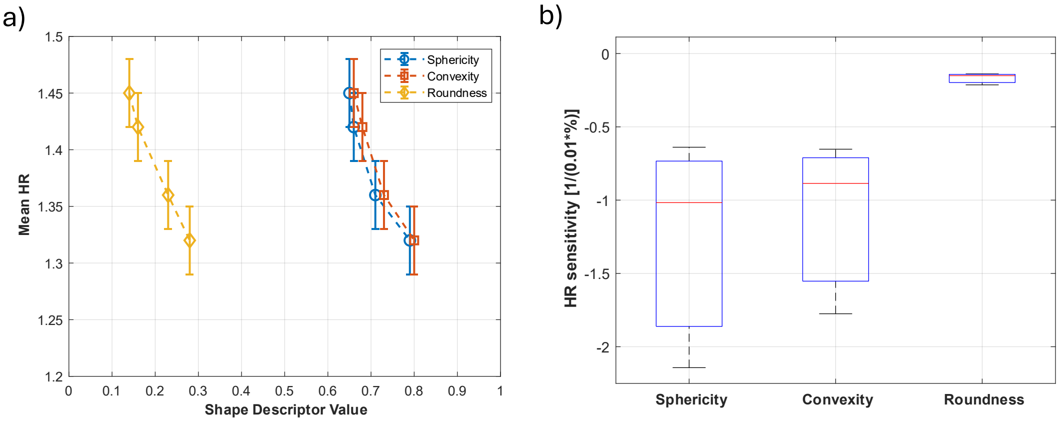

Figure 47: Relationship between HR and Particle shape descriptors. a) mean HR as a function of sphericity (blue), convexity (red), and roundness (yellow); the error bars here represent the uncertainties (95% confidence level). b) sensitivity of HR to changes in each shape descriptor, the boxplots show the distribution across measurements with the median (red line), interquartile range (box) and whiskers indicating the max. and min. values

Figure 47a shows the measured mean HR against sphericity, convexity and roundness. All the descriptors show an inverse relationship with the mean HR values.

Figure 47b shows boxplots quantifying the sensitivity of the Hausner Ratio (HR) to changes in particle shape descriptors. Changes in HR are normalized relative to the reference configuration (Equation 19):

$$\Delta HR = \frac{HR - HR_{ref}}{0.01 * d} \tag{19}$$

where:

- HR is the mean value at a given simplification level
- HR_{ref} is the mean value for the reference configuration (400,000 face model)

- d is the percentage change of the corresponding shape descriptor (sphericity, convexity, or roundness) relative to its reference value (Table 5)

Analysis of the sensitivity boxplots shows that HR exhibits negative sensitivity to all shape descriptors, indicating that increases in sphericity, convexity, and roundness correspond to reductions in HR:

- **Sphericity:** ΔHR ranges from −2.14 to −0.64, median −1.02
- **Convexity:** ΔHR ranges from −1.78 to −0.65, median −0.89
- **Roundness:** ΔHR ranges from −0.21 to −0.14, median −0.15

These results imply that the modest reduction in HR with geometric simplification is primarily associated with increases in sphericity and convexity, while roundness has a smaller effect. Cumulative shape simplifications appear to be statistically meaningful relative to the original 400,000-face particle, likely below 400-face resolution.
Nonetheless, the influence on flowability appears modest: most samples remain in the poor-flow category, while the 40-face particle falls at the upper end of the passable-flow range, close to the boundary with poor flow.

5.4 Conclusion

In this chapter, the following sub-research is carefully examined and answered: "How does the level of simplification influence measurable bulk properties such as angle of repose, coefficient of static friction, and Hausner ratio?"
The results imply that particle simplification a small but consistent effect on bulk flow properties:

- **Angle of Repose (AoR)**: decreases slightly from 48.9° (400,000 faces) to 44.4° (40 faces), likely due to increased sphericity and convexity, with roundness contributing minimally. Stepwise decreases between adjacent AoR are generally not statistically significant, and cumulative reductions may start to become notable below 100 faces, with 40 faces representing a resolution where the cumulative change in AoR appears to be statistically significant. Overall, flowability remains within the same category ('Cohesive' to upper limit of 'Fair Flowing' solely for the 40-face model), indicating that the practical impact of geometric simplification is likely limited.
- **Coefficient of Static Friction (μ_s):** Particle simplification leads to slight decreases in the coefficient of static friction at both single-particle and bulk levels.
  - Single-particle level: In the random placement test, μ_s decreases modestly from 0.48 (400,000 faces) to 0.46 (40 faces). Stepwise decreases between adjacent μ_s are unlikely to be statistically significant, and the same appears for the cumulative reductions. Controlled placement tests show

slightly higher μ_s values (0.52–0.47) and reduced uncertainties, confirming that orientation can enhance friction and that shape changes may collectively have a measurable effect under controlled conditions. For the controlled placement case, the same trend goes for the stepwise differences between adjacent μ_s to be unlikely statistical significant. However, the cumulative decrease in μ_s appears to start at a resolution below 400 faces. Sensitivity analysis indicate that the main cause for the decrease in μ_s , is due to the increase in sphericity and convexity. The increase in roundness appears to have the minimal contribution. Overall, these results indicate that the cumulative simplifications (likely due to increase in sphericity and convexity) may have an effect at a single particle level, once the shape effects are isolated.
- Bulk level: Mean μ_s decreases from 0.55 (400,000 faces) to 0.49 (40 faces). Stepwise decreases are generally not significant, but cumulative reductions below 100 faces may be statistically meaningful. Sensitivity analysis shows the same trend for the single particle case, with shape having the highest sensitivity to sphericity and convexity, while being least sensitive to roundness changes. Overall, at the bulk level, the values of μ_s appear to slightly decrease at resolutions below the 100-face model, with the increase in sphericity and convexity having the largest contribution and roundness the least.

- **Hausner Ratio (HR):** gradually decreases from 1.45 (400,000 faces) to 1.32 (40 faces) as particle complexity is reduced, likely due to the increase in sphericity and convexity, with roundness contributing minimally.
  Stepwise decreases between adjacent HR are generally not statistically significant, but cumulative decreases appear to start at a mesh resolution below 400 faces.
  Despite these cumulative changes, most models remain in the “poor” flowability category, while the 40-face sample falls near the upper end of the passable-flow range, close to the boundary with poor flow, suggesting only a modest practical change.

In short, geometric simplification appears to have a small but consistent influence on bulk flow properties. Slight reductions in angle of repose, coefficient of static friction, and Hausner ratio are associated with increases in sphericity and convexity, while roundness has minimal effect. Stepwise changes between adjacent face counts are generally not statistically significant, and cumulative effects tend to appear at resolutions below 100 faces for AoR and μ_s, and below 400 faces for HR.
Overall, bulk flow behaviour appears largely similar. Based on angle of repose, flowability might be classified from ‘Cohesive’ to the upper limit of ‘Fair Flowing’ solely for the 40-face model, while classifications based on Hausner Ratio place most samples in the poor-flow category, with the 40-face sample appearing near the upper end of the passable-flow range, close to the boundary with poor flow. These observations indicate only a modest practical change in flowability with geometric simplification.

6 Conclusion

The aim of this master thesis consists of reviewing the way in which particle shape simplification affects the flowability of 3D-printed sinter particles. This section wraps up the key findings from the sub-research questions and concludes by addressing the main research question.

1) **Which shape modelling method and shape descriptors most accurately capture and quantify the geometry of irregularly shaped particles?**

   The comparison of three modelling approaches multi-sphere, polyhedral, and super-ellipsoid showed that the polyhedral model most precisely captures irregular particle geometries, such as angularity, flat faces, and sharp edges. It provides superior geometric fidelity, crucial for regenerating irregularly shaped particle morphology in 3D printing. Among various descriptors, sphericity, convexity, and roundness proved to be the most effective parameters for quantitatively reviewing deviations in particle shape morphology between the original and simplified shapes. This combined framework based on the polyhedral modelling approach in combination with the descriptors sphericity, convexity, and roundness gives the most effective means of representing simplified particle geometries and quantifying their deviations from original shapes. In this study, this framework is applied to a single representative particle, as the entire printed bulk consists of particles with identical shape and size. Future studies could extend this approach to bulk systems consisting of particles with varying shapes and sizes.

2) **How does the level of geometric simplification impact the shape descriptors and volume relative to the original particle?**

   Geometric simplification was found to non-linearly increase the shape descriptors and decrease the volume once the mesh resolution decreased below a certain threshold resolution. Over the tested range these shape descriptors changed: sphericity increased from 0.65 to 0.79 (remaining within the same ‘spherical/equant’ classification but with the highest value approaching the ‘high sphericity category’), convexity increased from 0.66 to 0.80, and roundness increased from 0.14 to 0.28 (changing its classification from ‘very angular’ to ‘sub-angular’).
   In this study, the threshold resolution was determined where it was assumed that a 5% (or less) relative change in the average absolute deviation of the shape descriptors (sphericity, convexity, and roundness) represents a negligible shape change. In calculating the overall relative deviation (%), sphericity, convexity, and roundness were treated as equally important, since no data was available to indicate differing weights. This

unweighted mean provides a simple, reproducible, and standardized measure of overall deviation that treats all shape descriptors equally. As a result, the threshold in this study was defined to be around 400 faces. Volume stayed nearly constant (±0.16%) above 400 faces but diminished by up to 19% at 40 faces. Therefore, as mesh resolution decreased, the shape became more spherical, convex, and smoother, and the volume decreases, with the 400-face model defined as the threshold where the non-linear change starts.

In future studies, the threshold resolution could be determined more precisely by leveraging the sensitivity analysis of ΔAoR, $\Delta\mu_s$, and ΔHR with respect to the shape descriptors, as presented in Chapter 5.

3) **How to 3D print simplified shaped particles in bulk with matched volume and weight to the original particle?**

A standardized 3D-printing methodology was made to fabricate simplified particle replicas while keeping volume and mass equivalence with the original particles, guaranteeing particle shape remained the only experimental variable. Three representative resolutions, 40, 100, and 400 faces, were chosen given quantitative shape descriptors, capturing the full range from extreme simplification (40 faces), to intermediate fidelity (100 faces) and the threshold resolution (400 faces). Homothetic scaling preserved volume, while empirically calibrated infill ratios acquired mass deviations within the 95% confidence interval of 3.69 g. Bulk production of 1000 particles per type employing standardized FDM parameters (0.4 mm nozzle, 0.2 mm layer height) exhibited reproducible dimensional accuracy and consistent density. Material budgeting assured that sufficient filament was available for bulk production. The main limitation of this bulk printing process was the limited build volumes of the available printers. This resulted in multiple printer cycles, increasing printing time.

Nevertheless, the methodology made reliable and reproducible production of particles possible, supporting controlled experiments on shape-dependent flow behaviour. In future studies, industrial-scale printers, which have larger build volumes, could be used to produce greater quantities of particles per run, reducing the number of printing cycles and allowing experiments with larger bulk samples.

4) **How does the level of simplification influence measurable bulk properties such as angle of repose, coefficient of static friction, and Hausner ratio?**

Particle simplification appears to have a small but consistent effect, slightly increasing flowability, as the mesh resolution decreases. The mean angle of repose decreases slightly from 48.9° for the original high-resolution model (400,000 faces) to 44.4° for the most simplified model (40 faces). The decrease in AoR with respect to the reference value (48.9°)appears to become significant for mesh resolutions below 100 faces. This decrease

might be primarily due to increases in sphericity and convexity, while changes in roundness contribute minimally.
Single-particle coefficients of static friction (μ_s) was measured under two conditions: random placement and controlled placement, with the controlled placement test isolating shape effects. Under random placement, the mean μ_s decreased slightly from 0.48 to 0.46, with no significant difference. In controlled placement, it decreased from 0.52 to 0.47, becoming potentially significant below 400 faces. This decrease in μ_s at single particle level is appears due to primarily the increase in sphericity and convexity, with roundness increase contributing minimally, when shape effects are isolated at the single particle level.
Bulk-level coefficients of static friction (μ_s) also show a modest decrease from 0.55 to 0.49. Here, the decrease in μ_s with respect to the reference value (0.55) may start at resolutions with less than 100 faces. The same for the single particle case, also here these cumulative decreases might be primarly due to the increase in sphericity and convexity, while roundness increases contributing minimally.
Similarly, the mean Hausner ratio decreases gradually from 1.45 to 1.32, where cumulative decreases with respect to the reference value (1.45) appear to start at mesh resolutions below 400 faces. Also for HR, these decreases may be mainly due to sphericity and convexity increases, and less likely due to roundness increases.
Despite these trends, overall flowability classifications remain largely unchanged. Based on the angle of repose, all samples are classified as ‘Cohesive’ except the 40-face model, which approaches the upper limit of the ‘Fair Flowing’ category. Based on the Hausner ratio, most models remain within the “poor” flowability category, with the 40-face model near the upper end of the passable-flow range. Future studies could examine additional intermediate face counts below 100 to better identify the resolution at which cumulative shape changes lead to statistically significant alterations in bulk flow properties.

Upon answering to all these sub-research questions, the main research question can be answered which is:

How does the shape simplification of 3D-printed sinter particle affect their flowability?

Synthesizing the findings from the sub-research questions, polyhedral shape simplification of 3D-printed sinter particles appears to have a small but consistent influence on bulk flowability. As mesh resolution decreases below approximately 400 faces, sphericity and convexity increase noticeably. Based on the sensitivity analysis of AoR, μ_s, and HR with respect to relative changes in the shape descriptors, increases in sphericity and convexity appear to be the primary factors driving their decrease, whereas the effect of increased roundness is likely minimal.

These changes drive modest reductions in angle of repose, single-particle and bulk coefficients of static friction, and Hausner ratio. Stepwise changes between adjacent simplification levels are generally not statistically significant, with cumulative effects becoming measurable primarily at resolutions below ~100 faces for AoR and μ_s, and below ~400 faces for Hausner ratio. Consequently, simplified particles become slightly smoother and less angular, producing a minor increase in flowability. Despite these effects, flowability classifications remain largely unchanged: based on angle of repose, most samples are classified as ‘Cohesive’, with the 40-face model approaching the upper limit of the ‘Fair Flowing’ category, while Hausner ratio classifications remain mostly in the “poor” flowability range, with the 40-face sample near the passable-flow boundary. Overall, bulk flow behaviour is relatively robust, indicating that even substantial geometric simplification (40 faces) using the polyhedral approach does not fundamentally alter the flow characteristics of sinter particles.

7 Recommendations

Given the findings of this study, several avenues for future research are advised to further develop the understanding of particle shape simplification and its influence on flowability:

1. Explore a Range of Particle Shapes and Sizes
This study was concentrated on a single representative sinter particle with constant size. Future research could build on this scope by encompassing multiple particle shapes and also by including a particle size distribution. Examining a diverse set of morphologies and sizes would allow for assessment of whether the observed robustness of bulk flow behaviour under polyhedral shape simplification extends to more realistic granular systems. Such studies could offer a profounder understanding of the combined effects of shape heterogeneity and size variation on interparticle interactions and overall flowability.

2. Explore Alternative Shape Simplification Methods
While polyhedral simplification was effective for retaining essential particle morphology, alternative modelling approaches, for example super-ellipsoids, multi-sphere representations, or hybrid methods, could be explored. These approaches may provide insights into whether bulk flow behaviour is similarly preserved for particles with highly concave or irregular surfaces, and could aid at identifying the restrictions and advantages of different simplification strategies in representing complex geometries.

3. Investigate Extreme Shape Simplifications
This study took three simplification levels (40, 100, and 400 faces) into account, with the 40-face model showcasing the most extreme simplification tested. Future research could explore even lower-resolution geometries to identify the threshold at which particle shape simplification starts to significantly alter bulk flow behaviour. Examining these extreme cases would offer a clearer understanding of the limits of polyhedral simplification, uncover potential nonlinear effects on flow properties, and help setting up guidelines for the minimum geometric fidelity needed to protect representative flow characteristics in 3D-printed sinter particles.

4. Calibrate DEM Models for Polyhedral Shapes Using Flowability Metrics
Future work could include systematic calibration of DEM models for polyhedral particle shapes, specifically using measurable flowability parameters such as angle of repose, static friction coefficients (μ_s) at particle and bulk levels, and Hausner ratio. By adjusting contact parameters to match these macroscopic flow metrics, it would be possible to use simplified particle geometries, reducing computational load, while still accurately reproducing bulk flow behaviour. This approach would allow efficient simulations of large particle systems without requiring precise geometric details.

Bibliography

[1] Q. Sun, G. Wang, K. Hu, Some open problems in granular matter mechanics, Progress in Natural Science 19 (2009). https://doi.org/10.1016/j.pnsc.2008.06.023.

[2] H.M. Beakawi Al-Hashemi, O.S. Baghabra Al-Amoudi, A review on the angle of repose of granular materials, Powder Technol. 330 (2018). https://doi.org/10.1016/j.powtec.2018.02.003.

[3] H. Feng, Z.-Y. Yin, W. Liang, A novel unified elastoplasticity-μ (I) phase transition model for granular flows from solid-like to fluid-like states and its application, Eng. Geol. 352 (2025) 108054. https://doi.org/10.1016/j.enggeo.2025.108054.

[4] R.P. Behringer, B. Chakraborty, The physics of jamming for granular materials: A review, Reports on Progress in Physics 82 (2019). https://doi.org/10.1088/1361-6633/aadc3c.

[5] L. Lu, O. Ishiyama, 14 - Iron ore sintering, in: L. Lu (Ed.), Iron Ore, Woodhead Publishing, 2015: pp. 395–433. https://doi.org/https://doi.org/10.1016/B978-1-78242-156-6.00014-9.

[6] S. Cheng, P.C. Hayes, E. Jak, Iron Ore Sinter Macro-and Micro-Structures, and Their Relationships to Breakage Characteristics, Minerals 12 (2022). https://doi.org/10.3390/min12050631.

[7] R. Roeplal, Y. Pang, A. Adema, J. van der Stel, D. Schott, Modelling of phenomena affecting blast furnace burden permeability using the Discrete Element Method (DEM) – A review, Powder Technol. 415 (2023). https://doi.org/10.1016/j.powtec.2022.118161.

[8] C.K. Ho, S.M. Wu, H.P. Zhu, A.B. Yu, S.T. Tsai, Experimental and numerical investigations of gouge formation related to blast furnace burden distribution, Miner. Eng. 22 (2009). https://doi.org/10.1016/j.mineng.2009.03.004.

[9] B.D. Pandey, U.S. Yadav, Blast furnace performance as influenced by burden distribution, Ironmaking and Steelmaking 26 (1999). https://doi.org/10.1179/030192399677059.

[10] B.K. Mishra, R.K. Rajamani, The discrete element method for the simulation of ball mills, Appl. Math. Model. 16 (1992). https://doi.org/10.1016/0307-904X(92)90035-2.

[11] A.B. Yu, Discrete element method: An effective way for particle scale research of particulate matter, in: Engineering Computations (Swansea, Wales), 2004. https://doi.org/10.1108/02644400410519749.

[12] P.A. Cundall, O.D.L. Strack, A discrete numerical model for granular assemblies, Geotechnique 29 (1979). https://doi.org/10.1680/geot.1979.29.1.47.

[13] C. Coetzee, Calibration of the discrete element method: Strategies for spherical and non-spherical particles, Powder Technol. 364 (2020). https://doi.org/10.1016/j.powtec.2020.01.076.

[14] C.J. Coetzee, Calibration of the discrete element method and the effect of particle shape, Powder Technol. 297 (2016). https://doi.org/10.1016/j.powtec.2016.04.003.

[15] D. Höhner, S. Wirtz, V. Scherer, Experimental and numerical investigation on the influence of particle shape and shape approximation on hopper discharge using the discrete element method, Powder Technol. 235 (2013). https://doi.org/10.1016/j.powtec.2012.11.004.

[16] D. Markauskas, R. Kačianauskas, A. Džiugys, R. Navakas, Investigation of adequacy of multi-sphere approximation of elliptical particles for DEM simulations, Granul. Matter 12 (2010). https://doi.org/10.1007/s10035-009-0158-y.

[17] P.W. Cleary, DEM prediction of industrial and geophysical particle flows, Particuology 8 (2010). https://doi.org/10.1016/j.partic.2009.05.006.

[18] P.W. Cleary, M.L. Sawley, DEM modelling of industrial granular flows: 3D case studies and the effect of particle shape on hopper discharge, Appl. Math. Model. 26 (2002). https://doi.org/10.1016/S0307-904X(01)00050-6.

[19] J. Diviš, D. Žurovec, Á. Ramírez-Gómez, J. Hlosta, J. Rozbroj, K. Pokorná, J. Nečas, J. Zegzulka, DEM calibration insights on the role of particle shape for sub 2 mm particles, Sci. Rep. 15 (2025) 20477. https://doi.org/10.1038/s41598-025-04592-2.

[20] B. and L.S.J. and S.B. Su Yu-Feng and Zhang, Parametric Sensitivity Study of Particle Shape Effect Through 3D Printing, in: Y. and M.G. Li Xikui and Feng (Ed.), Proceedings of the 7th International Conference on Discrete Element Methods, Springer Singapore, Singapore, 2017: pp. 593–600.

[21] W.D. Schuitemaker, Design of grabs for coarse materials: Full-scale modelling of coarse cohesionless materials handling, Delft University of Technology, Faculty of Mechanical Engineering, 2025. https://resolver.tudelft.nl/uuid:2874d8ac-f8bc-4201-9dcc-f1bfc321921b.

[22] H. Ma, X. Xia, L. Zhou, C. Xu, Z. Liu, T. Song, G. Zou, Y. Liu, Z. Huang, X. Liao, Y. Zhao, A Comparative Study of the Performance of Different Particle Models in Simulating Particle Charging and Burden Distribution in a Blast Furnace within the DEM Framework, Energies (Basel). 16 (2023). https://doi.org/10.3390/en16093890.

[23] H. Ma, L. Zhou, Z. Liu, M. Chen, X. Xia, Y. Zhao, A review of recent development for the CFD-DEM investigations of non-spherical particles, Powder Technol. 412 (2022). https://doi.org/10.1016/j.powtec.2022.117972.

[24] Y. You, Y. Zhao, Discrete element modelling of ellipsoidal particles using super-ellipsoids and multi-spheres: A comparative study, Powder Technol. 331 (2018). https://doi.org/10.1016/j.powtec.2018.03.017.

[25] H. Kruggel-Emden, S. Rickelt, S. Wirtz, V. Scherer, A study on the validity of the multi-sphere Discrete Element Method, Powder Technol. 188 (2008). https://doi.org/10.1016/j.powtec.2008.04.037.

[26] B. Soltanbeigi, A. Podlozhnyuk, C. Kloss, S. Pirker, J.Y. Ooi, S.A. Papanicolopulos, Influence of various DEM shape representation methods on packing and shearing of granular assemblies, Granul. Matter 23 (2021). https://doi.org/10.1007/s10035-020-01078-y.

[27] D. Höhner, S. Wirtz, H. Kruggel-Emden, V. Scherer, Comparison of the multi-sphere and polyhedral approach to simulate non-spherical particles within the discrete element method: Influence on temporal force evolution for multiple contacts, Powder Technol. 208 (2011). https://doi.org/10.1016/j.powtec.2011.01.003.

[28] R.P. Jensen, P.J. Bosscher, M.E. Plesha, T.B. Edil, DEM simulation of granular media-structure interface: Effects of surface roughness and particle shape, Int. J. Numer. Anal. Methods Geomech. 23 (1999). https://doi.org/10.1002/(SICI)1096-9853(199905)23:6<531::AID-NAG980>3.0.CO;2-V.

[29] M.H. Abbaspour-Fard, Theoretical validation of a multi-sphere, discrete element model suitable for biomaterials handling simulation, Biosyst. Eng. 88 (2004). https://doi.org/10.1016/j.biosystemseng.2004.03.010.

[30] J.F. Favier, M.H. Abbaspour-Fard, M. Kremmer, A.O. Raji, Shape representation of axi-symmetrical, non-spherical particles in discrete element simulation using multi-element model particles, Engineering Computations (Swansea, Wales) 16 (1999). https://doi.org/10.1108/02644409910271894.

[31] F.L. Yuan, M. Sommerfeld, P. Muramulla, S. Gopireddy, L. Pasternak, N. Urbanetz, T. Profitlich, Rigid3D: a hybrid multi-sphere DEM framework for simulation of non-spherical particles in multi-phase flow, ArXiv Preprint ArXiv:2306.13678 (2023).

[32] A.G. Neto, P. Wriggers, Discrete element model for general polyhedra, Comput. Part. Mech. 9 (2022). https://doi.org/10.1007/s40571-021-00415-z.

[33] T.A. Shoemaker, C. Tanissa, Y.M.A. Hashash, Comparison of DEM Software with Polyhedral Particle Shapes, in: 2024. https://doi.org/10.1061/9780784485347.012.

[34] E. Illana, K. Qyteti, M. Scharnowski, M. Brömmer, S. Wirtz, V. Scherer, Shape-changing particles for locally resolved particle geometry in DEM simulations, Particuology 89 (2024). https://doi.org/10.1016/j.partic.2023.11.003.

[35] S. Zhang, A.M. Zsáki, Effect Geometric Detail on the Outcome of DEM Simulations with Polyhedral Particles, Geomechanics and Geoengineering 18 (2023). https://doi.org/10.1080/17486025.2022.2065037.

[36] J. Wedel, M. Štrakl, M. Hriberšek, P. Steinmann, J. Ravnik, A novel particle–particle and particle–wall collision model for superellipsoidal particles, Comput. Part. Mech. 11 (2024). https://doi.org/10.1007/s40571-023-00618-6.

[37] S. Zhao, T.M. Evans, X. Zhou, Shear-induced anisotropy of granular materials with rolling resistance and particle shape effects, Int. J. Solids Struct. 150 (2018). https://doi.org/10.1016/j.ijsolstr.2018.06.024.

[38] S. Wang, S. Ji, Smoothed Polyhedral DEM Model Based on Minkowski Sum Algorithm, in: Springer Tracts in Mechanical Engineering, 2024. https://doi.org/10.1007/978-981-99-9927-9_4.

[39] C. Xie, T. Song, Y. Zhao, Discrete element modeling and simulation of non-spherical particles using polyhedrons and super-ellipsoids, Powder Technol. 368 (2020). https://doi.org/10.1016/j.powtec.2020.05.008.

[40] C. Xie, H. Ma, Y. Zhao, Investigation of modeling non-spherical particles by using spherical discrete element model with rolling friction, Eng. Anal. Bound. Elem. 105 (2019). https://doi.org/10.1016/j.enganabound.2019.04.013.

[41] X. Wang, K. Tian, D. Su, J. Zhao, Superellipsoid-based study on reproducing 3D particle geometry from 2D projections, Comput. Geotech. 114 (2019). https://doi.org/10.1016/j.compgeo.2019.103131.

[42] P.J. BARRETT, The shape of rock particles, a critical review, Sedimentology 27 (1980). https://doi.org/10.1111/j.1365-3091.1980.tb01179.x.

[43] V. Angelidakis, S. Nadimi, S. Utili, SHape Analyser for Particle Engineering (SHAPE): Seamless characterisation and simplification of particle morphology from imaging data, Comput. Phys. Commun. 265 (2021). https://doi.org/10.1016/j.cpc.2021.107983.

[44] M.A. Maroof, A. Mahboubi, A. Noorzad, Y. Safi, A new approach to particle shape classification of granular materials, Transportation Geotechnics 22 (2020). https://doi.org/10.1016/j.trgeo.2019.100296.

[45] M. C. Powers, A New Roundness Scale for Sedimentary Particles, SEPM Journal of Sedimentary Research Vol. 23 (1953). https://doi.org/10.1306/d4269567-2b26-11d7-8648000102c1865d.

[46] S. Nadimi, J. Fonseca, Single-Grain Virtualization for Contact Behavior Analysis on Sand, Journal of Geotechnical and Geoenvironmental Engineering 143 (2017). https://doi.org/10.1061/(asce)gt.1943-5606.0001740.

[47] J. Fonseca, C. O'Sullivan, M.R. Coop, P.D. Lee, Non-invasive characterization of particle morphology of natural sands, Soils and Foundations 52 (2012). https://doi.org/10.1016/j.sandf.2012.07.011.

[48] J.M. Rodriguez, T. Edeskär, S. Knutsson, Particle shape quantities and measurement techniques-A review, Electronic Journal of Geotechnical Engineering 18 A (2013).

[49] S.J. Blott, K. Pye, Particle shape: A review and new methods of characterization and classification, Sedimentology 55 (2008). https://doi.org/10.1111/j.1365-3091.2007.00892.x.

[50] W.C. Krumbein, MEASUREMENT AND GEOLOGICAL SIGNIFICANCE OF SHAPE AND ROUNDNESS OF SEDIMENTARY PARTICLES, Journal of Sedimentary Research 11 (1941). https://doi.org/10.1306/D42690F3-2B26-11D7-8648000102C1865D.

[51] M. Potticary, A numerical investigation of the effect of particle shape on the strength of coarse granular materials, University of Southampton, 2018.

[52] C.R.I. Clayton, C.O.R. Abbireddy, R. Schiebel, A method of estimating the form of coarse particulates, Geotechnique 59 (2009). https://doi.org/10.1680/geot.2007.00195.

[53] C.K. Wentworth, The shapes of beach pebbles, USGS Professional Paper 131–C (1922).

[54] A. Cailleux, Distinction des galets marins et fluviatiles, Bulletin de La Société Géologique de France S5-XV (1945). https://doi.org/10.2113/gssgfbull.s5-xv.7-8.375.

[55] T. Zingg, Beitrag zur schotteranalyse, ETH Zurich, 1935.

[56] K. Bagi, Á. Orosz, A new variable for characterising irregular element geometries in experiments and DEM simulations, in: Proceedings - European Council for Modelling and Simulation, ECMS, 2020. https://doi.org/10.7148/2020-0256.

[57] M. Potticary, A. Zervos, J. Harkness, An investigation into the effect of particle platyness on the strength of granular materials using the discrete element method, in: Proceedings of the 4th International Conference on Particle-Based Methods - Fundamentals and Applications, PARTICLES 2015, 2015.

[58] D. Kong, J. Fonseca, Quantification of the morphology of shelly carbonate sands using 3D images, Geotechnique 68 (2018). https://doi.org/10.1680/jgeot.16.P.278.

[59] V. Angelidakis, S. Nadimi, S. Utili, Elongation, flatness and compactness indices to characterise particle form, Powder Technol. 396 (2022). https://doi.org/10.1016/j.powtec.2021.11.027.

[60] B. Zhao, J. Wang, 3D quantitative shape analysis on form, roundness, and compactness with µCT, Powder Technol. 291 (2016). https://doi.org/10.1016/j.powtec.2015.12.029.

[61] J. Žunić, P.L. Rosin, Measuring Shapes with Desired Convex Polygons, IEEE Trans. Pattern Anal. Mach. Intell. 42 (2020). https://doi.org/10.1109/TPAMI.2019.2898830.

[62] C.F. Mora, A.K.H. Kwan, Sphericity, shape factor, and convexity measurement of coarse aggregate for concrete using digital image processing, Cem. Concr. Res. 30 (2000). https://doi.org/10.1016/S0008-8846(99)00259-8.

[63] R.D. Beemer, L. Li, A. Leonti, J. Shaw, J. Fonseca, I. Valova, M. Iskander, C.H. Pilskaln, Comparison of 2D Optical Imaging and 3D Microtomography Shape Measurements of a Coastal Bioclastic Calcareous Sand, J. Imaging 8 (2022). https://doi.org/10.3390/jimaging8030072.

[64] B. Zhou, X. Zhang, J. Wang, H. Wang, J. Shen, Insight into the mechanism of microbially induced carbonate precipitation treatment of bio-improved calcareous sand particles, Acta Geotech. 18 (2023). https://doi.org/10.1007/s11440-022-01625-2.

[65] S. Bhattacharya, S. Subedi, S.J. Lee, N. Pradhananga, Estimation of 3D Sphericity by Volume Measurement – Application to Coarse Aggregates, Transportation Geotechnics 23 (2020). https://doi.org/10.1016/j.trgeo.2020.100344.

[66] Bert C. Aschenbrenner (2), A New Method of Expressing Particle Sphericity, SEPM Journal of Sedimentary Research Vol. 26 (1956). https://doi.org/10.1306/74d704a7-2b21-11d7-8648000102c1865d.

[67] Bernard Swan, Measures of Particle Roundness: A NOTE, SEPM Journal of Sedimentary Research Vol. 44 (1974). https://doi.org/10.1306/74d72a90-2b21-11d7-8648000102c1865d.

[68] M.J. Church, Grain size and shape, in: M.J. and C.M. and H.L.A. and L.F.J. Middleton Gerard V. and Church (Ed.), Encyclopedia of Sediments and Sedimentary Rocks, Springer Netherlands, Dordrecht, 2003: pp. 338–345. https://doi.org/10.1007/978-1-4020-3609-5_104.

[69] Bert C. Aschenbrenner (2), A New Method of Expressing Particle Sphericity, SEPM Journal of Sedimentary Research Vol. 26 (1956). https://doi.org/10.1306/74d704a7-2b21-11d7-8648000102c1865d.

[70] H. Wadell, Volume, Shape, and Roundness of Rock Particles, J. Geol. 40 (1932). https://doi.org/10.1086/623964.

[71] P.J. BARRETT, The shape of rock particles, a critical review, Sedimentology 27 (1980). https://doi.org/10.1111/j.1365-3091.1980.tb01179.x.

[72] J.W. Bullard, E.J. Garboczi, Defining shape measures for 3D star-shaped particles: Sphericity, roundness, and dimensions, Powder Technol. 249 (2013). https://doi.org/10.1016/j.powtec.2013.08.015.

[73] Y. Kim, J. Ma, S.Y. Lim, J.Y. Song, T.S. Yun, Determination of shape parameters of sands: a deep learning approach, Acta Geotech. 17 (2022). https://doi.org/10.1007/s11440-022-01464-1.

[74] J.C. Santamarina, G.C. Cho, Soil behaviour: The role of particle shape, in: Advances in Geotechnical Engineering: The Skempton Conference - Proceedings of a Three Day Conference on Advances in Geotechnical Engineering, Organised by the Institution of Civil Engineers, 2004.

[75] G.-C. Cho, J. Dodds, J.C. Santamarina, Particle Shape Effects on Packing Density, Stiffness, and Strength: Natural and Crushed Sands, Journal of Geotechnical and Geoenvironmental Engineering 132 (2006). https://doi.org/10.1061/(asce)1090-0241(2006)132:5(591).

[76] R.P. Chapuis, Estimating the in situ porosity of sandy soils sampled in boreholes, Eng. Geol. 141–142 (2012). https://doi.org/10.1016/j.enggeo.2012.04.015.

[77] Z. Nie, Z. Liang, X. Wang, A three-dimensional particle roundness evaluation method, Granul. Matter 20 (2018). https://doi.org/10.1007/s10035-018-0802-5.

[78] J. Zheng, R.D. Hryciw, Traditional soil particle sphericity, roundness and surface roughness by computational geometry, Geotechnique 65 (2015). https://doi.org/10.1680/geot.14.P.192.

[79] I. Cavarretta, C. O'Sullivan, M.R. Coop, Applying 2D shape analysis techniques to granular materials with 3D particle geometries, in: AIP Conf. Proc., 2009. https://doi.org/10.1063/1.3180057.

[80] J.R.J. Lee, M.L. Smith, L.N. Smith, P.S. Midha, A mathematical morphology approach to image based 3D particle shape analysis, Mach. Vis. Appl. 16 (2005). https://doi.org/10.1007/s00138-005-0181-x.

[81] C.Y. Kuo, J.D. Frost, J.S. Lai, L.B. Wang, Three-dimensional image analysis of aggregate particles from orthogonal projections, Transp. Res. Rec. (1996). https://doi.org/10.3141/1526-12.

[82] U. Ulusoy, A Review of Particle Shape Effects on Material Properties for Various Engineering Applications: From Macro to Nanoscale, Minerals 13 (2023). https://doi.org/10.3390/min13010091.

[83] M. Fan, D. Su, N. Zhang, G. Cai, X. Chen, Optimizing parameter combinations for clump models enabled by the bubble packing algorithm: Insights from geometrical and morphological approximation of typical geotechnical particles, Comput. Geotech. 180 (2025) 107061. https://doi.org/https://doi.org/10.1016/j.compgeo.2025.107061.

[84] A. Mahmood, T. Akram, H. Chen, S. Chen, On the Evolution of Additive Manufacturing (3D/4D Printing) Technologies: Materials, Applications, and Challenges, Polymers (Basel). 14 (2022). https://doi.org/10.3390/polym14214698.

[85] P. Lakkala, S.R. Munnangi, S. Bandari, M. Repka, Additive manufacturing technologies with emphasis on stereolithography 3D printing in pharmaceutical and medical applications: A review, Int. J. Pharm. X 5 (2023). https://doi.org/10.1016/j.ijpx.2023.100159.

[86] T.D. Ngo, A. Kashani, G. Imbalzano, K.T.Q. Nguyen, D. Hui, Additive manufacturing (3D printing): A review of materials, methods, applications and challenges, Compos. B Eng. 143 (2018). https://doi.org/10.1016/j.compositesb.2018.02.012.

[87] M. sha Huang, M. Zhang, B. Bhandari, Assessing the 3D Printing Precision and Texture Properties of Brown Rice Induced by Infill Levels and Printing Variables, Food Bioproc. Tech. 12 (2019). https://doi.org/10.1007/s11947-019-02287-x.

[88] J. Tabak, Geometry: The Language of Space and Form, Infobase Publishing, 2014.

[89] D. Schulze, Powders and Bulk Solids: Behavior, Characterization, Storage and Flow, Second Edition, 2021. https://doi.org/10.1007/978-3-030-76720-4.

[90] D.S. Shah, K.K. Moravkar, D.K. Jha, V. Lonkar, P.D. Amin, S.S. Chalikwar, A concise summary of powder processing methodologies for flow enhancement, Heliyon 9 (2023). https://doi.org/10.1016/j.heliyon.2023.e16498.

[91] M. Irfan, A Simple Method for Generation of Statistical Tables by the Help of Excel Software, Journal of Social and Development Sciences 2 (2011). https://doi.org/10.22610/jsds.v2i1.651.

[92] C.J. Coetzee, S.G. Lombard, Discrete element method modelling of a centrifugal fertiliser spreader, Biosyst. Eng. 109 (2011). https://doi.org/10.1016/j.biosystemseng.2011.04.011.

[93] M. Zeghal, T.B. Edil, M.E. Plesha, Discrete Element Method for Sand-Structure Interaction, in: 2002. https://doi.org/10.1061/40647(259)56.

[94] J.K. Prescott, R.A. Barnum, On powder flowability, Pharmaceutical Technology 24 (2000) 60.

[95] V. Ganesan, K.A. Rosentrater, K. Muthukumarappan, Flowability and handling characteristics of bulk solids and powders - a review with implications for DDGS, Biosyst. Eng. 101 (2008). https://doi.org/10.1016/j.biosystemseng.2008.09.008.

[96] W. Chen, A. Roberts, K. Williams, J. Miller, J. Plinke, On uniaxial compression and Jenike direct shear testings of cohesive iron ore materials, Powder Technol. 312 (2017). https://doi.org/10.1016/j.powtec.2017.02.037.

[97] A.S. CAGLI, B.N. DEVECI, C.H. OKUTAN, D.A.A. SIRKECI, E.Y. TEOMAN, 044 Flow property measurement using the Jenike shear cell for 7 different bulk solids, Proceedings of European Congress of Chemical Engineering (ECCE-6) (2007).

[98] R.J. Berry, M.S.A. Bradley, Investigation of the effect of test procedure factors on the failure loci and derived failure functions obtained from annular shear cells, Powder Technol. 174 (2007). https://doi.org/10.1016/j.powtec.2006.10.023.

[99] H. Kalman, Effect of moisture content on flowability: Angle of repose, tilting angle, and Hausner ratio, Powder Technol. 393 (2021). https://doi.org/10.1016/j.powtec.2021.08.010.

[100] F. Elekes, E.J.R. Parteli, An expression for the angle of repose of dry cohesive granular materials on Earth and in planetary environments, Proc. Natl. Acad. Sci. U. S. A. 118 (2021). https://doi.org/10.1073/pnas.2107965118.

[101] D. Müller, E. Fimbinger, C. Brand, Algorithm for the determination of the angle of repose in bulk material analysis, Powder Technol. 383 (2021). https://doi.org/10.1016/j.powtec.2021.01.010.

[102] H. Kalman, Quantification of mechanisms governing the angle of repose, angle of tilting, and Hausner ratio to estimate the flowability of particulate materials, Powder Technol. 382 (2021). https://doi.org/10.1016/j.powtec.2021.01.012.

[103] T. Roessler, A. Katterfeld, Scalability of angle of repose tests for the calibration of DEM parameters, in: ICBMH 2016 - 12th International Conference on Bulk Materials Storage, Handling and Transportation, Proceedings, 2016.

[104] S.M. Derakhshani, D.L. Schott, G. Lodewijks, Micro-macro properties of quartz sand: Experimental investigation and DEM simulation, Powder Technol. 269 (2015). https://doi.org/10.1016/j.powtec.2014.08.072.

[105] Y. Shen, P. Sun, Z. Zhang, Y. Wang, B. Zheng, A tube heat transfer prediction model considering static friction coefficient of dense particle flow, Int. J. Heat Mass Transf. 205 (2023). https://doi.org/10.1016/j.ijheatmasstransfer.2023.123902.

[106] S.K. Wilkinson, S.A. Turnbull, Z. Yan, E.H. Stitt, M. Marigo, A parametric evaluation of powder flowability using a Freeman rheometer through statistical and sensitivity analysis: A discrete element method (DEM) study, Comput. Chem. Eng. 97 (2017). https://doi.org/10.1016/j.compchemeng.2016.11.034.

[107] L. Markman, Flow Behaviour of Pellets: Design of a Mass Flow Hopper for Biomass and Waste Pellets in an HTW Gasification Plant, Delft University of Technology, 2023.

[108] N. Nuño, R. Groppetti, N. Senin, Static coefficient of friction between stainless steel and PMMA used in cemented hip and knee implants, Clinical Biomechanics 21 (2006). https://doi.org/10.1016/j.clinbiomech.2006.05.008.

[109] M. Stasiak, M. Molenda, M. Bańda, J. Wiącek, P. Parafiniuk, A. Lisowski, M. Gancarz, E. Gondek, Mechanical characteristics of pine biomass of different sizes and shapes, European Journal of Wood and Wood Products 77 (2019). https://doi.org/10.1007/s00107-019-01415-w.

[110] A. Mahajan, I. Dafnomilis, V. Hancock, G. Lodewijks, D. Schott, Assessing the representativeness of durability tests for wood pellets by DEM Simulation - Comparing conditions in a durability test with transfer chutes, in: EPJ Web Conf., 2017. https://doi.org/10.1051/epjconf/201714015004.

[111] R.H. Dean, A.P. Turner, A.B. Koc, R. Karthikeyan, INFLUENCE OF MOISTURE CONTENT AND FINE LEVELS ON ANGLE OF REPOSE FOR PELLETIZED MATERIALS, Appl. Eng. Agric. 39 (2023). https://doi.org/10.13031/aea.15141.

[112] M.A. Madrid, J.M. Fuentes, F. Ayuga, E. Gallego, Determination of the Angle of Repose and Coefficient of Rolling Friction for Wood Pellets, Agronomy 12 (2022). https://doi.org/10.3390/agronomy12020424.

[113] P.C. Austin, J.E. Hux, A brief note on overlapping confidence intervals, J. Vasc. Surg. 36 (2002). https://doi.org/10.1067/mva.2002.125015.

[114] S.M. Shafaei, S. Kamgar, A comprehensive investigation on static and dynamic friction coefficients of wheat grain with the adoption of statistical analysis, J. Adv. Res. 8 (2017). https://doi.org/10.1016/j.jare.2017.04.003.

[115] J.S. Weaver, J. Whiting, V. Tondare, C. Beauchamp, M. Peltz, J. Tarr, T.Q. Phan, M.A. Donmez, The effects of particle size distribution on the rheological properties of the powder and the mechanical properties of additively manufactured 17-4 PH stainless steel, Addit. Manuf. 39 (2021). https://doi.org/10.1016/j.addma.2021.101851.

[116] M.A. Kaleem, M.Z. Alam, M. Khan, S.H.I. Jaffery, B. Rashid, An experimental investigation on accuracy of Hausner Ratio and Carr Index of powders in additive manufacturing processes, Metal Powder Report 76 (2021). https://doi.org/10.1016/j.mprp.2020.06.061.

Appendix A: Research Paper

From Sinter to Print

Linking Particle Shape and Flowability

Erol Asad Pour, Ahmed Hadi, Hao Shi &, Dingena Schott
Department of Maritime and Transport Technology, Faculty of Mechanical Engineering, Delft University of Technology, Delft 2628CD, the Netherlands

Abstract— **Iron ore sinter particles have highly irregular shapes that influence how they pack and flow in bulk, which affects gas flow and reaction efficiency inside the blast furnace. To improve the efficiency of steelmaking processes, these particles are often studied using DEM simulations in which their complex shapes are simplified (generally as spheres), creating a need to understand how such geometric simplification influences bulk behaviour. In this study, the computational load associated with representing complex particle shapes in DEM simulations is overcome by transferring particle shape complexity from the numerical to the physical domain through the fabrication of 3D-printed sinter particle replicas with varying levels of geometric simplification.**

Three DEM shape representations, multi-sphere, polyhedral, and super-ellipsoid, were compared to determine the most suitable shape modelling approach. As irregularly shaped and angular sinter particles are best represented through faceted geometries, the polyhedral approach was selected as the sole modelling method for this study. To quantify the deviations in shape across various simplification levels, the shape descriptors (sphericity, convexity, and roundness) were applied. Comparisons of flowability metrics, such as angle of repose, coefficient of static friction (particle-wall), and Hausner ratio, demonstrated that, despite geometric simplification, bulk flow behaviour remained largely unchanged. A critical threshold near 400 faces was identified, below which particle morphology deviates more sharply from the original shape; nonetheless, the corresponding changes in flowability metrics were minimal, showing that even substantial simplification applying the polyhedral model does not significantly change the macroscopic flow behaviour of sinter particle assemblies

Keywords- Sinter; Flowability 3D-Printing; Shape modelling; Polyhedrons; DEM

1. INTRODUCTION

Granular materials are collections of discrete particles (micrometres to metres) governed by interactions, energy dissipation, and collective dynamics and are broadly handled across numerous industrial processes [1,2].

In the steel industry, sinter (granular fused iron ore) is a key component of the blast furnace burden [3]. Sinter particles have highly irregular shapes and heterogeneous internal structures, with smooth, dense regions and fractured, porous surfaces. Their textures reflect partial melting and solidification during sintering, producing angular, feature-rich geometries (Figure 1). Understanding sinter bulk behaviour is essential for furnace optimization, stable burden descent, and resource efficiency.

DEM, introduced by Cundall and Strack, models granular materials by resolving particle-scale positions, velocities, and stresses [4–6]. In many DEM models, particles are approximated as spheres for low computational cost [7], though shape significantly affects bulk behaviour. Accurately capturing this shape effect is thus one of the most demanding aspects of DEM modelling [8–11].

Despite growing recognition of the importance of particle shape, accurately representing complex particle shapes in DEM simulations comes with a substantial computational cost. For instance Diviš et al. [12] showed that spherical-particle simulations complete in under an hour, whereas polyhedral-particle simulations require 7–8 hours, increasing total computation time from days (for spheres) to weeks (for polyhedra) when scaled to 81 simulations. Although non-spherical particle models have been widely adopted [13–15] to capture shape effects, the degree of shape simplification that can be applied without loss of accuracy remains unclear. To address this, a representative particle shape was selected as a reference model, and 1,000 identical particles of each simplified version were 3D-printed per model.

By transferring geometric complexity to the physical domain, flowability experiments can generate high-quality reference data without the computational cost of DEM [16]. This study focuses on flowability, quantified for 3D-printed sinter particles at different simplification levels using angle of repose, static friction coefficient, and Hausner ratio.

2. METHODS

2.1 Particle Shape Models

To simplify irregularly shaped particles, widely adopted particle shape models are considered to ensure reproducibility and relevance for future DEM studies. The most applied approaches in DEM simulations are multi-sphere, polyhedral and super-ellipsoid models [17–19]. These models were compared to identify which best captures the geometry of irregular sinter particles (Figure 1).

Figure 1: Images of an irregularly shaped sinter particle [20]

The multi-sphere model represents particles as assemblies of overlapping spheres arranged to preserve either external geometry (control geometry, CG-24; Figure 2a) or particle volume (control volume, CV-24; Figure 2c), where 24 denotes the number of overlapping spheres, and is widely used in DEM due to efficient sphere–sphere contact detection [21–24]. One limitation of this model is its ability to accurately capture flat faces and sharp edges, due to the overlapping sub-spheres it consists of [24,25].

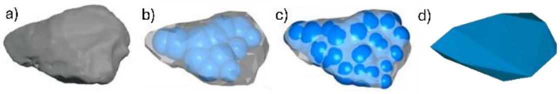

Figure 2: a) Real shape; b) CG-24; c) CV-24; d) Polyh-32 [17]

The polyhedral method captures particle shapes by discretising them it into planar faces (Polyh-32; Figure 2a), where 32 denotes the number of faces. This model accurately represents sharp edges, flat faces, and angular features [17,18], but incurs high computational cost in DEM due to complex plane–edge contact calculations [26–28].

The super-ellipsoid method offers a mathematical formula (Equation 1) which by adjusting the parameters (a, b, c, s1, s2), the output shape can vary from spherical to rectangular (Figure 3). This model is only restricted to model a certain range of convex regular shapes and is thus only applicable to simulate granular materials with particles having these shapes.

$$f(x,y,z) = \left(\left|\frac{x}{a}\right|^{s_2} + \left|\frac{y}{b}\right|^{s_2}\right)^{\frac{s_1}{s_2}} + \left|\frac{z}{c}\right|^{s_1} - 1 = 0 \quad (1)$$

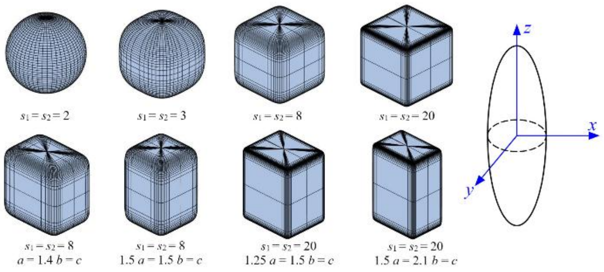

Figure 3: Range of shapes captured by super-ellipsoid model [17]

As this study focuses on highly irregular sinter particles, capturing flat faces and sharp edges is essential. Therefore, the polyhedral method was selected. Although this approach is computationally expensive in DEM, it does not represent a limitation in the present work, as 3D-printed particles are used in the experiments.

2.2 Particle Shape Descriptors

Particle shape descriptors are metrics applied to quantify the shape of a particle, which can be characterised through three hierarchical components: form, roundness and roughness, as illustrated in Figure 4.

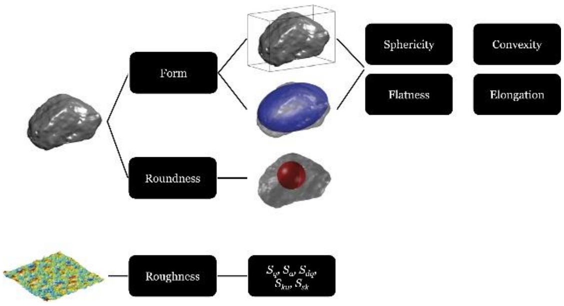

Figure 4: Particle shape aspects and descriptors [29]

Form, quantified by sphericity and convexity, measures overall geometry. Sphericity (φ, 0–1) indicates deviation from a perfect sphere, with 1 denoting an ideal sphere, and is computed as defined by Wadell (Equation 2), where V_p and S_p are the particle's volume and surface area [30].

$$\varphi = \frac{\pi^{\frac{1}{3}}\left(6V_p\right)^{\frac{2}{3}}}{S_p} \tag{2}$$

Convexity (Equation 3) measures how closely a particle approaches its convex hull, with values near 1 indicating fully convex shapes [31], where V and V_{CH} are the particle and convex hull volumes [29,32].

$$Convexity = \frac{V}{V_{CH}} \tag{3}$$

Since spheres are generally used in DEM simulations for low computational cost [33], this study focuses on quantifying deviations in general particle form compared to these ideal spheres, which affect flowability. As specific combinations of elongation and flatness correspond to unique sphericity values, their joint geometric effect is already captured by the sphericity measure [34] (Figure 5). As such, elongation and flatness are not considered separately. Overall form is quantified using sphericity and convexity, calculated from the STL files of the original and simplified particles via MATLAB [35].

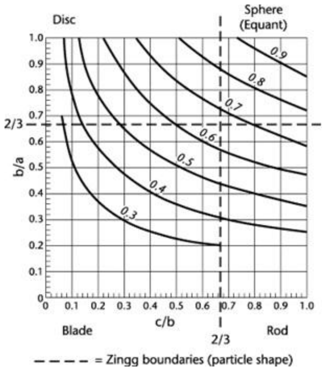

Figure 5: Chart to determine Krumbein intercept sphericity [34,36]

Roundness (R) denotes the roundness of the particle edges, being the inverse of angularity [37–39]. It is calculated as the ratio of the mean corner radius to the maximum inscribed radius (Equation 4) [30]:

$$R = \frac{\frac{1}{n}\sum_{i=1}^{n} r_i}{r_{ins}} \tag{4}$$

where n is the number of corners, r_i is the corner radius and r_{ins} is the maximum inscribed circle radius. Since 2D roundness depends on a single projection and may vary with angle [40], a 3D estimate is obtained by averaging values from three orthogonal projections (YZ, XZ, XY) [41–43]. Projection images were generated in SolidWorks, converted to binary, and processed in MATLAB [35], where radii were computed via a corner-fitting algorithm [44]. Roundness is then obtained as the ratio of the mean corner radius to the inscribed circle radius

2.3 3D Printing Process

3D printing builds objects layer by layer from a 3D digital model (e.g., STL file) [45–47]. Fused Deposition Modelling (FDM) was used to print the simplified models, consistent with the original FDM-printed reference particles (Figure 6a). The specifications of the 3D printer and its parameters are presented in Table 1.

Table 1: 3D printer models and parameters

	Original Prusa XL	**Bambu Lab A1**
Method	FDM	FDM
Build Area	360x360x360 mm	256x256x256 mm
Layer height	0.2 mm	0.2 mm
Nozzle diameter	0.4 mm	0.4 mm

To isolate particle shape effects on flowability, the STL files of the simplified models were scaled to match the volume of the reference particle.

Particle mass was adjusted by modifying the 3D-printing infill ratio. The target mass was set as the mean weight of four original particles (400,000 face model), with uncertainty estimated at 95% confidence. Because predicted masses from the slicing software can differ from actual prints, sample particles of each simplified model were printed at varying infill ratios, measured, and the ratio yielding a mean mass closest to the target was selected.

A sample size of 1,000 particles per model was chosen for statistically meaningful flowability measurements, as in DEM simulations [48,49]. Additionally, different colours were employed to distinguish models (Figure 6).

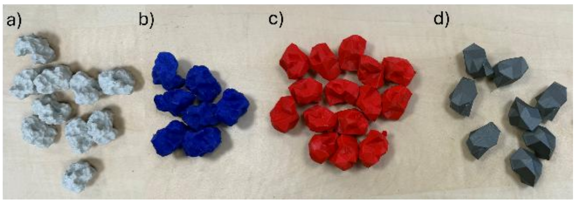

Figure 6: a) 400,000 face model; b) 400 face model; c) 100 face model; d) 40 face model

To guarantee sufficient material for printing, the batch mass was estimated based on the total particle mass. Variability and support material were taken into consideration by adding an additional 20% to the total mass of the particles.

Bulk printing was limited by printer build volumes (Table 1), allowing up to 100 particles per batch on the Prusa XL and 50 on the Bambu Lab A1. Printing time per particle ranged from 37 minutes (400-face model) to 30 minutes (40-face model), resulting in 13–20 days to produce 1,000 particles per model [35].

Testing all mesh resolutions was infeasible, so three representative models were selected: 400-face (threshold resolution), 40-face (most simplified), and 100-face (intermediate). Threshold and intermediate resolution will be addressed in detail in the results section. This selection balances coverage of the simplification range with fabrication constraints.

2.4. Flowability Indicators

Flowability can be measured using precise but time-consuming methods such as shear testers [50–52], or using parameters that correlate with flowability [53]. As this study focuses on relative changes in flowability between original and simplified particles, flowability indicators, including angle of repose (AoR), coefficient of static friction (μ_s), and Hausner ratio (HR), were used.

The AoR is the maximum slope angle at which a granular pile remains stable [54,55]. A higher AoR implies poorer flowability, ranging from 'very free-flowing' (at AoR 25°-30°) to 'very cohesive' (at AoR > 55°) [2,55]. AoR measurements vary with method due to contributions from wall friction, local particle avalanching, and internal shear governed by material friction [56]. To reduce wall-sliding effects and emphasize internal shear, the ledge test was selected, as the box edge limits particle motion along the bottom surface (Figure 7).

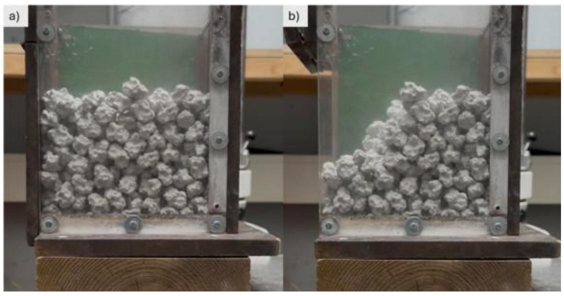

Figure 7: Ledge box: a) front gate closed; b) front gate open

The ledge test is performed by filling the box to a 140 mm height and opening the front gate to allow free discharge. Once flow stops, a stable slope forms and is photographed from a tripod. This process was repeated 15 times. The resulting images were used to measure the AoR. A limitation of AoR measurements is that materials consisting of sticky, highly angular, or broadly size-distributed particles may not form ideal conical heaps (Figure 8) [2,57].

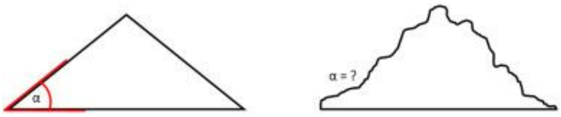

Figure 8: 'ideal' vs. 'non-ideal' conical heap of granular material [55]

To reduce subjectivity in AoR measurements, a MATLAB code is applied [35] that converts processed heap images to binary form, extracts heap-edge coordinates, fits a linear regression to the slope, and computes the AoR via the arctangent of the fitted gradient. Prior to analysis, images are cropped to the region of interest, the background is set to green, and particle colour is adjusted to white if its colour isn't white/grey (Figure A1)

The coefficient of static friction (μ_s) is the ratio of maximum static friction to normal force between surfaces at rest. Higher μ_s indicates greater resistance to motion and lower flowability. [58,59].

The μ_s was measured through an inclined surface tester (Figure 9) at two scales: the bulk level and single-particle level. This tester displays the wall friction angle θ_w to one decimal, used in Equation 5.

$$\mu_s = \tan(\theta_w) \tag{5}$$

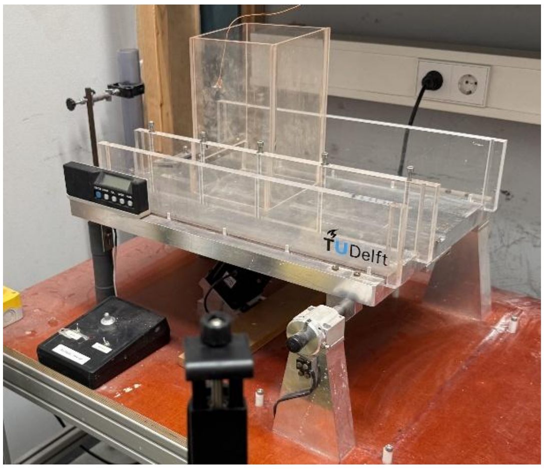

Figure 9: Inclined surface tester, with a test-box on it (used for the bulk level test)

The bulk test used a plexiglass box on a steel base (140 × 140 × 140 mm³, Figure 9), filled with particles to 140 mm. The top was levelled, and the inclination angle was gradually increased until sliding, repeated 15 times per model. The low plexiglass–steel friction (0.3–0.4 [60]) is likely to have only a minor influence on results. Single-particle tests were performed similarly, using either random placement or controlled placement (Figure 10) to examine the effect of particle orientation and location on the wall friction angle. All these tests were video-recorded, in order to conduct a frame-by-frame analysis to accurately identify the θ_w .

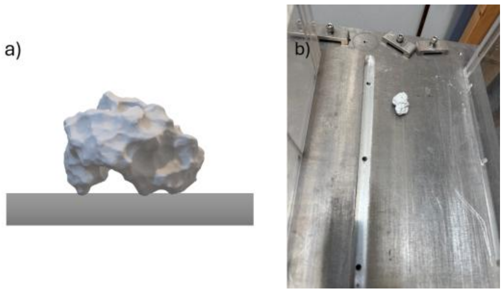

Figure 10: Controlled placement test; a) side view of the chosen orientation; b) position of the particle

The Hausner Ratio (HR) is the ratio of the tapped density ρ_t and the bulk density ρ_b (Equation 6), with higher values indicating poorer flowability, ranging from 'excellent' (at HR < 1.11) to 'very very poor' (at HR > 1.59) [56].

$$HR = \frac{\rho_T}{\rho_B} \tag{6}$$

HR measurements were performed using a 2 L graduated cylinder (20 mL resolution). The empty cylinder was weighed five times and the mean mass was recorded. Particles were added to 1 L (V_0), manually tapped 180 times, and the final compacted volume (V_t) was measured. Bulk and tapped densities were calculated by dividing the particle mass (corrected for cylinder weight) by V_0 and V_t, respectively. Each measurement was repeated five times, and these densities were used to compute HR.

3. RESULTS

3.1 Shape Simplification Effects

Particle shape changes with simplification were quantified using sphericity, convexity, and roundness, computed for the original (~400,000 faces) and simplified models (40,000; 10,000; 1,000; 400; 300; 150; 100; 80; 40 faces).

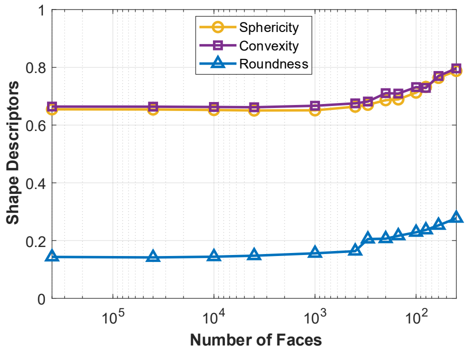

Figure 11: Shape Descriptors (sphericity, convexity, and roundness) vs. Number of faces

Figure 11 shows that decreasing face count increases sphericity, convexity, and roundness, with changes becoming notable below the threshold resolution. Across 400,000–40 faces, sphericity increases from 0.66 to 0.79, remaining in the 'Spherical/Equant' category [61]. The convexity increases from 0.66 (at 400,000 faces) to 0.80 (at 40 faces), indicating that as the particle gets simplified the coarser meshes 'fill in' the indentations of the particle [35].

Roundness increases as face count decreases, from 0.14 (400,000 faces) to 0.16 (400 faces), 0.21 (300 faces), 0.25 (60 faces), and 0.28 (40 faces), indicating a qualitative shift from 'very angular' (400,000–400 faces) to 'angular' (300–60 faces) and 'sub-angular' (40 faces) [61,62].

Relative changes in sphericity, convexity, and roundness to the original shape (Table A1) were computed and combined into an average absolute shape deviation, calculated as an unweighted mean; assuming equal contribution of each descriptor in the absence of information on their relative importance. This provides a quantitative measure of morphological deviation due to mesh simplification. Following [63], a 5% relative change is used as a practical threshold, reflecting that small changes indicate negligible shape differences. Although that study examined DEM clumps, the same criterion is assumed here to indicate sufficient convergence of 3D-printed sinter particle shapes. Using this method, the threshold resolution is approximately 400 faces, where the average absolute shape deviation nears the 5% threshold.

The intermediate model between the threshold and simplest resolution is determined by averaging the sphericity, convexity, and roundness of the 400- and 40-face models to define a target midpoint in 3D descriptor space. For candidate models (60–300 faces), the Euclidean distance to this midpoint is computed, and the model with the smallest distance (the 100-face model) is selected, providing an objective and reproducible criterion.

3.2 Flowability changes

Flowability was assessed using the AoR, μ_s on bulk and particle level, and the HR. With increasing mesh simplification, the mean AoR decreases slightly from 48.9° (400,000 faces) to 44.4° (40 faces) (Figure 12, Table A2). All models except the 40-face case remain within the 'cohesive' range, while the 40-face model lies at the upper limit of 'fair flowing' [2,55].

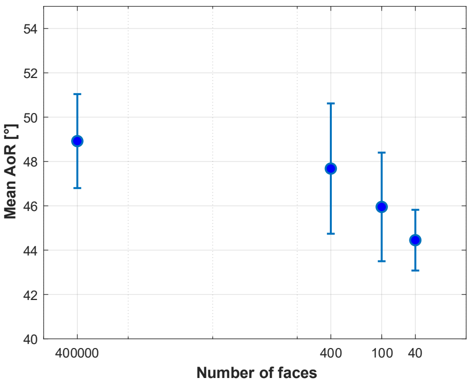

Figure 12: Mean AoR with 95% confidence intervals for the 400,000-, 400-, 100-, and 40-face model

Deviations of the AoR from the reference AoR become appear to be significant below 100 faces. These changes are reported to be most sensitive to changes in sphericity, followed by convexity, with roundness having a smaller influence [35].

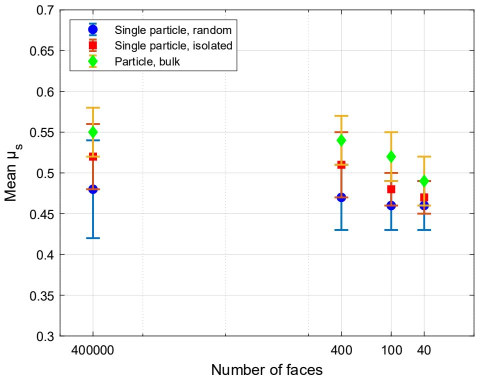

Figure 13: Mean μ_s and 95% confidence intervals for different face counts at the single-particle (random or controlled placement) and bulk levels.

Figure 13 shows mean μ_s across mesh resolutions for single and bulk cases. For the random placement, μ_s decreases slightly from 0.48 (400,000 faces) to 0.46 (40 faces) (Table A3) In the controlled placement test, values are slightly higher, decreasing from 0.52 to 0.47, with noticeable changes appearing at resolutions below 400 faces (Table A4). Bulk measurements show higher μ_s overall, decreasing from 0.55 to 0.49 (Table A5), with more pronounced changes appearing at mesh resolutions below 100 faces. These reductions may be associated with changes in sphericity and convexity, while roundness appears to have a smaller influence [35].

The mean HR decreases slightly as the mesh resolution decreases (Figure 14), from 1.45 (400,000 faces) to 1.32 (40 faces) (Table A6). Based on standard classifications from [56] the 400,000-, 400-, and 100-face fall within the 'poor flowability' range, while the 40-face model lies at the upper limit of 'passable'.

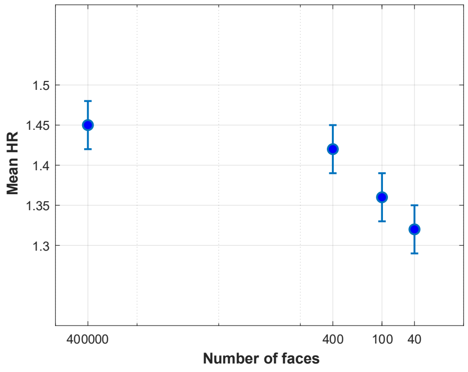

Figure 14: Mean HR with 95% confidence intervals for the 400,000-, 400-, 100-, and 40-face model

Deviations of the HR from the reference HR become apparent below 400 faces and might be mainly associated with increases in sphericity, followed by convexity, with roundness having a smaller influence [35].

4. CONCLUSION AND DISCUSSION

This study evaluated how simplifying irregular sinter particles affects bulk flow using 3D-printed particles. Particle shapes were simplified with polyhedral models at various resolutions, and deviations were quantified using sphericity, convexity, and roundness. Shape descriptors increase notably below the threshold, with 400 faces chosen as the threshold resolution based on the assumption that sphericity, convexity, and roundness contribute equally to overall shape change relative to the 400,000-face model. Flowability was assessed via AoR, μ_s, and HR, comparing the 400-, 100-, and 40-face models to the 400,000-face reference. AoR, μ_s, and HR slightly decrease with lower mesh resolution, with noticeable changes below 400 faces for μ_s (single, controlled) and HR, and below 100 faces for AoR and μ_s (bulk).

These changes generally align with increases in sphericity and convexity, while roundness appears to have a smaller effect. Most simplified models (400- and 100-face) remain in the original flowability class ('cohesive' AoR, 'poor' HR), with only the 40-face model approaching the upper edge of the next lower class ('fair flowing' AoR, 'passable' HR). These results suggest that polyhedral simplification from 400,000 to 40 faces has minor effects on flowability, with most models retaining the original classification, while the 40-face model nears the upper edge of the next lower category. This implies that a resolution between 100 and 40 faces may still preserve the original flowability class.

This study is limited to a batches of uniform particles; future work could examine particle size and shape distributions, more extreme simplifications (<40 faces), alternative simplification methods (e.g., multi-sphere or super-ellipsoid), and improve printing efficiency with larger industrial printers.

Overall, this work provides a basis for calibrating DEM models with simplified polyhedral particles using measurable flowability metrics, enabling efficient realistic simulations.

REFERENCES

[1] Q. Sun, G. Wang, K. Hu, Some open problems in granular matter mechanics, Progress in Natural Science 19 (2009). https://doi.org/10.1016/j.pnsc.2008.06.023.

[2] H.M. Beakawi Al-Hashemi, O.S. Baghabra Al-Amoudi, A review on the angle of repose of granular materials, Powder Technol. 330 (2018). https://doi.org/10.1016/j.powtec.2018.02.003.

[3] L. Lu, O. Ishiyama, 14 - Iron ore sintering, in: L. Lu (Ed.), Iron Ore, Woodhead Publishing, 2015: pp. 395–433. https://doi.org/https://doi.org/10.1016/B978-1-78242-156-6.00014-9.

[4] B.K. Mishra, R.K. Rajamani, The discrete element method for the simulation of ball mills, Appl. Math. Model. 16 (1992). https://doi.org/10.1016/0307-904X(92)90035-2.

[5] A.B. Yu, Discrete element method: An effective way for particle scale research of particulate matter, in: Engineering Computations (Swansea, Wales), 2004. https://doi.org/10.1108/02644400410519749.

[6] P.A. Cundall, O.D.L. Strack, A discrete numerical model for granular assemblies, Geotechnique 29 (1979). https://doi.org/10.1680/geot.1979.29.1.47.

[7] C. Coetzee, Calibration of the discrete element method: Strategies for spherical and non-spherical particles, Powder Technol. 364 (2020). https://doi.org/10.1016/j.powtec.2020.01.076.

[8] D. Höhner, S. Wirtz, V. Scherer, Experimental and numerical investigation on the influence of particle shape and shape approximation on hopper discharge using the discrete element method, Powder Technol. 235 (2013). https://doi.org/10.1016/j.powtec.2012.11.004.

[9] D. Markauskas, R. Kačianauskas, A. Džiugys, R. Navakas, Investigation of adequacy of multi-sphere approximation of elliptical particles for DEM simulations, Granul. Matter 12 (2010). https://doi.org/10.1007/s10035-009-0158-y.

[10] P.W. Cleary, DEM prediction of industrial and geophysical particle flows, Particuology 8 (2010). https://doi.org/10.1016/j.partic.2009.05.006.

[11] P.W. Cleary, M.L. Sawley, DEM modelling of industrial granular flows: 3D case studies and the effect of particle shape on hopper discharge, Appl. Math. Model. 26 (2002). https://doi.org/10.1016/S0307-904X(01)00050-6.

[12] J. Diviš, D. Žurovec, Á. Ramírez-Gómez, J. Hlosta, J. Rozbroj, K. Pokorná, J. Nečas, J. Zegzulka, DEM calibration insights on the role of particle shape for sub 2 mm particles, Sci. Rep. 15 (2025) 20477. https://doi.org/10.1038/s41598-025-04592-2.

[13] G. Lu, J.R. Third, C.R. Müller, Discrete element models for non-spherical particle systems: From theoretical developments to applications, Chem. Eng. Sci. 127 (2015). https://doi.org/10.1016/j.ces.2014.11.050.

[14] C. Xie, T. Song, Y. Zhao, Discrete element modeling and simulation of non-spherical particles using polyhedrons and super-ellipsoids, Powder Technol. 368 (2020). https://doi.org/10.1016/j.powtec.2020.05.008.

[15] Z. Liu, H. Ma, Y. Zhao, Comparative study of discrete element modeling of tablets using multi-spheres, multi-super-ellipsoids, and polyhedrons, Powder Technol. 390 (2021). https://doi.org/10.1016/j.powtec.2021.05.065.

[16] B. and L.S.J. and S.B. Su Yu-Feng and Zhang, Parametric Sensitivity Study of Particle Shape Effect Through 3D Printing, in: Y. and M.G. Li Xikui and Feng (Ed.), Proceedings of the 7th International Conference on Discrete Element Methods, Springer Singapore, Singapore, 2017: pp. 593–600.

[17] H. Ma, X. Xia, L. Zhou, C. Xu, Z. Liu, T. Song, G. Zou, Y. Liu, Z. Huang, X. Liao, Y. Zhao, A Comparative Study of the Performance of Different Particle Models in Simulating Particle Charging and Burden Distribution in a Blast Furnace within the DEM Framework, Energies (Basel). 16 (2023). https://doi.org/10.3390/en16093890.

[18] H. Ma, L. Zhou, Z. Liu, M. Chen, X. Xia, Y. Zhao, A review of recent development for the CFD-DEM investigations of non-spherical particles, Powder Technol. 412 (2022). https://doi.org/10.1016/j.powtec.2022.117972.

[19] Y. You, Y. Zhao, Discrete element modelling of ellipsoidal particles using super-ellipsoids and multi-spheres: A comparative study, Powder Technol. 331 (2018). https://doi.org/10.1016/j.powtec.2018.03.017.

[20] M. Li, Y. Yu, H. Saxén, Numerical and experimental study of particle shape effect on pile properties based on a 3D sinter model, Powder Technol. 452 (2025) 120496. https://doi.org/https://doi.org/10.1016/j.powtec.2024.120496.

[21] M.H. Abbaspour-Fard, Theoretical validation of a multi-sphere, discrete element model suitable for biomaterials handling simulation, Biosyst. Eng. 88 (2004). https://doi.org/10.1016/j.biosystemseng.2004.03.010.

[22] J.F. Favier, M.H. Abbaspour-Fard, M. Kremmer, A.O. Raji, Shape representation of axi-symmetrical, non-spherical particles in discrete element simulation using multi-element model particles, Engineering Computations (Swansea, Wales) 16 (1999). https://doi.org/10.1108/02644409910271894.

[23] R.P. Jensen, P.J. Bosscher, M.E. Plesha, T.B. Edil, DEM simulation of granular media-structure interface: Effects of surface roughness and particle shape, Int. J. Numer. Anal. Methods Geomech. 23 (1999). https://doi.org/10.1002/(SICI)1096-9853(199905)23:6<531::AID-NAG980>3.0.CO;2-V.

[24] H. Kruggel-Emden, S. Rickelt, S. Wirtz, V. Scherer, A study on the validity of the multi-sphere Discrete Element Method, Powder Technol. 188 (2008). https://doi.org/10.1016/j.powtec.2008.04.037.

[25] F.L. Yuan, M. Sommerfeld, P. Muramulla, S. Gopireddy, L. Pasternak, N. Urbanetz, T. Profitlich, Rigid3D: a hybrid multi-sphere DEM framework for simulation of non-spherical particles in multi-phase flow, ArXiv Preprint ArXiv:2306.13678 (2023).

[26] T.A. Shoemaker, C. Tanissa, Y.M.A. Hashash, Comparison of DEM Software with Polyhedral Particle Shapes, in: 2024. https://doi.org/10.1061/9780784485347.012.

[27] E. Illana, K. Qyteti, M. Scharnowski, M. Brömmer, S. Wirtz, V. Scherer, Shape-changing particles for locally resolved particle geometry in DEM simulations, Particuology 89 (2024). https://doi.org/10.1016/j.partic.2023.11.003.

[28] S. Zhang, A.M. Zsáki, Effect Geometric Detail on the Outcome of DEM Simulations with Polyhedral Particles, Geomechanics and Geoengineering 18 (2023). https://doi.org/10.1080/17486025.2022.2065037.

[29] V. Angelidakis, S. Nadimi, S. Utili, SHape Analyser for Particle Engineering (SHAPE): Seamless characterisation and simplification of particle morphology from imaging data, Comput. Phys. Commun. 265 (2021). https://doi.org/10.1016/j.cpc.2021.107983.

[30] H. Wadell, Volume, Shape, and Roundness of Rock Particles, J. Geol. 40 (1932). https://doi.org/10.1086/623964.

[31] J. Žunić, P.L. Rosin, Measuring Shapes with Desired Convex Polygons, IEEE Trans. Pattern Anal. Mach. Intell. 42 (2020). https://doi.org/10.1109/TPAMI.2019.2898830.

[32] R.D. Beemer, L. Li, A. Leonti, J. Shaw, J. Fonseca, I. Valova, M. Iskander, C.H. Pilskaln, Comparison of 2D Optical Imaging and 3D Microtomography Shape Measurements of a Coastal Bioclastic Calcareous Sand, J. Imaging 8 (2022). https://doi.org/10.3390/jimaging8030072.

[33] B. Soltanbeigi, A. Podlozhnyuk, S.A. Papanicolopulos, C. Kloss, S. Pirker, J.Y. Ooi, DEM study of mechanical characteristics of multi-spherical and superquadric particles at micro and macro scales, Powder Technol. 329 (2018). https://doi.org/10.1016/j.powtec.2018.01.082.

[34] W.C. Krumbein, MEASUREMENT AND GEOLOGICAL SIGNIFICANCE OF SHAPE AND ROUNDNESS OF SEDIMENTARY PARTICLES, Journal of Sedimentary Research 11 (1941). https://doi.org/10.1306/D42690F3-2B26-11D7-8648000102C1865D.

[35] E. Asad Pour, From Sinter to Print: Linking Particle Shape and Flowability, Delft University of Technology, 2026.

[36] M.J. Church, Grain size and shape, in: M.J. and C.M. and H.L.A. and L.F.J. Middleton Gerard V. and Church (Ed.), Encyclopedia of Sediments and Sedimentary Rocks, Springer Netherlands, Dordrecht, 2003: pp. 338–345. https://doi.org/10.1007/978-1-4020-3609-5_104.

[37] P.J. BARRETT, The shape of rock particles, a critical review, Sedimentology 27 (1980). https://doi.org/10.1111/j.1365-3091.1980.tb01179.x.

[38] S.J. Blott, K. Pye, Particle shape: A review and new methods of characterization and classification, Sedimentology 55 (2008). https://doi.org/10.1111/j.1365-3091.2007.00892.x.

[39] J.W. Bullard, E.J. Garboczi, Defining shape measures for 3D star-shaped particles: Sphericity, roundness, and dimensions, Powder Technol. 249 (2013). https://doi.org/10.1016/j.powtec.2013.08.015.

[40] Z. Nie, Z. Liang, X. Wang, A three-dimensional particle roundness evaluation method, Granul. Matter 20 (2018). https://doi.org/10.1007/s10035-018-0802-5.

[41] I. Cavarretta, C. O'Sullivan, M.R. Coop, Applying 2D shape analysis techniques to granular materials with 3D particle geometries, in: AIP Conf. Proc., 2009. https://doi.org/10.1063/1.3180057.

[42] J.R.J. Lee, M.L. Smith, L.N. Smith, P.S. Midha, A mathematical morphology approach to image based 3D particle shape analysis, Mach. Vis. Appl. 16 (2005). https://doi.org/10.1007/s00138-005-0181-x.

[43] C.Y. Kuo, J.D. Frost, J.S. Lai, L.B. Wang, Three-dimensional image analysis of aggregate particles from orthogonal projections, Transp. Res. Rec. (1996). https://doi.org/10.3141/1526-12.

[44] J. Zheng, R.D. Hryciw, Traditional soil particle sphericity, roundness and surface roughness by computational geometry, Geotechnique 65 (2015). https://doi.org/10.1680/geot.14.P.192.

[45] A. Mahmood, T. Akram, H. Chen, S. Chen, On the Evolution of Additive Manufacturing (3D/4D Printing) Technologies: Materials, Applications, and Challenges, Polymers (Basel). 14 (2022). https://doi.org/10.3390/polym14214698.

[46] P. Lakkala, S.R. Munnangi, S. Bandari, M. Repka, Additive manufacturing technologies with emphasis on stereolithography 3D printing in pharmaceutical and medical applications: A review, Int. J. Pharm. X 5 (2023). https://doi.org/10.1016/j.ijpx.2023.100159.

[47] T.D. Ngo, A. Kashani, G. Imbalzano, K.T.Q. Nguyen, D. Hui, Additive manufacturing (3D printing): A review of materials, methods, applications and challenges, Compos. B Eng. 143 (2018). https://doi.org/10.1016/j.compositesb.2018.02.012.

[48] J.A. Fleischmann, Micromechanical Exploration of the Lade–Duncan Yield Surface by the Discrete Element Method, Geotechnical and Geological Engineering 38 (2020). https://doi.org/10.1007/s10706-020-01374-7.

[49] H. Cheng, T. Shuku, K. Thoeni, H. Yamamoto, Probabilistic calibration of discrete element simulations using the sequential quasi-Monte Carlo filter, Granul. Matter 20 (2018). https://doi.org/10.1007/s10035-017-0781-y.

[50] W. Chen, A. Roberts, K. Williams, J. Miller, J. Plinke, On uniaxial compression and Jenike direct shear testings of cohesive iron ore materials, Powder Technol. 312 (2017). https://doi.org/10.1016/j.powtec.2017.02.037.

[51] A.S. CAGLI, B.N. DEVECI, C.H. OKUTAN, D.A.A. SIRKECI, E.Y. TEOMAN, 044 Flow property measurement using the Jenike shear cell for 7 different bulk solids, Proceedings of European Congress of Chemical Engineering (ECCE-6) (2007).

[52] R.J. Berry, M.S.A. Bradley, Investigation of the effect of test procedure factors on the failure loci and derived failure functions obtained from annular shear cells, Powder Technol. 174 (2007). https://doi.org/10.1016/j.powtec.2006.10.023.

[53] H. Kalman, Effect of moisture content on flowability: Angle of repose, tilting angle, and Hausner ratio, Powder Technol. 393 (2021). https://doi.org/10.1016/j.powtec.2021.08.010.

[54] F. Elekes, E.J.R. Parteli, An expression for the angle of repose of dry cohesive granular materials on Earth and in planetary environments, Proc. Natl. Acad. Sci. U. S. A. 118 (2021). https://doi.org/10.1073/pnas.2107965118.

[55] D. Müller, E. Fimbinger, C. Brand, Algorithm for the determination of the angle of repose in bulk material analysis, Powder Technol. 383 (2021). https://doi.org/10.1016/j.powtec.2021.01.010.

[56] H. Kalman, Quantification of mechanisms governing the angle of repose, angle of tilting, and Hausner ratio to estimate the flowability of particulate materials, Powder Technol. 382 (2021). https://doi.org/10.1016/j.powtec.2021.01.012.

[57] D. Schulze, Powders and Bulk Solids: Behavior, Characterization, Storage and Flow, Second Edition, 2021. https://doi.org/10.1007/978-3-030-76720-4.

[58] Y. Shen, P. Sun, Z. Zhang, Y. Wang, B. Zheng, A tube heat transfer prediction model considering static friction coefficient of dense particle flow, Int. J. Heat Mass Transf. 205 (2023). https://doi.org/10.1016/j.ijheatmasstransfer.2023.123902.

[59] S.K. Wilkinson, S.A. Turnbull, Z. Yan, E.H. Stitt, M. Marigo, A parametric evaluation of powder flowability using a Freeman rheometer through statistical and sensitivity analysis: A discrete element method (DEM) study, Comput. Chem. Eng. 97 (2017). https://doi.org/10.1016/j.compchemeng.2016.11.034.

[60] N. Nuño, R. Groppetti, N. Senin, Static coefficient of friction between stainless steel and PMMA used in cemented hip and knee implants, Clinical Biomechanics 21 (2006). https://doi.org/10.1016/j.clinbiomech.2006.05.008.

[61] M.A. Maroof, A. Mahboubi, A. Noorzad, Y. Safi, A new approach to particle shape classification of granular materials, Transportation Geotechnics 22 (2020). https://doi.org/10.1016/j.trgeo.2019.100296.

[62] J. Zheng, Z. Zhang, C. Li, Z. Li, L. Gao, Laboratory-on-a-smartphone for estimating angularity of granular soils, Acta Geotech. 17 (2022). https://doi.org/10.1007/s11440-021-01259-w.

[63] M. Fan, D. Su, N. Zhang, G. Cai, X. Chen, Optimizing parameter combinations for clump models enabled by the bubble packing algorithm: Insights from geometrical and morphological approximation of typical geotechnical particles, Comput. Geotech. 180 (2025) 107061. https://doi.org/https://doi.org/10.1016/j.compgeo.2025.107061.

APPENDIX

Table A1: Relative shape changes per simplification level

Number of faces	sphericity change(%)	convexity change(%)	roundness change (%)	average absolute shape change (%)
40	-20.34	-19.92	-93.50	44.59
60	-16.64	-15.95	-76.40	36.33
80	-11.83	-9.75	-65.33	28.97
100	-8.85	-10.16	-59.56	26.19
150	-5.25	-6.78	-51.09	21.04
200	-4.83	-7.00	-44.11	18.65
300	-2.40	-2.62	-43.25	16.09
400	-1.40	-1.69	-14.05	5.71
1000	0.53	-0.43	-8.79	2.90
4000	0.62	0.35	-3.00	0.68
10000	0.36	0.21	-0.56	0.00
40000	0.09	0.05	1.14	0.43
400000	0.00	0.00	0.00	0.00

Table A2: Mean, uncertainty (95% confidence level), and relative uncertainty of AoR at different simplification levels

	400000 faces	400 faces	100 faces	40 faces
Mean AoR	48.9°	41.7°	46.0°	44.4°
Uncertainty (95% confidence level)	+/- 2.1°	+/- 2.9°	+/- 2.5°	+/- 1.4°
Relative Uncertainty	+/- 4.3 %	+/- 6.2 %	+/- 5.3 %	+/- 3.1%

Table A3: Mean, uncertainty (95% confidence level), and relative uncertainty of μ_s (single-particle, random placement) at different simplification levels

	400000 faces	400 faces	100 faces	40 faces
Mean μ_s	0.48	0.47	0.46	0.46
Uncertainty (95% confidence level)	+/- 0.06	+/- 0.04	+/- 0.03	+/- 0.03
Relative Uncertainty	12.50%	8.51%	6.52%	6.52%

Table A4: Mean, uncertainty (95% confidence level), and relative uncertainty of μ_s *(single-particle, controlled placement) at different simplification levels*

	400000 faces	**400 faces**	**100 faces**	**40 faces**
Mean μ_s	0.52	0.51	0.48	0.47
Uncertainty (95% confidence level)	+/- 0.04	+/- 0.04	+/- 0.02	+/- 0.02
Relative Uncertainty	+/- 7.69%	+/- 7.84%	+/- 4.17%	+/- 4.26%

Table A5: Mean, uncertainty (95% confidence level), and relative uncertainty of μ_s *(bulk level) at different simplification levels*

	400000 faces	**400 faces**	**100 faces**	**40 faces**
Mean μ_s	0.55	0.54	0.52	0.49
Uncertainty (95%)	+/- 0.03	+/- 0.03	+/- 0.03	+/- 0.03
Relative Uncertainty	+/- 5.45%	+/- 5.56%	+/- 5.77%	+/- 6.12%

Table A6: Mean, uncertainty (95% confidence level), and relative uncertainty of HR at different simplification levels

	400000 faces	**400 faces**	**100 faces**	**40 faces**
Mean HR	1.45	1.42	1.36	1.32
Uncertainty (95%)	+/- 0.03	+/- 0.03	+/- 0.03	+/- 0.03
Relative Uncertainty	+/- 2.07%	+/- 2.11%	+/- 2.21%	+/- 2.27%

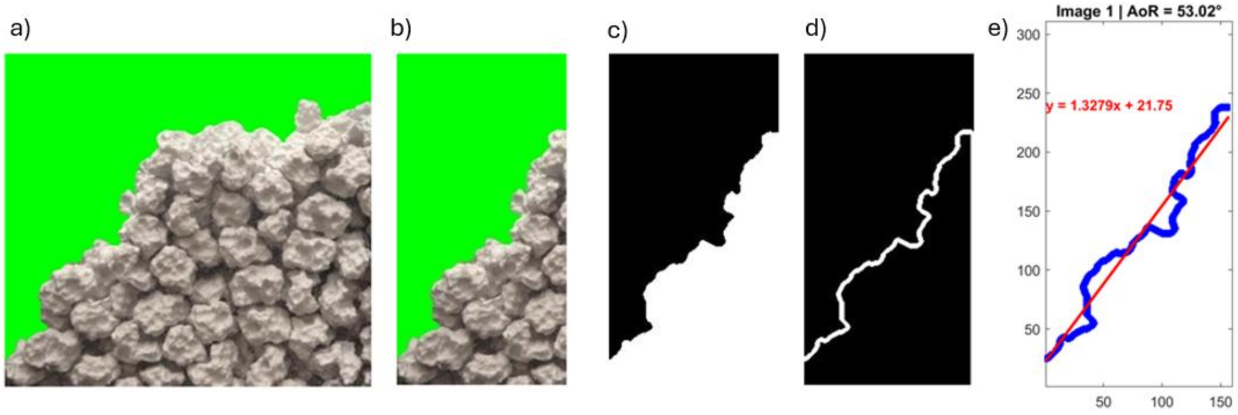

Figure A1: Image-processing steps: a) full image with edited green background; b) cropped region of interest; c) binary image after colour-based segmentation; d) extracted edge; e) extracted edge points (blue) and linear fitted line (red), to calculate AoR

Appendix B: Matlab Code for Shape Descriptors

```
clc; clear all; close all;

% Define shape files

shapeFiles = ["S1_1 (1).stl", "1x_simplification_40000faces.stl",
"1x_simplification_10000faces.stl", "1x_simplification_4000faces.stl",
"1x_simplification_1000faces.stl", "1x_simplification_400faces.stl"
,"1x_simplification_300faces.stl" , "1x_simplification_200faces.stl",
"1x_simplification_150faces.stl" ,
"1x_simplification_100faces.stl","1x_simplification_80faces.stl" ,
"1x_simplification_60faces.stl" ,"1x_simplification_40faces.stl"];

id_array = 1:numel(shapeFiles);

% Define parameters to store
parameters = ["b/a"; "c/b"; "Sphericity"; "SVR"; "Convexity";
"Compactness"; "id"];
shapeMatrix = zeros(numel(parameters), numel(shapeFiles));

% Loop through each shape
for i = 1:numel(shapeFiles)
    % Read the STL file
    [vertices, faces, ~] = stlread(char(shapeFiles{i}));

    % Align the shape based on the bounding box
    centeredVertices = vertices - mean(vertices);
    [coeff, ~, latent] = pca(centeredVertices);

    % Identify smallest, largest, and intermediate dimensions
    [~, minIndex] = min(latent);
    [~, maxIndex] = max(latent);
    indices = 1:3;
    midIndex = setdiff(indices, [minIndex, maxIndex]);

    smallest_value = latent(minIndex);
    largest_value = latent(maxIndex);
    intermediate_value = latent(midIndex);


    % Compute b/a and c/b
    shapeMatrix(1, i) = intermediate_value / largest_value; % b/a
    shapeMatrix(2, i) = smallest_value / intermediate_value; % c/b

    % Compute volume and surface area
```

```
    [Volume, SurfaceArea] = compute_volume_area(faces, vertices);

    % Compute Sphericity
    Sphericity = (pi^(1/3) * (6 * Volume)^(2/3)) / SurfaceArea;
    shapeMatrix(3, i) = Sphericity;

    % Compute SVR (Surface-to-Volume Ratio)
    SVR = SurfaceArea / Volume;
    shapeMatrix(4, i) = SVR;

    % Compute Convexity (V / V_convex_hull)
    [~, ConvexHullVolume] = convhull(vertices);
    Convexity = Volume / ConvexHullVolume;
    shapeMatrix(5, i) = Convexity;

    % Compute Compactness (V / a^3)
    Compactness = Volume / (largest_value^3);
    shapeMatrix(6, i) = Compactness;

    % Store particle ID
    shapeMatrix(7, i) = id_array(i);

    % Display results
    fprintf('Particle: %s | b/a: %.3f | c/b: %.3f | Sphericity: %.5f |
SVR: %.5f | Convexity: %.5f | Compactness: %.5f\n', ...
        shapeFiles(i), shapeMatrix(1, i), shapeMatrix(2, i),
Sphericity, SVR, Convexity, Compactness);
end

% Function to compute volume and surface area from STL mesh
function [Volume, SurfaceArea] = compute_volume_area(faces, vertices)
    Volume = 0;
    SurfaceArea = 0;
    for i = 1:size(faces,1)
        v1 = vertices(faces(i,1),:);
        v2 = vertices(faces(i,2),:);
        v3 = vertices(faces(i,3),:);

        % Compute triangle area using cross product
        TriangleArea = 0.5 * norm(cross(v2 - v1, v3 - v1));
        SurfaceArea = SurfaceArea + TriangleArea;

        % Compute volume using tetrahedral decomposition
        TetraVolume = dot(v1, cross(v2, v3)) / 6;
        Volume = Volume + TetraVolume;
    end
    Volume = abs(Volume); % Ensure positive volume
end

% Function to read STL file
function [vertices, faces, normals] = stlread(fileName)
```

```
    [fid, msg] = fopen(fileName, 'r');
    if fid == -1
        error('stlread: cannot open file, %s', msg);
    end

    fseek(fid, 80, 'bof'); % Skip header
    numFaces = fread(fid, 1, 'uint32'); % Read number of triangles

    faces = zeros(numFaces, 3);
    vertices = zeros(numFaces*3, 3);
    normals = zeros(numFaces, 3);

    for i = 1:numFaces
        normals(i,:) = fread(fid, 3, 'float32');
        vertices(3*i-2,:) = fread(fid, 3, 'float32');
        vertices(3*i-1,:) = fread(fid, 3, 'float32');
        vertices(3*i,:) = fread(fid, 3, 'float32');
        faces(i,:) = [3*i-2, 3*i-1, 3*i];
        fread(fid, 1, 'uint16'); % Attribute byte count
    end

    fclose(fid);

    % Remove duplicate vertices
    [vertices, ~, indexMap] = unique(vertices, 'rows');
    faces = indexMap(faces);
end
```

Appendix C: MATLAB Code for Roundness

```
%%%%%%%%%%%%%%%%%%%%%%%%%%%%%%%%%%%%
% This code was developed by
%       Junxing Zheng  (Sep. 2014)
%       University of Michigan, Ann Arbor
%       junxing@umich.edu
%
%  The detailed description of code is in the paper:
%  Zheng and Hryciw (2015)
%
%   If you use this code in your publication, please cite:
%   Zheng, J., and Hryciw, R.D. (2015). “Traditional Soil Particle
Sphericity,
%   Roundness and Surface Roughness by Computational Geometry”,
%   Géotechnique, Vol. 65, No. 6, 494-506, DOI:10.1680/geot./14-P-192.
%%%%%%%%%%%%%%%%%%%%%%%%%%%%%%%%%%%%

clear all
close all
addpath(genpath('main_Funs'))


%% parameter settings
tol =0.3;     % forming straight lines to the bounndary
factor = 0.98; % fitting small circles
span = 0.07; % nonparametric fitting, if the boundary of particle is
very rough, try a larger value;

%% main function
img=imread('40faces_example.jpg');
level = graythresh(img);
im = im2bw(img,level);
BW =~im;
lbl = bwlabel(BW, 4);


dist_map=bwdist(~BW);
sz=size(BW);
cc = bwconncomp(BW, 8);
particles = discrete_boundary(cc);
particles = nonparametric_fitting(particles, span);


figure
imshow(img);
```

```
hold on
result = [];

for k = 1:cc.NumObjects
    obj = cc.PixelIdxList{k};
    [R, RInd]=max(dist_map(obj));
    [cy, cx]=ind2sub(sz, obj(RInd));
    boundary_points = particles.objects(k).cartesian;
    X = boundary_points(:, 1);
    Y = boundary_points(:, 2);

    % plot largest circle
    theta = [linspace(0,2*pi, 100)];
    plot(cos(theta)*R+cx,sin(theta)*R+cy,'color','r','LineWidth', 2);

    % segment the boundary of particels
    seglist = segment_boundary(X, Y, tol, 0);

    % concave and convex detection
    [concave, convex] = concave_convex(seglist, [cx, cy], 0);

    % fit small circles
    [z, r] = compute_corner_circles(sz,obj , convex, boundary_points,
R, factor, 3);


    for ee = 1:length(r)
        plot(z(ee, 1),z(ee,2),...   % plot the center of circles
            z(ee, 1)  + r(ee)  * cos(theta),...
            z(ee,2)  + r(ee) * sin(theta), 'g','LineWidth', 2);


    end

    Roundness = mean(r)/R;
    if Roundness > 1
        Roundness =1;
    end


    text(cx, cy, num2str(k), 'Color', 'b' )



 %% Sphericity computation
        [~,rcum] = min_circum_circle(X,Y);
        sphericity1 = particles.objects(k).area/(pi*rcum^2);  % area
sphericity
        sphericity2 = sqrt( particles.objects(k).area/ pi)/rcum;   %
diameter sphericity
        sphericity3 = R/rcum;   % circle ratio sphericity
```

```
        sphericity4 =
2*sqrt(pi*particles.objects(k).area)/particles.objects(k).perimeter; %
perimeter sphericity
        sphericity5 =
particles.objects(k).d1d2(2)/particles.objects(k).d1d2(1); % width to
length ratio spehricity

 %% summary of results
        result = [result; Roundness, sphericity1, sphericity2,
sphericity3, sphericity4, sphericity5];

end
```

Appendix D: Particles at various Simplification Levels

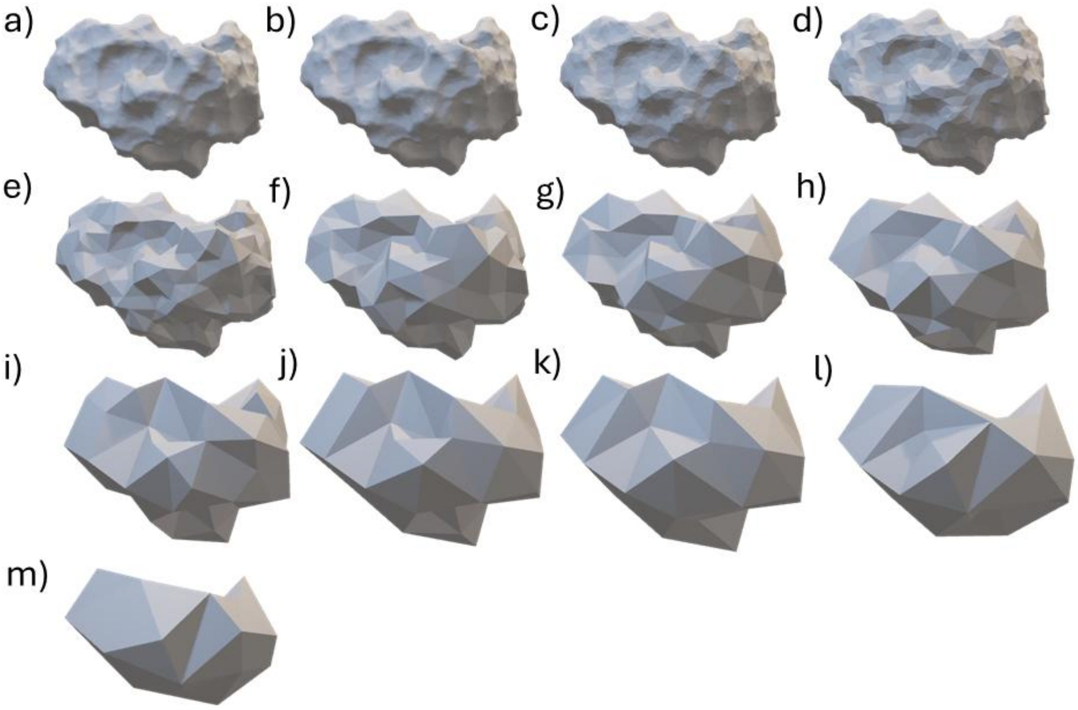

Figure D. 1: Simplification levels: a) 400,000 faces; b) 40,000 faces; c) 10,000 faces; d) 4,000 faces; e)1,000 faces; f) 400 faces; g) 300 faces; h) 200 faces; i) 150 faces; j) 100 faces; k) 80 faces; l) 60 faces; m) 40 faces (image sizes are not to scale)

Appendix E: Shape Descriptor values and Volume at various Simplification Levels

Table E. 1: Volume and Shape Descriptor Values

Number of Faces	Roundness	Volume (mm^3)	Sphericity	Convexity
40	0.27723	3675.01	0.78777	0.79635
60	0.25273	4124.74	0.76357	0.77003
80	0.23687	4184.6	0.73208	0.72883
100	0.22860	4243.65	0.71255	0.73153
150	0.21647	4374.32	0.68901	0.7091
200	0.20647	4480.61	0.68626	0.71054
300	0.20523	4547.72	0.67033	0.68151
400	0.16340	4547.72	0.66377	0.67532
1000	0.15587	4561.22	0.65114	0.66693
4000	0.14757	4544.8	0.65057	0.66174
10000	0.14407	4542.44	0.65229	0.66268
40000	0.14163	4540.98	0.65401	0.66377
400000	0.14327	4540.55	0.65462	0.66408

Appendix F: Weighted Particles per Sample

Figure F. 1: 400,000-face particles weighted

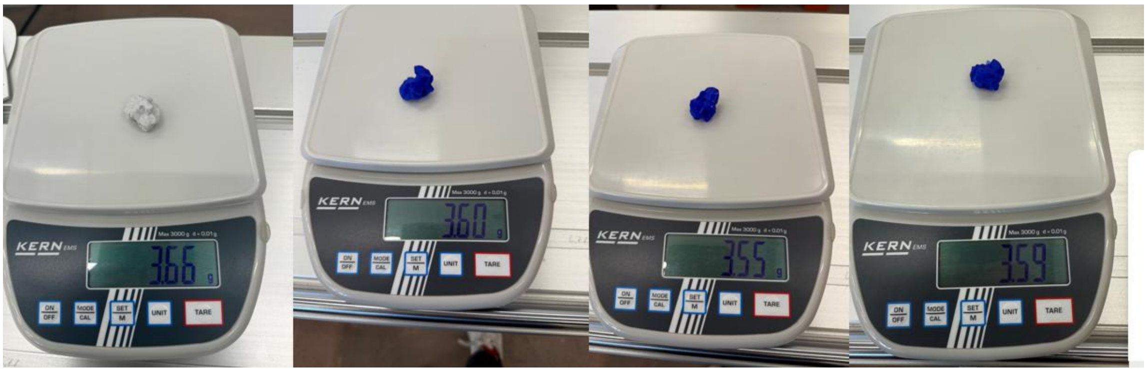

Figure F. 2: 400-face particles weighted

Figure F. 3: 100-face particles weighted

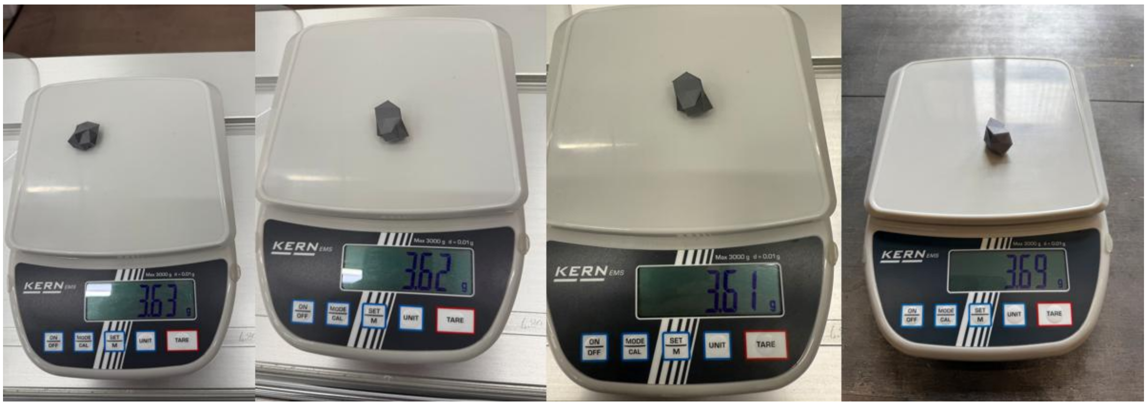

Figure F. 4: 40-face particles weighted

Appendix G: Printing Time (single particle & bulk level) of the 400-, 100-, and 40-Face Model

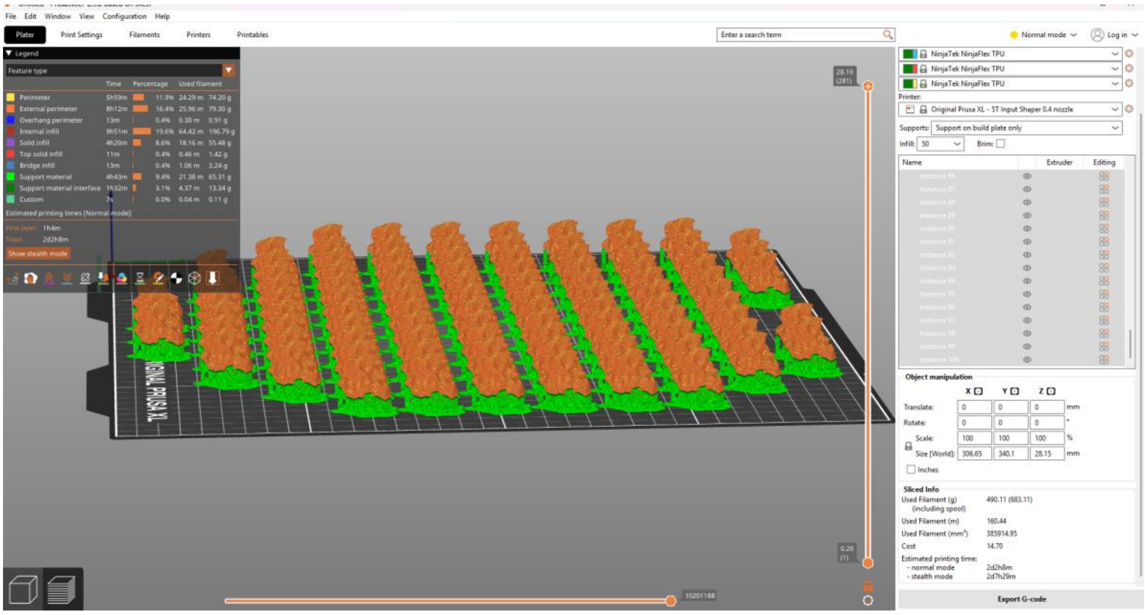

	Time	Percentage	Used filament	
🟨 Perimeter	5h59m	11.9%	24.29 m	74.20 g
🟧 External perimeter	8h12m	16.4%	25.96 m	79.30 g
🟦 Overhang perimeter	13m	0.4%	0.30 m	0.91 g
🟥 Internal infill	9h51m	19.6%	64.42 m	196.79 g
🟪 Solid infill	4h20m	8.6%	18.16 m	55.48 g
🟥 Top solid infill	11m	0.4%	0.46 m	1.42 g
🟦 Bridge infill	13m	0.4%	1.06 m	3.24 g
🟩 Support material	4h43m	9.4%	21.38 m	65.31 g
🟩 Support material interface	1h32m	3.1%	4.37 m	13.34 g
🟩 Custom	7s	0.0%	0.04 m	0.11 g

Estimated printing times [Normal mode]:

First layer: 1h4m

Total: 2d2h8m

NinjaTek NinjaFlex TPU

NinjaTek NinjaFlex TPU

NinjaTek NinjaFlex TPU

Printer:

Original Prusa XL - 5T Input Shaper 0.4 nozzle

Supports: Support on build plate only

Infill: 50 Brim: ☐

Object manipulation

	X	Y	Z	
Translate:	0	0	0	mm
Rotate:	0	0	0	°
Scale:	100	100	100	%
Size [World]:	306.65	340.1	28.15	mm

☐ Inches

Sliced Info

Used Filament (g) (including spool)	490.11 (683.11)
Used Filament (m)	160.44
Used Filament (mm³)	385914.95
Cost	14.70
Estimated printing time:	
- normal mode	2d2h8m
- stealth mode	2d7h29m

Figure G. 1: Estimated printing time for 100 particles of the 400-face model

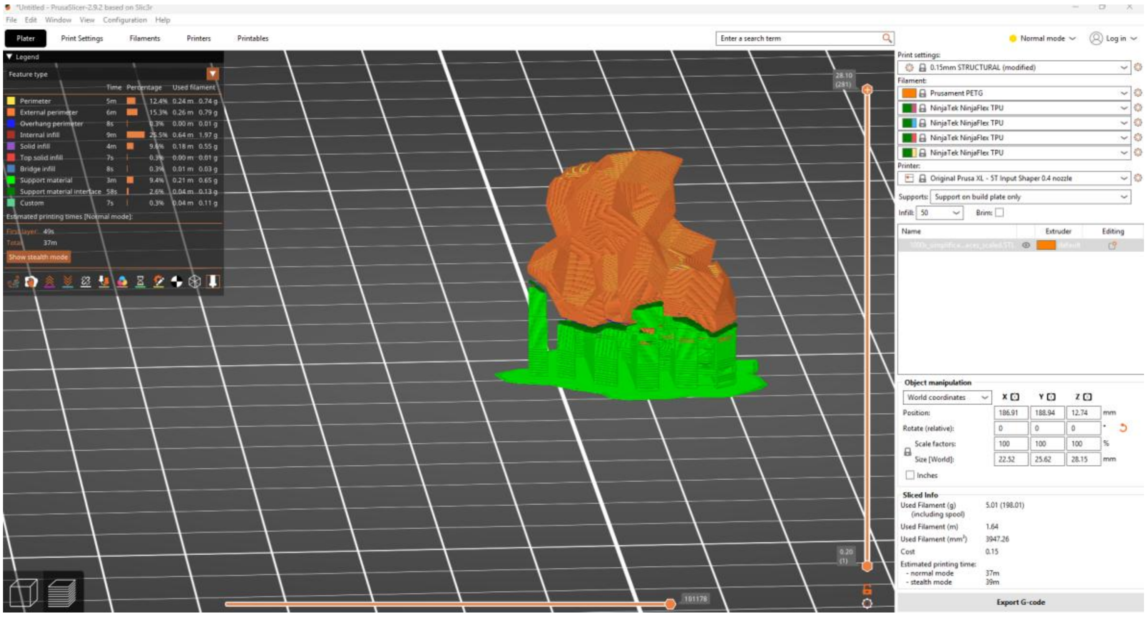

	Time	Percentage	Used filament	
🟨 Perimeter	5m	12.4%	0.24 m	0.74 g
🟧 External perimeter	6m	15.3%	0.26 m	0.79 g
🟦 Overhang perimeter	8s	0.3%	0.00 m	0.01 g
🟥 Internal infill	9m	25.5%	0.64 m	1.97 g
🟪 Solid infill	4m	9.6%	0.18 m	0.55 g
🟥 Top solid infill	7s	0.3%	0.00 m	0.01 g
🟦 Bridge infill	8s	0.3%	0.01 m	0.03 g
🟩 Support material	3m	9.4%	0.21 m	0.65 g
🟩 Support material interface	58s	2.6%	0.04 m	0.13 g
🟩 Custom	7s	0.3%	0.04 m	0.11 g

Estimated printing times [Normal mode]:

First layer: 49s

Total: 37m

Print settings:

0.15mm STRUCTURAL (modified)

Filament:

Prusament PETG

NinjaTek NinjaFlex TPU

NinjaTek NinjaFlex TPU

NinjaTek NinjaFlex TPU

NinjaTek NinjaFlex TPU

Printer:

Original Prusa XL - 5T Input Shaper 0.4 nozzle

Supports: Support on build plate only

Infill: 50 Brim: ☐

Object manipulation

World coordinates	X	Y	Z	
Position:	186.91	188.94	12.74	mm
Rotate (relative):	0	0	0	°
Scale factors:	100	100	100	%
Size [World]:	22.52	25.62	28.15	mm

☐ Inches

Sliced Info

Used Filament (g) (including spool)	5.01 (198.01)
Used Filament (m)	1.64
Used Filament (mm³)	3947.26
Cost	0.15
Estimated printing time:	
- normal mode	37m
- stealth mode	39m

Figure G. 2: Estimated printing time for a single particle of the 400-face model

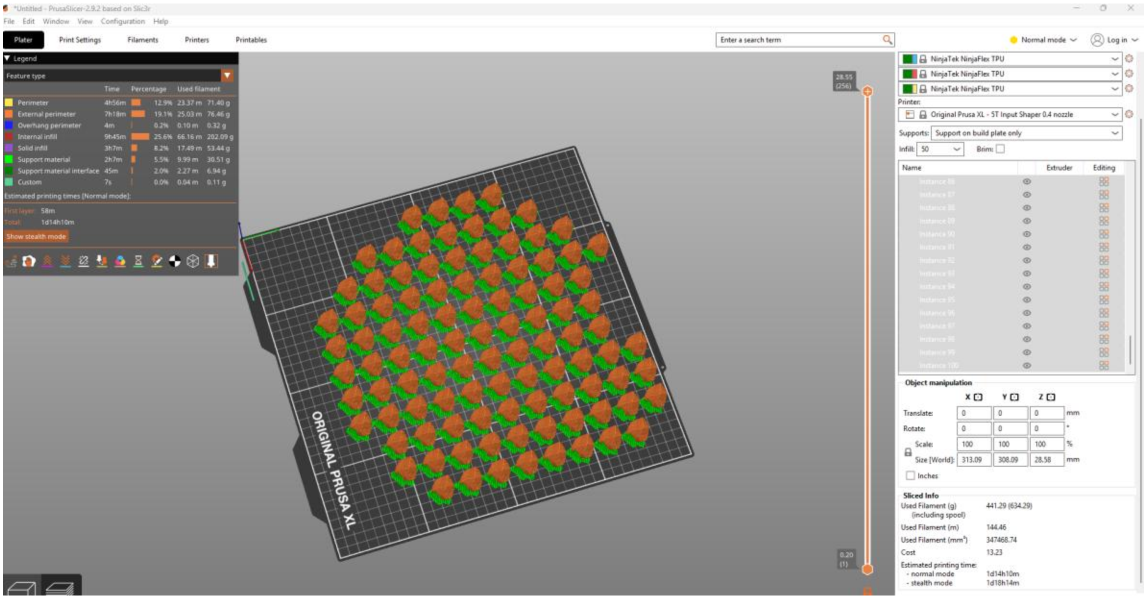

Feature type

	Time	Percentage	Used filament	
Perimeter	4h56m	12.9%	23.37 m	71.40 g
External perimeter	7h18m	19.1%	25.03 m	76.46 g
Overhang perimeter	4m	0.2%	0.10 m	0.32 g
Internal infill	9h45m	25.6%	66.16 m	202.09 g
Solid infill	3h7m	8.2%	17.49 m	53.44 g
Support material	2h7m	5.5%	9.99 m	30.51 g
Support material interface	45m	2.0%	2.27 m	6.94 g
Custom	7s	0.0%	0.04 m	0.11 g

Estimated printing times [Normal mode]:
First layer: 58m
Total: 1d14h10m

NinjaTek NinjaFlex TPU
NinjaTek NinjaFlex TPU
NinjaTek NinjaFlex TPU
Printer: Original Prusa XL - 5T Input Shaper 0.4 nozzle
Supports: Support on build plate only
Infill: 50
Brim: ☐

Object manipulation

	X	Y	Z	
Translate:	0	0	0	mm
Rotate:	0	0	0	°
Scale:	100	100	100	%
Size [World]:	313.09	308.09	28.58	mm

☐ Inches

Sliced Info

Used Filament (g) (including spool)	441.29 (634.29)
Used Filament (m)	144.46
Used Filament (mm³)	347468.74
Cost	13.23
Estimated printing time: - normal mode - stealth mode	 1d14h10m 1d18h14m

Figure G. 3: Estimated printing time for 100 particles of the 100-face model

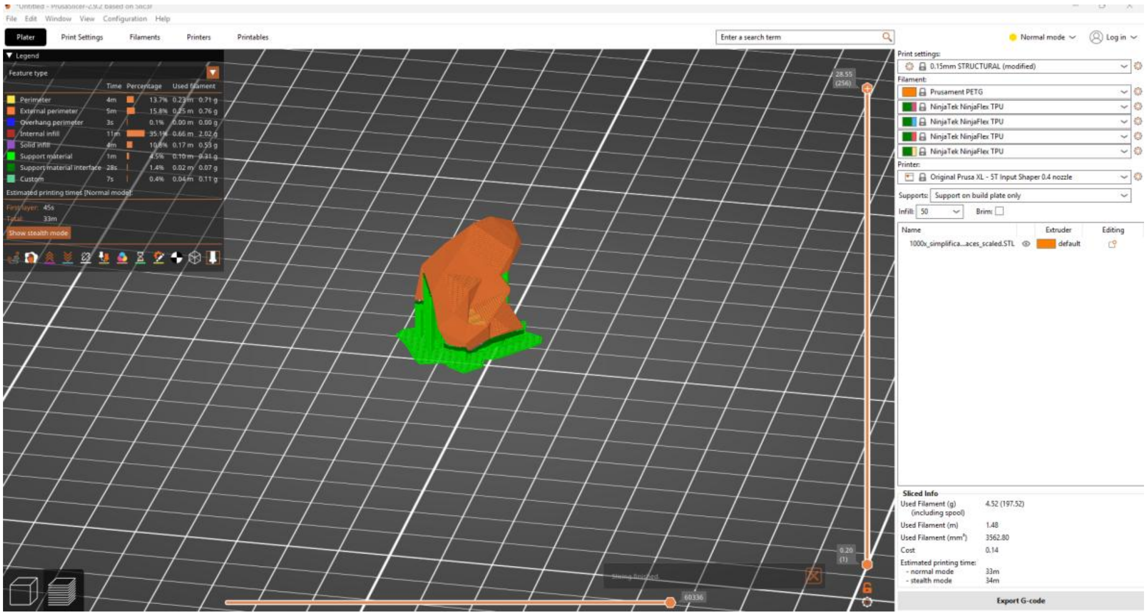

Feature type

	Time	Percentage	Used filament	
Perimeter	4m	13.7%	0.23 m	0.71 g
External perimeter	5m	15.8%	0.25 m	0.76 g
Overhang perimeter	3s	0.1%	0.00 m	0.00 g
Internal infill	11m	35.1%	0.66 m	2.02 g
Solid infill	4m	10.8%	0.17 m	0.53 g
Support material	1m	4.5%	0.10 m	0.31 g
Support material interface	28s	1.4%	0.02 m	0.07 g
Custom	7s	0.4%	0.04 m	0.11 g

Estimated printing times [Normal mode]:
First layer: 45s
Total: 33m

Print settings: 0.15mm STRUCTURAL (modified)
Filament:
Prusament PETG
NinjaTek NinjaFlex TPU
NinjaTek NinjaFlex TPU
NinjaTek NinjaFlex TPU
NinjaTek NinjaFlex TPU
Printer: Original Prusa XL - 5T Input Shaper 0.4 nozzle
Supports: Support on build plate only
Infill: 50
Brim: ☐

Name	Extruder	Editing
1000x_simplifica...aces_scaled.STL	default	

Sliced Info

Used Filament (g) (including spool)	4.52 (197.52)
Used Filament (m)	1.48
Used Filament (mm³)	3562.80
Cost	0.14
Estimated printing time: - normal mode - stealth mode	 33m 34m

Figure G. 4: Estimated printing time for a single particle of the 100-face model

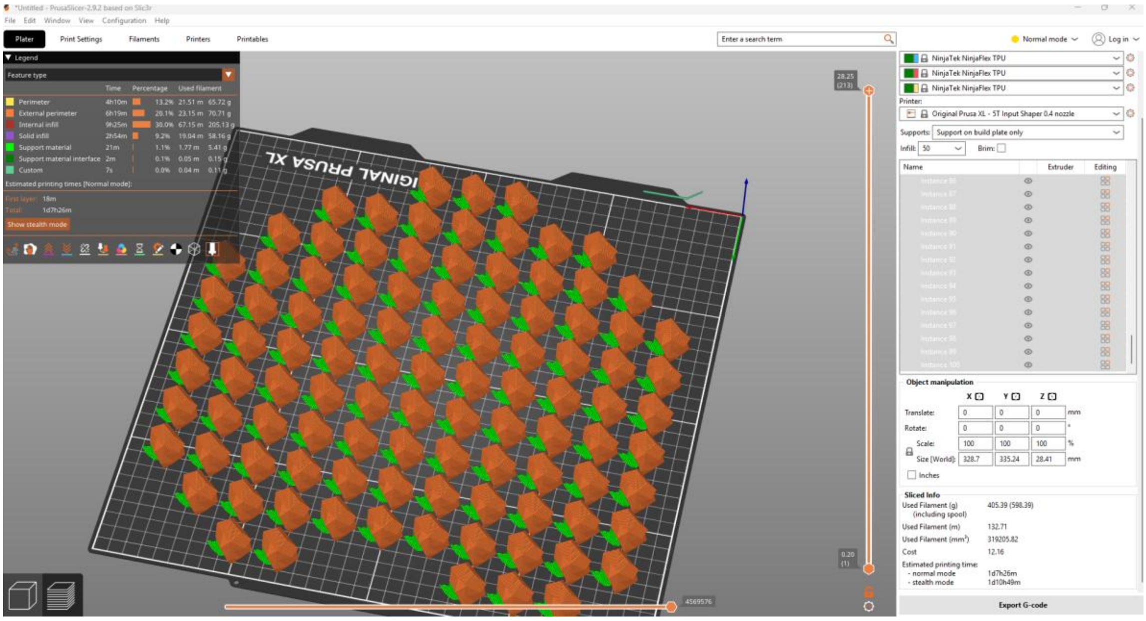

	Time	Percentage	Used filament	
🟨 Perimeter	4h10m	13.2%	21.51 m	65.72 g
🟧 External perimeter	6h19m	20.1%	23.15 m	70.71 g
🟥 Internal infill	9h25m	30.0%	67.15 m	205.13 g
🟪 Solid infill	2h54m	9.2%	19.04 m	58.16 g
🟩 Support material	21m	1.1%	1.77 m	5.41 g
🟩 Support material interface	2m	0.1%	0.05 m	0.15 g
🟩 Custom	7s	0.0%	0.04 m	0.11 g

Estimated printing times [Normal mode]:
First layer: 18m
Total: 1d7h26m

NinjaTek NinjaFlex TPU
NinjaTek NinjaFlex TPU
NinjaTek NinjaFlex TPU
Printer:
Original Prusa XL - 5T Input Shaper 0.4 nozzle
Supports: Support on build plate only
Infill: 50
Brim: ☐

Object manipulation

	X	Y	Z	
Translate:	0	0	0	mm
Rotate:	0	0	0	°
Scale:	100	100	100	%
Size [World]:	328.7	335.24	28.41	mm

☐ Inches

Sliced Info

Used Filament (g) (including spool)	405.39 (598.39)
Used Filament (m)	132.71
Used Filament (mm^3)	319205.82
Cost	12.16
Estimated printing time: - normal mode - stealth mode	 1d7h26m 1d10h49m

Figure G. 5: Estimated printing time for 100 particles of the 40-face model

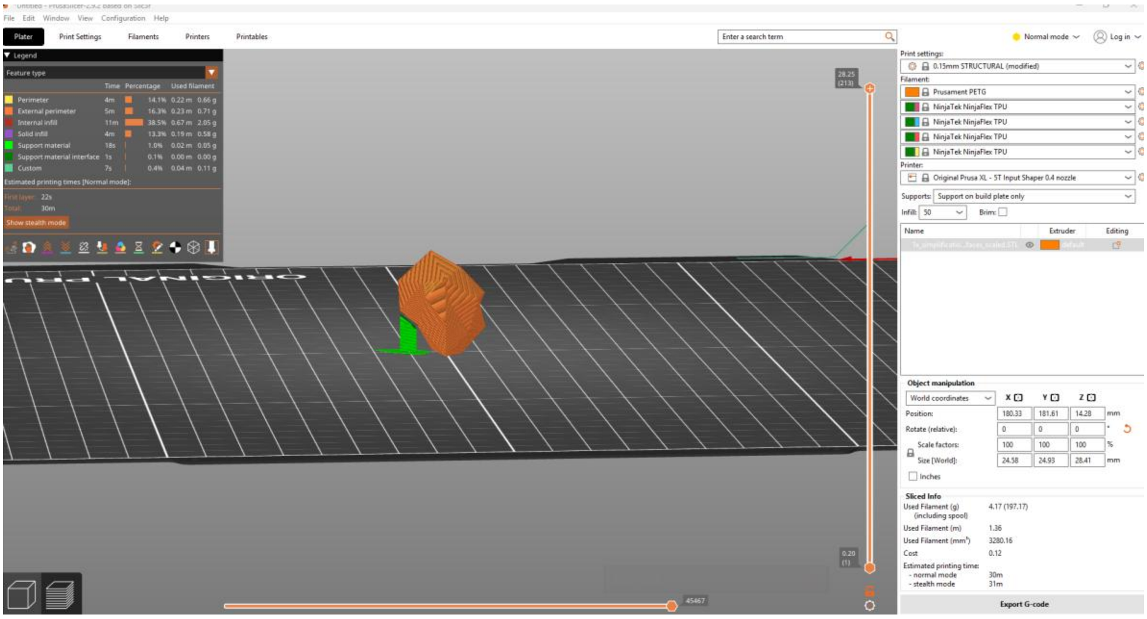

	Time	Percentage	Used filament	
🟨 Perimeter	4m	14.1%	0.22 m	0.66 g
🟧 External perimeter	5m	16.3%	0.23 m	0.71 g
🟥 Internal infill	11m	38.5%	0.67 m	2.05 g
🟪 Solid infill	4m	13.3%	0.19 m	0.58 g
🟩 Support material	18s	1.0%	0.02 m	0.05 g
🟩 Support material interface	1s	0.1%	0.00 m	0.00 g
🟩 Custom	7s	0.4%	0.04 m	0.11 g

Estimated printing times [Normal mode]:
First layer: 22s
Total: 30m

Print settings:
0.15mm STRUCTURAL (modified)
Filament:
Prusament PETG
NinjaTek NinjaFlex TPU
NinjaTek NinjaFlex TPU
NinjaTek NinjaFlex TPU
NinjaTek NinjaFlex TPU
Printer:
Original Prusa XL - 5T Input Shaper 0.4 nozzle
Supports: Support on build plate only
Infill: 50
Brim: ☐

Object manipulation

World coordinates	X	Y	Z	
Position:	180.33	181.61	14.28	mm
Rotate (relative):	0	0	0	°
Scale factors:	100	100	100	%
Size [World]:	24.58	24.93	28.41	mm

☐ Inches

Sliced Info

Used Filament (g) (including spool)	4.17 (197.17)
Used Filament (m)	1.36
Used Filament (mm^3)	3280.16
Cost	0.12
Estimated printing time: - normal mode - stealth mode	 30m 31m

Figure G. 6: Estimated printing time for a single particle of the 40-face model

Appendix H: MATLAB code for the Angle of Repose

```
clear
close
clc
%%%%%%%%%%%%%%%%%%%%%%%%%%%%%%%%%%%%
%%%%% Reading multiple images %%%%%%
% Read image1.jpg through imageK.jpg.  Files are in the current directory.
% Use fullfile() if you need to prepend some other folder to the base file name.
% Adapt to use which ever cases you need.
num_Image = input("Enter the number of images:");
mkdir('Outputs')
fileID = fopen('AoR.txt','w');
fprintf(fileID, 'ID\t');
fprintf(fileID, 'Angle of repose\n');
for k = 1 : num_Image
      % OPTION 2: Create an image filename, and read it in to a variable called imageData.
      jpgFileName = strcat('Large_', num2str(k), '.jpeg');
      if isfile(jpgFileName)
            imageData = imread(jpgFileName);
        %%%%%%%%%%%%%%%%%%%%%%%%%%%%%%%%%%%%
        imageData = imrotate(imageData,180);
        imageData = flip(imageData,2);
        %%%%% Colour segmentation using L*a*b* space %%%%%%
        [Image_BW,Image_M] = Mask_large(imageData);
%         Image_BW = medfilt2(Image_BW',[2 2]);
        filt = fspecial('average',[2 2]);
        Image_BW = imfilter(Image_BW,filt);
        imshow(Image_BW);
        % Heap = imcrop(Heap);
        %%%%%%%%%%%%%%%%%%%%%%%%%%%%%%%%%%%%
        Image_Edge = edge(Image_BW);
        thickness = 2;
        se = strel('disk', thickness);
        Image_Edge = imdilate(Image_Edge, se);
        imshow(Image_Edge);
        [r,c] = find(Image_Edge==1);
        plot(c,r,'.');
        % P_Edge(k) = gcf;
        % exportgraphics(P_Edge(k),'Edge.png','Resolution',300);
        %%%%%%%%%%%%%%%%%%%%%%%%%%%%%%%%%%%
        %enter the a in y=ax+b equation manualy
        %to do: make this automatic
```

```
        LFit = polyfit(c,r,1);
        a = LFit(1);
        AoR(k) = rad2deg(atan(abs(a)));
        fprintf(fileID, '%d\t', k);
        fprintf(fileID, '%.2f\n', AoR(k));
        %%%%% Save desired outputs %%%%%
        Image_Save = imrotate(Image_BW,180);
        Image_Save = flip(Image_Save,2);

        Image_Edge_Out = imrotate(Image_Edge,180);
        Image_Edge_Out = flip(Image_Edge_Out,2);
        % create the filename with numbering pattern
        filename1 = sprintf('P_BW_%03d.jpg', k);
        filename2 = sprintf('P_Edge_%03d.jpg', k);
        % save the image to the new subfolder
        imwrite(Image_Save, fullfile('Outputs', filename1));
        imwrite(Image_Edge_Out, fullfile('Outputs', filename2));
    else
            fprintf('File %s does not exist.\n', jpgFileName);
    end
end
fprintf(fileID, '**************************************\n');
AoR_STD = std(AoR);
AoR_Avg = mean(AoR);
fprintf(fileID, 'The average AoR is: %.2f\n', AoR_Avg);
%%%%% Insert the t value from the table %%%%%
t_value = 2.776;
AoR_95_CI = (t_value*AoR_STD)/sqrt(num_Image);
fprintf(fileID, 'The 95 confidence interval is: %.2f\n', AoR_95_CI);
%%%%%%%%%%%%% Close writing the output %%%%%%%%%%%%%
fclose(fileID);
```

Appendix I: T-table

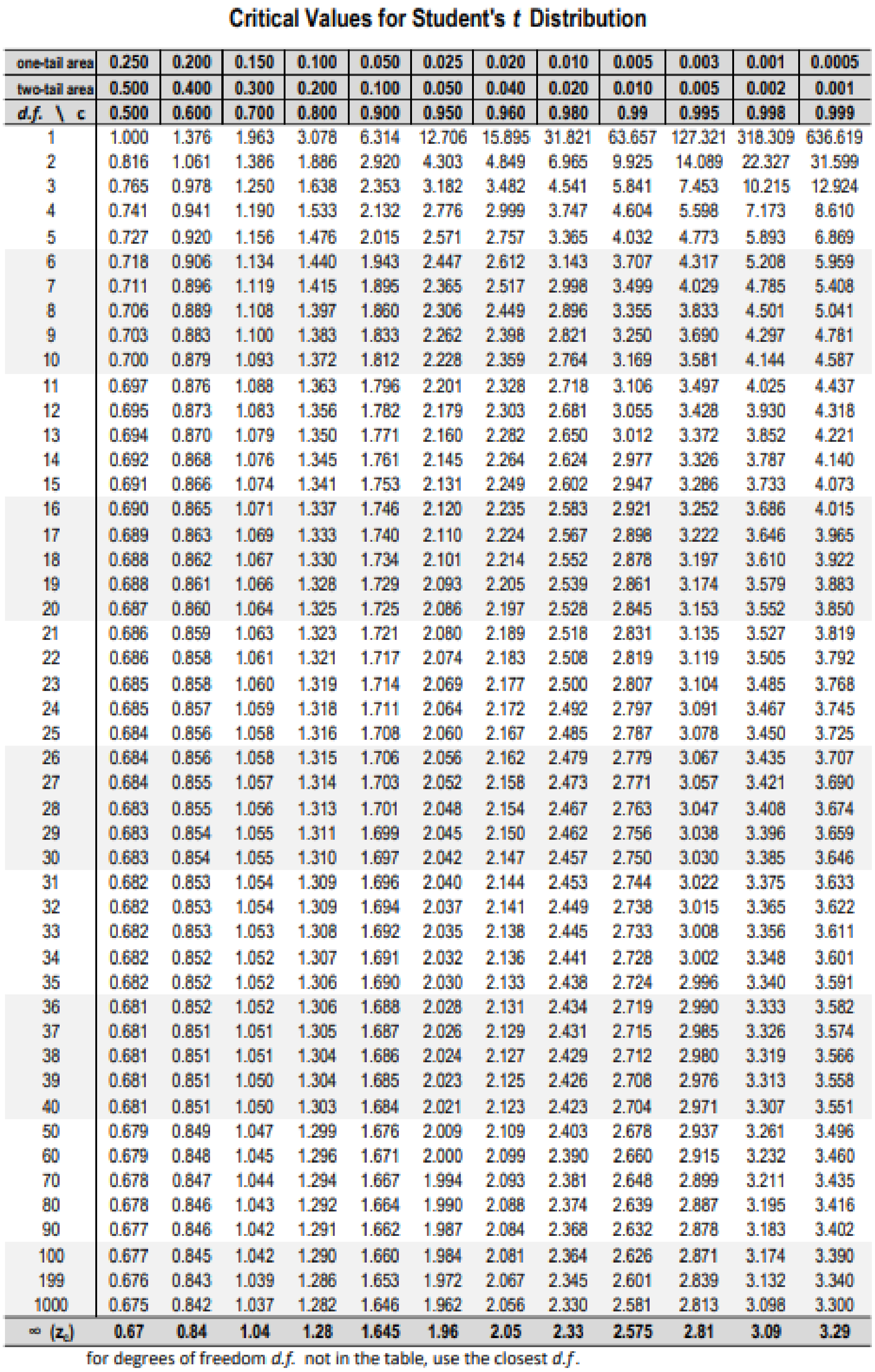

Critical Values for Student's *t* Distribution

one-tail area	**0.250**	**0.200**	**0.150**	**0.100**	**0.050**	**0.025**	**0.020**	**0.010**	**0.005**	**0.003**	**0.001**	**0.0005**
two-tail area	**0.500**	**0.400**	**0.300**	**0.200**	**0.100**	**0.050**	**0.040**	**0.020**	**0.010**	**0.005**	**0.002**	**0.001**
***d.f.* \ c**	**0.500**	**0.600**	**0.700**	**0.800**	**0.900**	**0.950**	**0.960**	**0.980**	**0.99**	**0.995**	**0.998**	**0.999**
1	1.000	1.376	1.963	3.078	6.314	12.706	15.895	31.821	63.657	127.321	318.309	636.619
2	0.816	1.061	1.386	1.886	2.920	4.303	4.849	6.965	9.925	14.089	22.327	31.599
3	0.765	0.978	1.250	1.638	2.353	3.182	3.482	4.541	5.841	7.453	10.215	12.924
4	0.741	0.941	1.190	1.533	2.132	2.776	2.999	3.747	4.604	5.598	7.173	8.610
5	0.727	0.920	1.156	1.476	2.015	2.571	2.757	3.365	4.032	4.773	5.893	6.869
6	0.718	0.906	1.134	1.440	1.943	2.447	2.612	3.143	3.707	4.317	5.208	5.959
7	0.711	0.896	1.119	1.415	1.895	2.365	2.517	2.998	3.499	4.029	4.785	5.408
8	0.706	0.889	1.108	1.397	1.860	2.306	2.449	2.896	3.355	3.833	4.501	5.041
9	0.703	0.883	1.100	1.383	1.833	2.262	2.398	2.821	3.250	3.690	4.297	4.781
10	0.700	0.879	1.093	1.372	1.812	2.228	2.359	2.764	3.169	3.581	4.144	4.587
11	0.697	0.876	1.088	1.363	1.796	2.201	2.328	2.718	3.106	3.497	4.025	4.437
12	0.695	0.873	1.083	1.356	1.782	2.179	2.303	2.681	3.055	3.428	3.930	4.318
13	0.694	0.870	1.079	1.350	1.771	2.160	2.282	2.650	3.012	3.372	3.852	4.221
14	0.692	0.868	1.076	1.345	1.761	2.145	2.264	2.624	2.977	3.326	3.787	4.140
15	0.691	0.866	1.074	1.341	1.753	2.131	2.249	2.602	2.947	3.286	3.733	4.073
16	0.690	0.865	1.071	1.337	1.746	2.120	2.235	2.583	2.921	3.252	3.686	4.015
17	0.689	0.863	1.069	1.333	1.740	2.110	2.224	2.567	2.898	3.222	3.646	3.965
18	0.688	0.862	1.067	1.330	1.734	2.101	2.214	2.552	2.878	3.197	3.610	3.922
19	0.688	0.861	1.066	1.328	1.729	2.093	2.205	2.539	2.861	3.174	3.579	3.883
20	0.687	0.860	1.064	1.325	1.725	2.086	2.197	2.528	2.845	3.153	3.552	3.850
21	0.686	0.859	1.063	1.323	1.721	2.080	2.189	2.518	2.831	3.135	3.527	3.819
22	0.686	0.858	1.061	1.321	1.717	2.074	2.183	2.508	2.819	3.119	3.505	3.792
23	0.685	0.858	1.060	1.319	1.714	2.069	2.177	2.500	2.807	3.104	3.485	3.768
24	0.685	0.857	1.059	1.318	1.711	2.064	2.172	2.492	2.797	3.091	3.467	3.745
25	0.684	0.856	1.058	1.316	1.708	2.060	2.167	2.485	2.787	3.078	3.450	3.725
26	0.684	0.856	1.058	1.315	1.706	2.056	2.162	2.479	2.779	3.067	3.435	3.707
27	0.684	0.855	1.057	1.314	1.703	2.052	2.158	2.473	2.771	3.057	3.421	3.690
28	0.683	0.855	1.056	1.313	1.701	2.048	2.154	2.467	2.763	3.047	3.408	3.674
29	0.683	0.854	1.055	1.311	1.699	2.045	2.150	2.462	2.756	3.038	3.396	3.659
30	0.683	0.854	1.055	1.310	1.697	2.042	2.147	2.457	2.750	3.030	3.385	3.646
31	0.682	0.853	1.054	1.309	1.696	2.040	2.144	2.453	2.744	3.022	3.375	3.633
32	0.682	0.853	1.054	1.309	1.694	2.037	2.141	2.449	2.738	3.015	3.365	3.622
33	0.682	0.853	1.053	1.308	1.692	2.035	2.138	2.445	2.733	3.008	3.356	3.611
34	0.682	0.852	1.052	1.307	1.691	2.032	2.136	2.441	2.728	3.002	3.348	3.601
35	0.682	0.852	1.052	1.306	1.690	2.030	2.133	2.438	2.724	2.996	3.340	3.591
36	0.681	0.852	1.052	1.306	1.688	2.028	2.131	2.434	2.719	2.990	3.333	3.582
37	0.681	0.851	1.051	1.305	1.687	2.026	2.129	2.431	2.715	2.985	3.326	3.574
38	0.681	0.851	1.051	1.304	1.686	2.024	2.127	2.429	2.712	2.980	3.319	3.566
39	0.681	0.851	1.050	1.304	1.685	2.023	2.125	2.426	2.708	2.976	3.313	3.558
40	0.681	0.851	1.050	1.303	1.684	2.021	2.123	2.423	2.704	2.971	3.307	3.551
50	0.679	0.849	1.047	1.299	1.676	2.009	2.109	2.403	2.678	2.937	3.261	3.496
60	0.679	0.848	1.045	1.296	1.671	2.000	2.099	2.390	2.660	2.915	3.232	3.460
70	0.678	0.847	1.044	1.294	1.667	1.994	2.093	2.381	2.648	2.899	3.211	3.435
80	0.678	0.846	1.043	1.292	1.664	1.990	2.088	2.374	2.639	2.887	3.195	3.416
90	0.677	0.846	1.042	1.291	1.662	1.987	2.084	2.368	2.632	2.878	3.183	3.402
100	0.677	0.845	1.042	1.290	1.660	1.984	2.081	2.364	2.626	2.871	3.174	3.390
199	0.676	0.843	1.039	1.286	1.653	1.972	2.067	2.345	2.601	2.839	3.132	3.340
1000	0.675	0.842	1.037	1.282	1.646	1.962	2.056	2.330	2.581	2.813	3.098	3.300
∞ (z_c)	**0.67**	**0.84**	**1.04**	**1.28**	**1.645**	**1.96**	**2.05**	**2.33**	**2.575**	**2.81**	**3.09**	**3.29**

for degrees of freedom *d.f.* not in the table, use the closest *d.f*.

Figure I. 1: t-table

Appendix J: Detailed Test Results

Angle of Repose results:

Table J.1: Angle of Repose Results

Model	400,000-faces	400-faces	100-faces	40-faces
1	53.02	47.37	43.70	44.43
2	50.46	50.85	48.61	45.26
3	44.86	57.56	40.74	43.70
4	47.51	49.73	51.80	39.36
5	53.41	49.45	54.45	42.63
6	51.33	51.73	43.52	45.04
7	41.55	50.30	42.24	45.25
8	48.35	50.08	44.49	46.73
9	43.51	43.40	43.66	41.32
10	50.89	44.51	45.15	46.83
11	54.17	53.12	44.23	41.06
12	51.81	47.82	38.49	44.49
13	48.09	41.58	51.62	48.49
14	49.90	38.43	48.31	45.67
15	44.99	39.26	48.23	46.44
Mean AoR [°]	**48.92**	**47.68**	**45.95**	**44.45**
95% CL uncertainty [°]	**2.12**	**2.94**	**2.45**	**1.37**

The uncertainty is calculated as follows:

$$u_{AoR} = \frac{t_{0.95} * s_{AoR}}{\sqrt{N}} \qquad (J.1)$$

, where:

- u_{AoR} is the uncertainty on the mean angle of repose with a CL of 95%
- N is the sample size
- $t_{0.95}$ is the t-value (in this case for $N = 15$, $t_{0.95} = 2.145$)

- s_{AoR} is the standard deviation of the angle of repose

The overlap between two 95% confidence level intervals is calculated as follows:

$$overlap(\%) = \frac{\max\left(0, \min(U_1, U_2) - \max\left(L_1, L_2\right)\right)}{CL_{width}} * 100 \qquad (J.2)$$

, where:

- $overlap(\%)$: the overlap in percentage between two 95% confidence intervals
- U_1, L_1 : upper (U) and lower (L) bounds of the reference confidence intervals
- U_2, L_2: upper (U) and lower (L) bounds of the comparison confidence intervals
- CL_{width} is the width of the reference confidence level interval

Table J.2: Percentage overlap of 95% CL intervals between simplification levels (Angle of Repose)

Comparison	Reference interval	CL overlap (%)
400 w.r.t 400,000 faces	$CL_{400,000-faces}$	90.2
100 w.r.t 400 faces	$CL_{400-faces}$	62.3
40 w.r.t 100 faces	$CL_{100-faces}$	47.2
100 w.r.t 400,000 faces	$CL_{400,000-faces}$	37.7
40 w.r.t 400,000 faces	$CL_{400,000-faces}$	0

IQR Estimation:

As only three data points (sensitivity values at 400, 100 and 40-face model) are available per descriptor, the IQR is estimated by linear interpolation. Specifically, the 25th percentile (Q_1) is calculated as a point one-quarter of the way between the minimum ($x_{\min}$) and the median (x_{median}):

$$Q_1 = x_{\min} + \frac{1}{4}\left(x_{\text{median}} - x_{\min}\right) \qquad (J.3)$$

and the 75th percentile (Q_3) is one-quarter of the way between the median (x_{median}) and the maximum ($x_{\max}$):

$$Q_3 = x_{\text{median}} + \frac{1}{4}(x_{\max} - x_{\text{median}}) \qquad (J.4)$$

The resulting IQR is then:

$$\text{IQR} = Q_3 - Q_1 = \frac{3}{4}(x_{\max} - x_{\min}) \qquad (J.5)$$

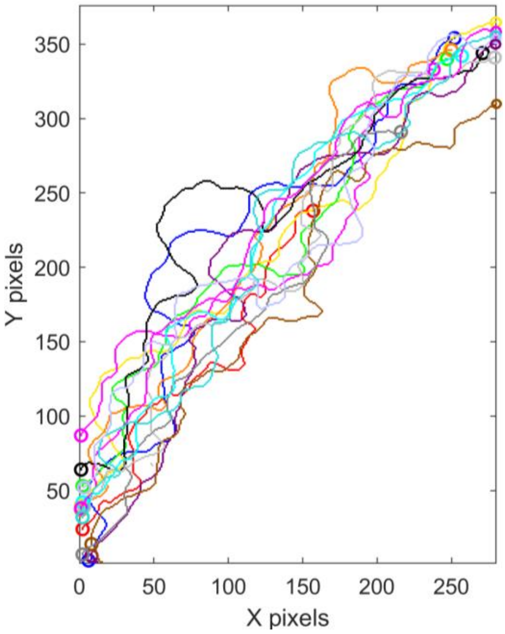

Figure J.1: Combined Edge Overlay (400,000 face model)

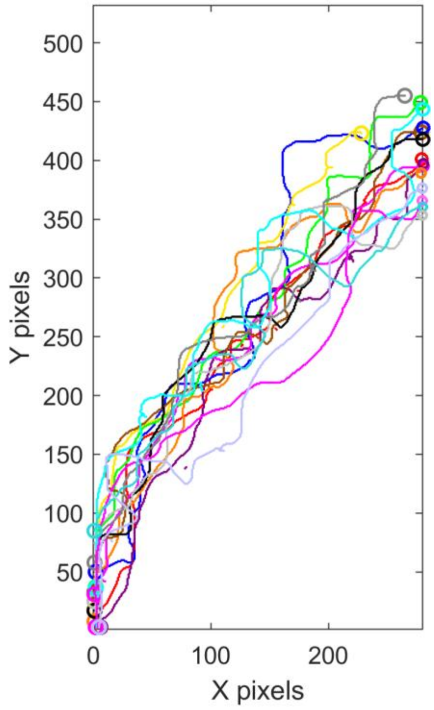

Figure J.2: Combined Edge Overlay (400 face model)

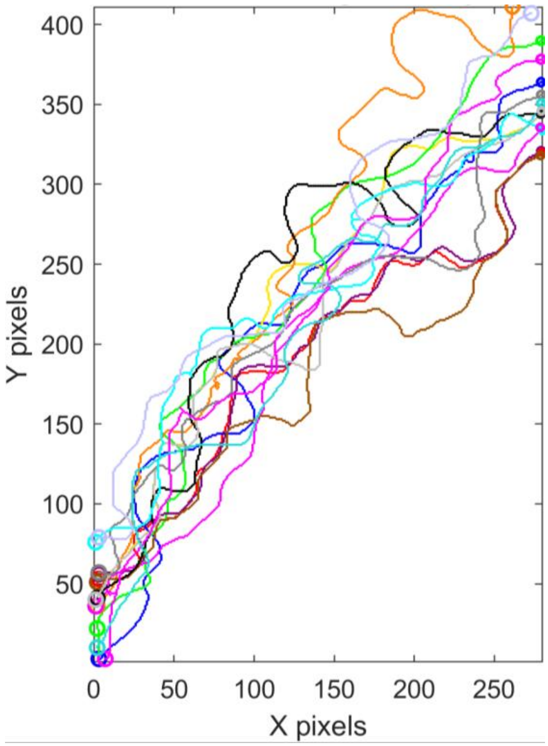

Figure J.3: Combined Edge Overlay (100 face model)

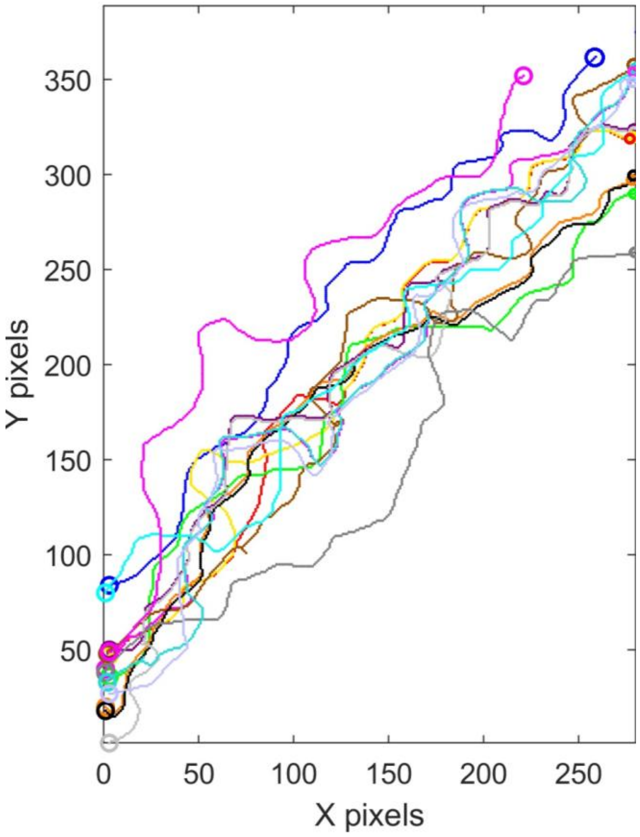

Figure J.4: Combined Edge Overlay (40 face model)

Coefficient of static friction results:

Table J.3: Wall friction angle results (random placement, single particle)

	400,000-face model	**400-face model**	**100-face model**	**40-face model**
	21.9	19	28.9	24.9
	16.3	26.2	22.7	28.4
	28.5	26.4	28.8	25.2
	28.3	20.2	24.2	22.8
	26.7	25.2	22.7	26.1
	18.2	25.2	24.4	23.6
	18.2	28.6	20.4	24.3
	28.2	25	22.9	23.4
	30.6	27.8	24.2	23.4
	31.3	31.8	25	20
	28.4	24.6	24.2	25
	25.6	20.3	23.9	29.9
	25.6	29.1	22.8	23.7
	27	26.6	28.3	25.3
	29.1	21.3	28.2	24.6
Mean wall friction angle [°] (single particle, random placement)	**25.6**	**25.2**	**24.8**	**24.7**
standard deviation [°]	**4.7**	**3.6**	**2.6**	**2.3**

Table J.4: Mean, Uncertainty and Relative Uncertainty values of coefficient of static friction (random placement, single particle)

Mean coefficient of static friction	**0.48**	**0.47**	**0.46**	**0.46**
CL 95%	0.06	0.04	0.03	0.03
Relative uncertainty [%]	11.81	9.22	6.74	6.05

Table J.5: Percentage overlap of 95% CL intervals between simplification levels (coefficient of static friction, random placement, single particle)

Comparison	Reference interval	CL overlap (%)
400 w.r.t 400,000 faces	$CL_{400,000-faces}$	66.67
100 w.r.t 400 faces	$CL_{400-faces}$	75.00
40 w.r.t 100 faces	$CL_{100-faces}$	100.00
100 w.r.t 400,000 faces	$CL_{400,000-faces}$	50.00
40 w.r.t 400,000 faces	$CL_{400,000-faces}$	50.00

Table J.6: Wall friction angle results (controlled placement, single particle)

	400,000-face model	400-face model	100-face model	40-face model
	25.2	26.3	24.8	24
	24.1	26.2	24.9	26.5
	25.3	25.1	28.8	23.8
	25	26	27	27.1
	24.6	26.3	24.5	25.9
	26.7	22.3	27	24.5
	27	26	25	26.8
	26	27	27	23.5
	33	30.8	26.2	25.2
	26.1	25.6	28	24.7
	33.2	33.8	24.2	22.9
	26.3	22.3	27.1	27.3
	34.2	29.1	24.3	23.6
	27	27	23.6	26
	27.1	33.2	24.7	24.7
Mean wall friction angle [°] (single particle, controlled placement)	**27.4**	**27.1**	**25.8**	**25.1**
standard deviation [°]	3.3	3.3	1.6	1.4

Table J.7: Mean, Uncertainty and Relative Uncertainty values of coefficient of static friction (controlled placement, single particle)

Mean coefficient of static friction	**0.52**	**0.51**	**0.48**	**0.47**
CL 95%	0.04	0.04	0.02	0.02
Relative uncertainty [%]	7.59	7.84	4.17	4.26

Table J.8: Percentage overlap of 95% CL intervals between simplification levels (coefficient of static friction, controlled placement, single particle)

Comparison	Reference interval	CL overlap (%)
400 w.r.t 400,000 faces	$CL_{400,000-faces}$	87.50
100 w.r.t 400 faces	$CL_{400-faces}$	37.50
40 w.r.t 100 faces	$CL_{100-faces}$	75.00
100 w.r.t 400,000 faces	$CL_{400,000-faces}$	25.00
40 w.r.t 400,000 faces	$CL_{400,000-faces}$	12.50

Table J.9: Wall friction angle results (bulk level)

	400,000-face model	400-face model	100-face model	40-face model
	28.2	28.8	28	27.6
	24.6	27.5	27.7	24.3
	30.2	26.6	28.5	24.3
	27.2	28.1	27	24.7
	26.2	25.3	25.4	29
	30.5	33	26.5	24.2
	28.6	30	25.1	26.5
	30.7	31	26.3	28
	30.7	26	30	28.9
	26.9	26.5	30.5	24.6
	26.2	28.8	31	24.3
	30.2	25	27	27.8
	34	26.8	28	28
	25	30.1	22	24.3
	30.3	31	27	23
Mean wall friction angle [°] (bulk level)	**28.6**	**28.3**	**27.3**	**26.0**
standard deviation [°]	**2.6**	**2.4**	**2.3**	**2.1**

Table J.10: Mean, Uncertainty and Relative Uncertainty values of coefficient of static friction (bulk level)

Mean coefficient of static friction	**0.55**	**0.54**	**0.52**	**0.49**
CL 95%	0.03	0.03	0.03	0.03
Relative uncertainty [%]	5.45	5.56	5.77	6.12

Table J.11: Percentage overlap of 95% CL intervals between simplification levels (coefficient of static friction, bulk level)

Comparison	Reference interval	CL overlap (%)
400 w.r.t 400,000 faces	$CL_{400,000-faces}$	83.33
100 w.r.t 400 faces	$CL_{400-faces}$	66.67
40 w.r.t 100 faces	$CL_{100-faces}$	50.00
100 w.r.t 400,000 faces	$CL_{400,000-faces}$	50.00
40 w.r.t 400,000 faces	$CL_{400,000-faces}$	0.00

Uncertainty of Coefficient of Static Friction:

The formula for calculating the uncertainty on the mean coefficient of static friction is.

$$u_{\mu_s} = \left|\frac{d\mu_{st}}{d\theta_w}\right| * u_{\theta_w} = \sec^2(\theta_w) * \frac{\pi}{180} * u_{\theta_w} \qquad (J.6)$$

u_{θ_w} is expressed as:

$$u_{\theta_w} = \sqrt{u_{random}^2 + u_{resolution}^2 + u_{accuracy}^2} \qquad (J.7)$$

$$u_{random} = \frac{t_{0.95} * s_{\theta_w}}{\sqrt{N}} \qquad (J.8)$$

$$u_{resolution} = \frac{1}{2} * resolution \qquad (J.9)$$

, where:

- u_{μ_s} is the uncertainty on the mean coefficient of static friction
- θ_w is the mean wall friction angle
- u_{θ_w} is the uncertainty of the wall friction angle
- u_{random} is the random error on the mean wall friction angle
- $u_{resolution}$ is the error due to resolution (here resolution = 0.1°)

- $u_{accuracy}$ is the accuracy of the inclined surface tester ($u_{accuracy}$ = 0.3°)
- N is the sample size (in this case N = 15)
- $t_{0.95}$ is the t-value for 95% CL (for N = 15 it is $t_{0.95} = 2.145$)
- s_{θ_w} is the standard deviation of the wall friction angle

Hausner Ratio test results:

Table J.12: Empty cylinder weight

Mean cylinder weight [g]	**181.9**
	181.7
	182
	181.9
	181.9
	181.9

Table J.13: Filled Cylinder weight

Weight (particles + cylinder) in [g]	**400,000 face-model**	**400 face-model**	**100 face-model**	**40 face model**
	516.5	539.9	569.3	592.9
	507.9	529.9	567.2	589.8
	519.8	539.9	563.0	586.0
	510.2	529.9	558.8	582.2
	516.4	534.5	556.7	579.1

Table J.14: Tapped Volume [L]

Tapped volume in [L]	**400,000 face-model**	**400 face-model**	**100 face-model**	**40 face model**
	0.69	0.71	0.74	0.75
	0.68	0.71	0.74	0.76
	0.7	0.69	0.74	0.76
	0.68	0.71	0.74	0.75
	0.69	0.7	0.73	0.76

Table J.15: Bulk density [g/L]

Bulk density [g/L]	**400,000 face-model**	**400 face-model**	**100 face-model**	**40 face model**
	334.6	358.0	387.4	411.0
	326.0	348.0	385.3	407.9
	337.9	358.0	381.1	404.1
	328.3	348.0	376.9	400.3
	334.5	352.6	374.8	397.2
Mean bulk density [g/L]	**332.3**	**352.9**	**381.1**	**404.1**

Table J.16: Tapped density [g/L]

Tapped density in [g/L]	**400,000 face-model**	**400 face-model**	**100 face-model**	**40 face model**
	484.9	504.2	523.5	548.0
	479.4	490.1	520.7	536.8
	482.7	518.8	515.0	531.7
	482.8	490.1	509.3	533.7
	484.8	503.8	513.4	522.6
Mean tapped density [g/L]	**482.9**	**501.4**	**516.4**	**534.6**

Table J.17: Mean, Uncertainty and Relative uncertainty of HR

	400,000 face-model	**400 face-model**	**100 face-model**	**40 face-model**
Mean HR [-]	1.45	1.42	1.36	1.32
CL 95% [-]	0.03	0.03	0.03	0.03
Relative uncertainty [%]	2.07	2.11	2.21	2.27

Table J.18: Percentage overlap of 95% CL intervals between simplification levels (HR)

Comparison	Reference interval	CL overlap (%)
400 w.r.t 400,000 faces	$CL_{400,000-faces}$	50.00
100 w.r.t 400 faces	$CL_{400-faces}$	0.00
40 w.r.t 100 faces	$CL_{100-faces}$	33.33
100 w.r.t 400,000 faces	$CL_{400,000-faces}$	0.00
40 w.r.t 400,000 faces	$CL_{400,000-faces}$	0.00

Uncertainty of HR:

$$u_{HR} = HR_{mean} * \sqrt{\left(\frac{u_{\rho_b}}{\rho_{b_{mean}}}\right)^2 + \left(\frac{u_{\rho_t}}{\rho_{t_{mean}}}\right)^2} \qquad (J.10)$$

In order to calculate this first u_{ρ_b} and u_{ρ_t} have to be known:

$$u_{\rho_b} = \sqrt{u_m^2 + u_{v_b}^2} \qquad (J.11)$$

$$u_{\rho t} = \sqrt{u_m^2 + u_{v_t}^2} \qquad (J.12)$$

$$u_m = \sqrt{\left(\frac{1}{2} * res_{scale}\right)^2 + \left(\frac{t_{0.95} * s_m}{\sqrt{N}}\right)} \qquad (J.13)$$

$$u_{v_b} = \frac{1}{2} * res_{cylinder} \qquad (J.14)$$

$$u_{v_t} = \sqrt{\left(\frac{1}{2} * res_{cylinder}\right)^2 + \left(\frac{t_{0.95} * s_v}{\sqrt{N}}\right)} \qquad (J.15)$$

, where

- u_{HR} is the uncertainty of the mean HR
- u_{ρ_b} is the uncertainty of the mean bulk density
- u_{ρ_t} is the uncertainty of the mean tapped density
- HR_{mean} is the mean value of HR
- $\rho_{b_{mean}}$ is the mean value of bulk density
- $\rho_{t_{mean}}$ is the mean value of the tapped density
- u_m is the uncertainty of the mass
- u_{v_b} is the uncertainty of the bulk volume
- u_{v_t} is the uncertainty of the tapped volume
- N is the sample size (in this case N = 5)
- $t_{0.95}$ is the t-value for 95% CL (for N = 5 it is $t_{0.95} = 2.770$)
- s_m is the standard deviation of the mass
- res_{scale} is the resolution for measurement of the weight is 0.1 gram
- $res_{cylinder}$ is the resolution for measurement of the volume is 0.02 litres